Unraveling the grain size evolution in the Earth's upper mantle : experimental observations and theoretical modeling

Leïla Hashim

Centre Val de Loire UNIVERSITÉ
Spirit of the Loire Valley

UNIVERSITÉ D'ORLÉANS

UNIVERSITE D'ORLEANS

ÉCOLE DOCTORALE ÉNERGIE, MATÉRIAUX, SCIENCES DE LA TERRE ET DE L'UNIVERS

Institut des Sciences de la Terre d'Orléans

THÈSE présentée par :

Leïla HASHIM

soutenue le : **17 Mai 2016**

pour obtenir le grade de : **Docteur de l'Université d'Orléans**

Discipline/ Spécialité : **Sciences de la Terre et de l'Atmosphère**

Unraveling the grain size evolution in the Earth's upper mantle

Experimental observations and theoretical modeling

THÈSE dirigée par :

Fabrice GAILLARD	Co-directeur de thèse, ISTO, Orléans
Bruno SCAILLET	Co-directeur de thèse, ISTO, Orléans

RAPPORTEURS :

Patrick CORDIER	Professeur, Université Lille 1, Lille
Ben HOLTZMAN	Associate research professor, Lamont-Doherty Earth Observatory, USA

JURY :

Jacques POIRIER	Professeur, CEMHTI, Orléans, Président du jury
Patrick CORDIER	Professeur, Université Lille 1, Lille
Ben HOLTZMAN	Associate research professor, Lamont-Doherty Earth Observatory, USA
Holger STÜNITZ	Professor, Universitetet i Tromsø, Norvège
Sylvie DEMOUCHY	Chargée de recherche, Géosciences Montpellier, Montpellier
Emmanuel GARDÉS	Chargé de recherche, CIMAP, Caen
Fabrice GAILLARD	Chargé de recherche, ISTO, Orléans

In critical moments, men sometimes see exactly what they wish to see.

Mr. Spock – "*The Tholian Web*", 1968

The most exciting phrase to hear in science, the one that heralds new discoveries, is not 'Eureka!' but 'That's funny...'

Isaac Asimov (1920–1992)

Die Definition von Wahnsinn ist immer wieder das Gleiche zu tun und andere Ergebnisse zu erwarten.

Albert Einstein (1879–1955)

Remerciements

Les remerciements... Une coutume pour chaque thésard de les rédiger... Une coutume pour moi de les lire systématiquement. J'ai toujours voulu savoir si au moins, les autres thésard(e)s vivaient la même chose que moi... La thèse a été pour moi un long chemin initiatique, qui m'a permis de me connaître plus, de repousser ce que je pensais être mes limites intellectuelles, de me trouver moi...

Avant toute chose, je voudrais remercier les membres du jury. Un panel de grands chercheurs qui ont lu le manuscrit, autorisé la soutenance et ont également fait le déplacement pour assister à mes 37 min de présentation orale. Merci donc aux rapporteurs d'avoir eu la gentillesse (et curiosité ?) de lire en détails mon manuscrit : Patrick Cordier et Ben Holtzman. Merci aux examinateurs, qui ont également lu le manuscrit dans son entièreté (en même temps, 78 pages, biblio incluse, c'est pas si long...) : Jacques Poirier, Holger Stünitz, Sylvie Demouchy et Emmanuel Gardés (bon, examinateur/co-encadrant, ce sont juste des termes ; devrait-on être si à cheval sur la définition des mots... ? ☺). Merci à vous pour cette belle discussion pendant la séance questions, de m'avoir laissée répondre ce qui me semblait être juste, et de m'avoir appris des choses qui étaient, pour moi, encore floues.

Ensuite, je voudrais remercier la personne qui m'a soutenue, poussée jusqu'à mes limites, qui a cru en moi pendant ces quatre années et demies de thèse : Fabrice Gaillard. Pouah... C'était un long chemin : du master 2, où j'étais la petite étudiante naïve, qui pensais que tout ce qui était dit en cours était vérité absolue, au stade de docteur, celle qui espère voir un jour la loi de croissance Hashim *et al.* écrite sur les tableaux des cours magistraux des sciences de la Terre (oui, bon, faut pas non plus pousser, nous savons tous que la loi dite Hashim n'est pas encore concrètement applicable dans le contexte mantellique, car si on en croit la composition interne de la Terre, il n'y a pas que de l'olivine...). Un papa de la recherche... On en parle souvent des papas (ou mamans !) de la recherche... Et bien, un grand merci Fabrice : tu as su faire de moi une expérimentaliste (oui, bon, il arrive que je casse des choses), tu as su me laisser libre choix de mon sujet lorsque les expériences ne marchaient pas dans le sens que je souhaitais (oui, les manips sont encore là ; si j'avais eu le temps, et surtout le courage, la partie Annexe E aurait existé et ce serait intitulée "Les expériences qui ont foiré, celles qui ne faut donc pas retenter... À lire avec beaucoup d'attention !"), tu as su attendre que je lise ma biblio sur la rhéologie mantellique du point de vue expérimentale (en gros, l'équipe de Kohlstedt, de Karato, les Lillois, les Montpelliérains, les Toulousains...), que j'essaye d'en tirer une loi rhéologique à la Hirth and Kohlstedt (2003), sans vraiment que je sache où ça me mène et que je vienne avec mon sujet de thèse, celui qui me portait à coeur : "Fabrice, redéfinissons la loi de croissance de l'olivine !". Merci de m'avoir rappelé à ma soutenance que c'était moi qui avais voulu travailler sur la croissance de grains, que je t'ai convaincu que c'était un bon sujet et qu'il méritait profondes investigations, tant du point de vue expérimental (Chapter 2) que théorique (Chapter 1). Tu as su former mon cerveau à la Science, refaire jaillir ma curiosité, écouter mes idées (et rejeter celles qui n'étaient pas bonnes !), me pousser au cul lorsque mon perfectionnisme faisait front, de me laisser prendre du temps lorsque j'étais en plein burnout (et ça, deux fois si mes souvenirs sont bons !)... Bref, un ÉNORME merci ☺.

L'encadrement de cette thèse n'aurait également pas pu être possible sans Bruno Scaillet. Merci d'avoir accepté d'être le directeur de thèse officiel, il y a de ça maintenant 5 ans.

Merci également à Emmanuel Gardés (Manu G de son petit nom) pour ton encadrement, sans qui les séances sol-gel auraient très vite été abandonnées, de m'avoir appris à polir (car oui, ma réputation au labo est bien connue, mais tu es celui qui m'a appris à correctement polir au départ), d'avoir été suffisamment patient pour avoir avec moi des discussions théoriques sur la croissance de grains, sur les joints de grains, la diffusion dans les grains... Et puis, ça c'est sans compter les soirées complètement à côté de la plaque, à ne plus savoir regarder droit devant, et à ne plus réussir à articuler... Cette thèse n'aurait pas été la même sans toi.

Avant de remercier les personnes du laboratoire, je voudrais remercier les différentes interactions avec d'autres chercheurs provenant d'autres laboratoires.

Il y a d'abord Luiz F. G. Morales : I am immensely grateful ; You have let me use the 8-year old SEM-FEG machine at GFZ, you have trusted me not to break the EBSD camera each time I was inserting it into the vacuumed chamber (you told me it was impossible though...), you have been a real moral support for the whole month I have spent in Potsdam. The paper is coming out, and although you tell me I did all the work each time I submit a conference abstract, your name is on it because, among other things, you have also listened to my grain growth questions, those that I could not answer at the time. Thank you Luiz.

Il y a ensuite Katharina Marquardt du BGI à Bayreuth. Thank you for the three days at BGI, for the discussions and for looking into the grain boundaries of my sample with your TEM.

Merci également à François Brisset de l'Université d'Orsay d'avoir eu du temps pour passer mes échantillons (qui étaient plus nombreux qu'initialement prévu) à l'EBSD, et tout ça, dans l'urgence pour finaliser la partie analytique/détermination de la taille de grains de ma thèse.

D'autres personnes sont également à remercier : David Kohlstedt, Lars Hansen, Saswata Hier-Majumder, Yasuko Takei, Uli Faul, Boris Mantisi, Bertrand Guillot, Anne Pommier, Renée Heilbronner, Sandra Ory, François Faure, Valerio Cerantola... La liste est encore longue, et je dois certainement oublier des personnes dans la liste précédente (j'ai checké mes archives de mail pour être sûre d'avoir oublié personne... Mais la certitude n'a jamais été mon point fort durant la thèse...), mais celles citées ont été d'une aide incroyable, que ce soit juste pour m'aider dans la théorie, ou encore m'aider pour des aspects pratiques (comme des envois d'échantillons...). Notamment, je voudrais en particulier remercier Anne Pommier, qui m'a fourni l'olivine de San Carlos lorsque la décision a été prise de réaliser les manips de croissance sur de l'olivine naturelle.

Revenons maintenant au personnel du laboratoire. Et je vais commencer par Rémi Champallier, le grand chef expérimental, celui qui a sacrifié certains week-ends (sans que je ne lui demande réellement au préalable ce qu'il avait prévu de faire) afin que je puisse tourner mes manips Paterson (celles qui sont archivées dans le cahier de manip Paterson, dans l'ordinateur Paterson, et dans mon ordinateur) à des vitesses expérimentalement lentes, juste parce que je me disais "Allez, on va faire très lent... !". Je souhaite te remercier du fond du coeur, et sache qu'il y a une chose bien robuste, que j'ai appris et que je n'ai cessé de répéter à Fabrice lorsqu'on a commencé les manips PC : "Il faut changer un paramètre expérimental à la fois !". Oui, sinon, ça devient brouillon... Je n'ai qu'une seule autre chose à dire : "Ah... Ah... Ah !!!!" (entends-tu donc la mouette rire ? ! !).

Un grand merci aux gars de l'atelier, à savoir Esteban (oui, j'ai pas été une des plus sympa en M2... À te demander de me faire une électrode interne dans mon pauvre caillou que je n'ai pas une seule fois réussi à carotter de façon complètement cylindrique...), Philippe Teulat (même si tu m'as engueulé une fois, et que je ne savais plus où me mettre, et que bon, ce n'était pas réellement de ma faute...), à Fred (tu es arrivé au labo quand je n'avais plus besoin d'aller à l'atelier, sauf... pour du scotch double face ou des boules quies), à p'tit Rémy. Eh, les gars, elles étaient pas top les photos qu'on vous a mises sur votre calendrier alors ! ! !

Je voudrais également remercier Ida. Cara Ida... Je crois que tu es ma sauveuse. Même si au début, je ne savais pas exactement ce que je devais faire avec mes échantillons (à part savoir si mes échantillons étaient à l'équilibre chimique, savoir si mes échantillons sol-gel avaient fonctionné, savoir si les échantillons SPS étaient bien exempt de porosité, mesurer une taille de grains moyenne...), tu as toujours été là pour me conseiller, m'aider dans mes galères, faire des

images très haute résolution. Tu as écouté mes malheurs pendant les séances MEB, écouter ma colère contre la recherche, rigolé avec moi de joie lorsque mes échantillons présentaient enfin les caractéristiques que je cherchais (ou voulais, ça depend toujours du point de vue...), parlé de plantes médicinales, des mecs que je convoitais... Tu as su être une bonne amie en plus d'être une super collègue. Cette thèse n'aurait jamais été possible si tu ne m'avais pas poussé à continuer dans ma démarche analytique, de m'aider à trouver des solutions autre que du MEB classique (polissage ionique, polissage EBSD, test de nouveaux paramètres sur le MEB, EBSD...).

Bien entendu, toute cette partie analytique n'aurait pas pu être possible sans Patricia ! Le nombre de fois où je suis venue te voir "Oui, salut Patricia ! Ça va ? ! Dis, euh, je suis en train de polir mes échantillons pour ma séance... euh... de demain matin... Tu pourras me les métalliser ?" et à chaque fois, c'était avec un grand sourire "Oui, y a pas de soucis !". Alors merci ! Merci aussi de m'avoir soutenue lorsqu'il y a eu conflit avec l'autre du BRGM, quand il s'agissait d'utiliser le PECS. Sans les couches de 2 nm d'épaisseur sur chacun de mes plots, il m'aurait été impossible de réaliser mes cartographies EBSD... Et tu as vu la quantité d'échantillons que j'avais, ainsi que le temps que ça me demandait de polir chaque plot... Merci d'avoir été patiente avec moi ☺.

Merci à Sylvain également : tu m'as bien aidé lorsqu'il a fallu que je change de type de résine. Celle que tu m'as conseillé a été d'un grand succès pour mes analyses. Une joie de polir ce genre de résine qui rentrait bien dans tous les interstices entre les grains.

Je voudrais maintenant remercier d'autres personnes du personnel technique, à savoir Didier (la première rencontre était quelque chose, tu t'en souviens probablement pas... J'étais dans la salle du gros bleu/gros vert, en train de régler la température de ma manip, "apeurée" d'être pour la première fois toute seule devant cette grosse cocotte minute, et tu as commencé à toucher les circuits électriques en marmonnant dans ta barbe. Je m'étais demandée qui tu étais et ce que tu étais en train de faire sur ma manip... Et si tu allais foirer ma trempe... Mais non, fort heureusement, tu n'as pas bidouillé les fils ce jour-là !), les informaticiens (Yohann, Laurent Catherine, merci à tous les deux de m'avoir aidé avec mes ordis perso, que ce soit en voulant créer un Hackintosh, en pensant que j'avais blacklisté ma box chez moi avec mes téléchargements illégaux, qu'en me fournissant toutes les fournitures informatiques que je voulais pour faire avancer mon boulot de thèse... ; Tatiana et Kévin), Philippe X, Philippe Leroy (merci pour avoir dézingué le nid d'abeilles des escaliers, d'avoir installé les étagères qu'on se prenait régulièrement dans la tête avec Mickaël, d'avoir installé le grand bureau deux places qui n'est vraiment pas pratique du tout au final...), à Marlène et Martine (pour tout ce qui était inscription à l'université ou encore réservation de salle de dernière minute).

Un merci à Nathalie Pothier, sans qui cette thèse n'aurait pas pu avoir le même bagage littéraire. Tu as toujours tiré toutes les ficelles que tu pouvais pour que je puisse avoir les papiers ou livres que je recherchais. Et c'est en lisant, une quantité incroyable, que j'ai réussi à mettre les choses les unes à côté des autres pour réussir à arriver aux conclusions de cette thèse. Je t'en suis très reconnaissante. Merci à Marielle Hatton également, avec qui nous avons passé à trois (dont Nath) de bons moments de discussion ! Merci d'avoir joué le jeu, càd feint ne rien savoir lorsque les gars de l'atelier pensaient que tu étais responsable de leur calendrier. On s'est vraiment bien fendues la gueule avec Alex ;-)

Merci aux gestionnaires : Marie-No (merci pour tout, et surtout de ta gentillesse), Olivier (merci, merci, merci de ne jamais m'en avoir voulu de demander un ordre de mission trois jours avant le départ) et Virginie (ma belle... que dire... de la Villa à maintenant, même si les choses ont changé, je sais qu'il y a toujours un petit quelque chose !). Merci également à Chantal, qui m'a beaucoup aidé au début de ma thèse pour l'inscription à mon premier AGU, mais surtout à l'EMPG à Kiel, conférence à laquelle je devais m'inscrire alors que j'étais justement à l'AGU. Avec le décalage horaire, ce n'était pas si évident, mais on a somme toute bien réussi. Quelle joie de revoir ensuite des années plus tard à un cours sur les plantes médicinales. Merci pour les photocopies des cours ! ! ! ! !

Merci à Jacques Précigout et Emmanuel Le Trong d'avoir travaillé avec moi étroitement pendant de longues heures. Que ce soit derrière le MEB pour les analyses EBSD où les idées

fusaient, tant bien sur la rhéologie que sur la croissance de grains, que derrière un autre écran d'ordinateur à essayer pendant presque deux ans à fitter trois fichus paramètres à la fois pour cette loi de croissance. Quel était le soulagement de réaliser que $n = 2$ lorsque les échantillons sont secs, archi-secs ! ! Tout était bien plus simple après ça (ou plus complexe, ça dépend du point de vue !).

Je voudrais remercier également le groupe des enseignants-chercheurs, à savoir Michel Pichavant (sans qui je n'aurais pas eu de recette de sol-gel ! Quelle joie de parcourir ton cahier de manip des années 80 !), Hugues Raimbourg et Romain Augier (pour ce stage de M1 qui m'a fait tant aimer la recherche. Je vous en suis réellement reconnaissante, même si ça n'avait pas dû être une partie de plaisir pour vous. . .), Guillaume Richard, Laurent Jolivet, Nicole Le Breton, Laurent Arbaret, Gaëlle Prouteau, Lionel Mercury (merci de m'avoir si généreusement prêté tes livres et m'avoir apporté une bonne biblio en plus !), Yannick Branquet, Charles Gumiaux, Jérémy Jacob, Ary Bruand, Pascale Gautret, Adrien Flavigny (même si officiellement, tu n'es pas enseignant-chercheur), Anaëlle Simmoneau (tu es celle qui m'a décidé à faire moi-même une thèse, et la première impression que j'ai eu de toi n'a jamais changé, tu es extra !). De près ou de loin, vous m'avez tous aidé à commencer et finir cette thèse.

L'équipe magma. . . Merci, tellement. Pour l'ambiance, le dynamisme, l'écoute, vos sourires : Giada (je ne saurais jamais te dire suffisamment merci, pour tout !), Caroline (si je n'avais pas eu mes problèmes de genoux, j'aurais certainement continué la zumba et je suis convaincue qu'on aurait continué de se fendre la gueule !), Juan (pour tes blagues à deux balles !), Marina (et Jérémy et leurs deux enfants !), Yann Morizet (oui, je t'inclus ici ! Tu voudrais que je t'inclus où ? ! !), Karine, Clairette (comment te remercier pour toutes ces discussions qu'on a eu au cours de ces cinq dernières années, mais surtout au cours de cette dernière année, qui m'a permis de m'évader de ma thèse). D'une manière un peu atypique, je souhaite remercier l'ascenseur du bâtiment ISTO. Oui, mes problèmes de genoux ont permis d'établir un lien particulier avec cette machine qui me permettait de monter à mon bureau. De la même manière, je souhaite remercier le canapé du hall d'entrée du bâtiment ISTO (un bon endroit pour faire la sieste lorsqu'on met des boules quies !).

Je remercie aussi mes co-thésards et post-doctorants, par ordre alphabétique (comme on nous l'apprend si bien pour faire la biblio) : Adoum, Alexandre, Alireza, Anne-Aziliz, Arnaud, Axelle, Bashar, Bastien (quelle joie de continuer de te voir alors que cela doit bien faire deux ans que tu as quitté le labo !), Benoît, Camille Clerc, Chloé, Claudie, Clément, Éloïse, Emanuela, FangFang (thank you so much for spending Christmas Eve 2015 with my family and myself !), Giulia, Joann, Julie, Kévin, Léo, Maximator (eh oui, je ne t'oublie pas ! Et bien entendu, ta belle femme Patricia !), Maxime, Mohammed, Myriam, Nicolas, Pier-Angelo (ou Pangelo, comme tu préfères !), Quentin, Rabi, Renata, Sarah, Saskia, Séb Jégo, Teddy, Thomas, Val, Vincent, Yann.

Une ligne pour trois femmes très spéciales : Nolwenn et Leslie avec qui nous nous sommes suivies du Master jusqu'à la fin de la thèse. Merci les filles pour les discussions et les bons moments de pause. Et Alexandra, une réelle amitié est née.

Mes co-bureaux : Mickaël (et donc Valérie et maintenant petit Clément !). . . Merci de m'avoir enduré depuis le Master 2. . . ? ! You've become my special Blumberbutt you know ☺. Yves. . . Partager des bières avec toi à partir de 15h sous le soleil tapant n'a pas été un problème. Pressée de te revoir aux US, my friend ! Et bien sûr, Zineb. . . Quel changement depuis ton arrivée à maintenant. Merci pour ta bonne humeur et tes sourires ! Contrairement à ce que j'ai bien pu dire il y a maintenant plus d'un an : ta joie me fait sourire !

Merci aux amis et aux copains un peu lointain (mais qui comptent tout de même !) : Nonette et Kalou (malgré les années sans nouvelles, je ne vous oublie absolument pas !), Mireille Schwaederle ainsi que Laurent, Éléonore et Angelina, Meissa et Max, Maud, Carole, Flob, Paul, Kiki, Charlène, Guillaume (ancien coloc d'Alexandra), Bastien (alias Tom-Tom), Aurore, ManuE, Mathieu, Nicolas Dubois Dunilac, Clémence Guerrier, Thibault (du GREMI), Séb (le chauve !), Morgane (la bretonne vivant à Toulouse, tout du moins, il y a encore 3 ans !), Jean-Yves (merci de m'avoir laissée habiter chez toi. C'est en habitant à Saint-Jean-le-Blanc que tout s'est débloqué !), Séti, Murielle.

D'autres amis, plus chers, sont également à remercier : Rayoult et Anaïs (et maintenant la belle Joanie ! ! ! !), Séb (et Camille, ainsi que toute la famille Danos bien entendu !), Laure. Vous me connaissez suffisamment pour savoir que ce n'est pas ici que je vais m'étaler.

Je remercie également les cercles de femmes, que ce soit ceux du Berry ou ceux d'Orléans. Une aide mensuelle, à ne pas louper !

Mes colocs de la Villa ! ! ! De bons moments passés ensemble, plaisant et éreintant ! ! Merci à Armel pour l'épluchage de graines de soja avec lesquelles nous n'avons jamais fait de tofu. Merci à Malky d'avoir supporté Billa. Je te l'accorde, ce n'était pas tâche facile. Merci à Colin pour m'avoir introduit au screaming orgasm (soyons clair, c'est un cocktail !). Merci Grand Dada pour l'épluchage d'oignons avec les masques de ski. Et bien plus encore...

Mes amis de très longue date : Nenya, Murion (et Vincent !), Betty, Laëtitia, Andréa (et aussi la maman d'Andréa qui sait bien lui remonter les culottes quand il faut ! Ça m'a vraiment touchée que tu viennes à ma soutenance !), Mica... Merci les Potiches. C'est dingue le chemin qu'on a toutes parcouru (oui, oui, les gars, je n'arrêterai pas de vous mettre au féminin !). Il y a dix ans, on nous l'aurait dit tout ça ? ! !

Je remercie Hugo et toute sa famille (Lisa, Simon, Claire, Martine, Patrick). Merci d'avoir croisé mon chemin.

Delphine, que dire... Le plus juste serait "gratitude".

Merci à ma famille. Dominique, Dad, Jules, Camille, Pépère et Mémère. Vous avez été d'un soutien immense, sans jamais complètement comprendre ce qui se passait en moi. Vous avez appris à mieux connaître mes mécanismes aussi je pense. Je crois que de la même manière, un mot juste est de rigueur et c'est bien "gratitude". Alors, Kamouschka, tu pourras raconter l'histoire de la croissance de grains ? ! ! De même, je remercie Billa, ma chatte (ou la Grosse comme l'appellerait si bien Armel !).

Enfin, je souhaite finir par ce qui commence, une belle aventure à tes côtés, Rémy. Tu réussis à m'enraciner, surtout lorsque je me perds moi-même... Cette thèse finie est le tremplin de tous nos projets, alors, on n'a plus qu'à foncer ! ! !

Cela en fait de longues pages de remerciements, mais comme je l'ai dit au début, cette thèse a été pour moi un long chemin initiatique et je ne me voyais pas abréger cette section juste par fainéantise. Non, cette thèse n'est pas seulement mon aboutissement, c'est l'aboutissement des différentes interactions que j'ai eu avec de nombreuses personnes depuis ces cinq dernières années, et je me devais, par respect pour toutes ces personnes, de les remercier. J'espère au moins n'avoir oublié personne...

Table des matières

Table des figures

Liste des tableaux

Introduction

Broadening our knowledge on the physical properties of Earth's interior is fundamental for a better understanding of our planet's global behavior. It is now clearly agreed that plate tectonics result from passive and active convection in the Earth's mantle (Bercovici, 2003, Davies and Richards, 1992), but modeling the generation of plate tectonics through the convective movements of the mantle is still delicate (Bercovici, 2003, Bercovici et al., 2000, Gueydan et al., 2014, Tackley, 2000). Numerous fields of geology implement these models, such as seismological observations, through tomographic imaging or seismic anisotropy (e.g. Rychert et al., 2012, Schmerr, 2012) or electrical conductivity (e.g. Baba et al., 2006, Naif et al., 2013, Sarafian et al., 2015, Selway, 2015). The geophysical observations of our planet's interior are usually interpreted thanks to surface field observations (Précigout and Gueydan, 2009, Skemer et al., 2013, Warren and Hirth, 2006) but also through experiments performed in the laboratory, which both reveal the appropriate underlying geological process (Hashim et al., 2013, Pommier et al., 2015, Sifré et al., 2014).

Grain size in polycrystalline rocks is a crucial parameter, which affects geophysical observations in the mantle (e.g. seismic wave attenuation, Behn et al., 2009), permeability of mantle rocks (e.g. for two-phase flow modeling, Richard et al., 2012) and also their rheology (Hirth and Kohlstedt, 2003). However, due to a minimization of the internal energy of the polycrystalline rock, the average grain size is constantly increasing with time (Atkinson, 1988, Burke and Turnbull, 1952), which is the kernel of this manuscript. In addition, there are several factors impacting grain growth, in particular deformation processes governed by intraganular defects (e.g. dislocations and disclinations, Cordier et al., 2014, Karato, 2008), which contributes to grain size reduction through dynamic recrystallization in the dislocation creep regime (Karato et al., 1980, Urai et al., 1986). At some point, decreasing the average grain size of the rock can therefore trigger a switch to grain size-dependent deformation regimes, such as diffusion creep or grain boundary sliding regimes, allowing grain growth to be the dominant process contributing to the evolution of grain size. Yet, this induces a complicated mechanical cycle, where grain growth and dynamic recrystallization are competing processes induced by the alternation of grain size-sensitive and grain size-insensitive deformation regimes (Austin and Evans, 2007, Hall and Parmentier, 2003, Pearce and Wheeler, 2011).

One other major argument on why grain size evolution singularly matters is the upscaling from human to geological length and time scales. Upscaling laboratory experiments to natural conditions therefore necessitates a decisive law for static grain growth by using the appropriate theoretical background.

Grain growth is the process by which the grain size of a strain-free (or nearly strain-free) material increases. Grain growth can be divided into two processes: (i) a continuous process, where the microstructure of the material coarsens uniformly, termed *normal grain growth* and (ii) a discontinuous process, *abnormal grain growth* (or secondary recrystallization), where a few large grains develop at the expense of smaller grains forming the matrix. In the case of normal grain growth, grain size and shape exhibit narrow distributions, which is time-independent as shown in Fig. 1(a). On the contrary, a bimodal grain size distribution develops in the case of abnormal grain growth since the large grains consume the matrix of smaller grains (Fig. 1(b)). Eventually, all the small grains from the matrix will be consumed therefore allowing normal grain

growth to proceed (Fig. 1(b)).

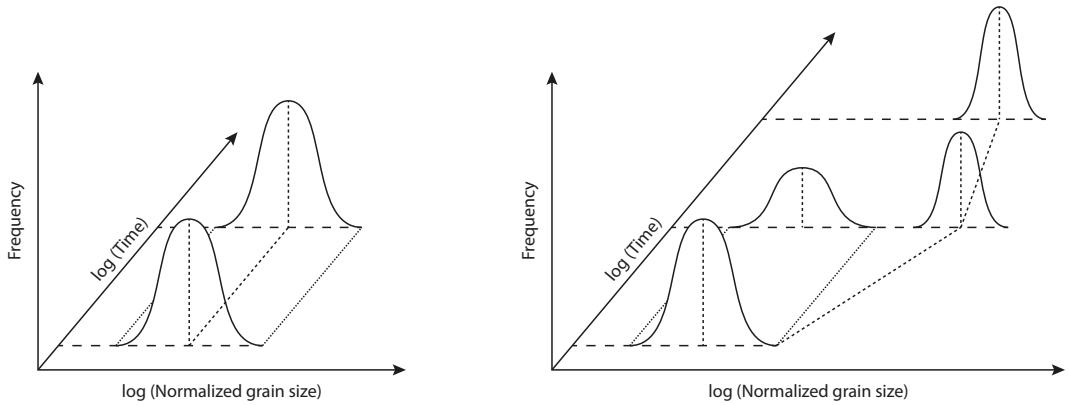

(a) Normal grain growth

(b) Abnormal grain growth

Figure 1 – Schematic evolution of the grain size distribution (after Detert (1978)).

In the laboratory, static grain growth requires measuring the experimental grain sizes of the polycrystalline aggregates in order to empirically determine the growth parameters, which is of the form (Atkinson, 1988, Burke and Turnbull, 1952):

$$r_f^n - r_i^n = t \cdot k_0 \exp\left(-\frac{E_a}{RT}\right) \tag{1}$$

with r_f and r_i, the final and initial grain radii (in m), n, the grain size exponent, t, the experimental duration (in s), k_0, a material-dependent pre-exponential factor (in $\mathrm{m^n\,s^{-1}}$), E_a, the empirical activation energy for grain growth (in $\mathrm{J\,mol^{-1}}$), R, the gas constant (in $\mathrm{J\,K^{-1}\,mol^{-1}}$) and T, the absolute temperature (in K). The grain size exponent, n, must first be established in order to determine the other growth parameters, usually fitted by a linear least squares fit of the data in a $\log_{10}(r_f^n - r_i^n)$ vs. $\log_{10}(t)$ plot. Ascertaining the grain size exponent is therefore critical, since it has considerable implications on grain size extrapolations to longer (geological) durations.

A number of experimental studies have empirically determined the parameters for olivine grain growth under static conditions, where different effects have been investigated, such as water (Karato, 1989, Ohuchi and Nakamura, 2007b), oxygen fugacity (f_{O_2}; Nichols and Mackwell, 1991), melt (Cabane et al., 2005, Faul and Scott, 2006) and secondary phases, e.g. pores (Karato, 1989, Nichols and Mackwell, 1991), orthopyroxenes (Hiraga et al., 2010, Tasaka and Hiraga, 2013) and clinopyroxenes (Ohuchi and Nakamura, 2007a,b). In these studies, two types of olivine aggregates have been used: (i) naturally-derived polycrystalline olivines (usually San Carlos olivine of composition $\sim \mathrm{Fo_{90}}$) and (ii) synthetic-derived olivines (either fabricated by the solution-gelation (sol-gel) method or by mixing of nano-oxides). These experiments were usually run at different temperatures (1200–1450 °C), pressures ranging from atmospheric pressure to 1.2 GPa and run durations as long as 763 h ($\sim$ 32 days). Linear least-square fits to the olivine grain growth law showed that the resulting grain size exponent values are very different from one study to another, but it generally seems to be constrained between 4 and 5.

The contrasting growth values in each of these studies indicate that there still does not exist one unambiguous grain growth law for olivine aggregates for application to rheological experiments but, most importantly, to natural geological conditions.

Therefore, the aim of this thesis is to increase the olivine grain growth database by performing high pressure and high temperature experiments and to confront and reconcile the existing grain growth database by using the appropriate theoretical background.

The previously published olivine grain growth experimental studies used in this manuscript are summarized in Fig. 2, where we have chosen a grain size exponent of $n = 4.37$, which corresponds to the average n deduced from these studies. This figure indicates the grain growth rates (i.e. $(G_f^n - G_i^n)/t$, with G, the grain diameter) as a function of absolute reciprocal temperature. We can observe two main effects: (i) genuinely dry experiments (open symbols) that were run under atmospheric pressure conditions (Hiraga et al., 2010, Karato, 1989, Nichols and Mackwell, 1991, Tasaka and Hiraga, 2013) and (ii) melt- and fluid-bearing experiments (orange and blue symbols), which were conducted at higher pressure and in the presence of a liquid phase (Cabane et al., 2005, Faul and Scott, 2006, Karato, 1989, Ohuchi and Nakamura, 2007a,b, Ohuchi et al., 2010). Indeed, as evidenced in this figure, liquid-bearing olivine aggregates display faster growth rates than genuinely dry olivine aggregates, suggesting two grain growth regimes, namely a slow, dry growth regime and a faster, liquid-bearing growth regime.

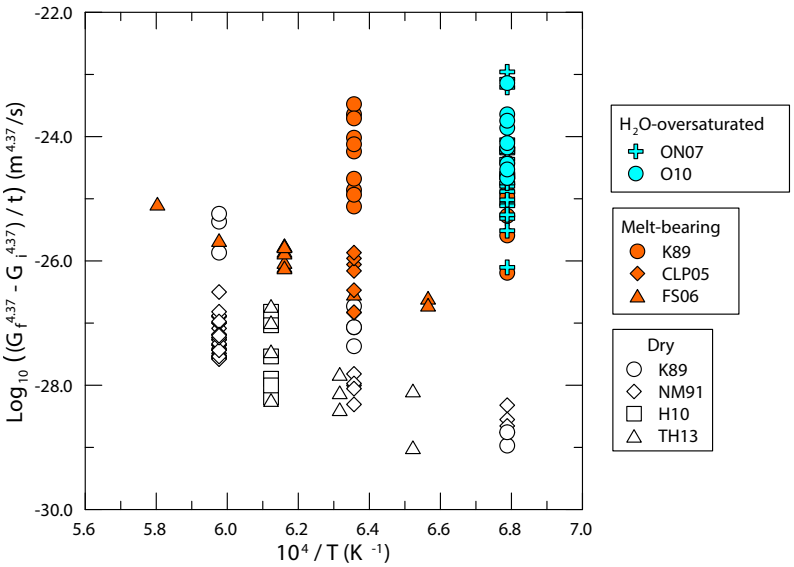

Figure 2 – Olivine grain growth rates vs. absolute reciprocal temperature for previously published experimental grain growth of olivine aggregates. Experiments are from Karato (1989) (K89), Nichols and Mackwell (1991) (NM91), Hiraga et al. (2010) (H10) and Tasaka and Hiraga (2013) (TH13), Cabane et al. (2005) (CLP05), Faul and Scott (2006) (FS06), Ohuchi and Nakamura (2007a,b) (ON07), Ohuchi et al. (2010) (O10).

Following this brief introduction, the manuscript is therefore divided in three chapters. The *first chapter* introduces the genuinely dry atmospheric database, as well as the physical theory behind dry grain growth. The discrepancies on the empirically determined growth values are in this chapter reconciled by using the diffusion properties of dry olivine aggregates. The *second chapter* presents the grain growth experiments performed in the course of this thesis on olivine aggregates, which was then confronted to published grain growth liquid-bearing aggregates. The reader will also find in this chapter a theoretical part, derived for liquid-bearing aggregates that will be used to obtain a grain growth law combining effects of both liquid-free and liquid-present grain growth processes.

Chapter three concerns another fundamental physical parameter within our planet, namely the viscosity. In this chapter, the reader will find an article published in *Earth and Planetary Science Letters*, which deals with the viscosity and the electrical conductivity of partially molten crustal rocks. It is an experimental study, which was conducted in a gas-medium deformation apparatus (Paterson press) on Himalayan metapelites in order to better understand the geophysical anomalies detected beneath the Himalayan-Tibetan orogenic system.

Four appendices can be found after the *bibliography section*, in which (A) I demonstrate that

the grain size exponent value n cannot unequivocally be defined from the empirical formalism of Eq. (1), (B) I describe the grain size determination methods, the cut-section effect, our error estimation from published experiments as well as the complete grain growth database, (C) I show complementary figures from chapter 2 and (D) I include a short research grant proposal accepted by the Deutscher Akademischer Austauschdienst (DAAD, Germany) for a six months project at Helmholtz-Zentrum Potsdam – Deutsches GeoForschungsZentrum (GFZ) in Potsdam (Germany). The project explains the need to perform nanotomography imaging of melt films in partially molten olivine aggregates to better understand the wetting properties of very low melt fractions. A feasibility test is introduced in this appendix, which will surely be investigated in more details in the future.

Introduction

Étudier les processus physiques se produisant à l'intérieur de la Terre est essentiel pour mieux comprendre le comportement général de notre globe. Il est maintenant admis que la tectonique des plaques résultent des convections passives et actives se déroulant dans le manteau terrestre (Bercovici, 2003, Davies and Richards, 1992). Cependant, ce genre de processus de grande échelle est encore aujourd'hui difficilement modélisable numériquement (Bercovici, 2003, Bercovici et al., 2000, Gueydan et al., 2014, Tackley, 2000). Les observations géophysiques, telles que l'imagerie tomographique, l'anisotropie sismique (e.g. Rychert et al., 2012, Schmerr, 2012) ou encore la conductivité électrique (e.g. Baba et al., 2006, Naif et al., 2013, Sarafian et al., 2015, Selway, 2015) sont de bons moyens pour comprendre ce qu'il se passe à l'intérieur de la Terre et donnent des informations cruciales qui permettent de perfectionner les modèles numériques simulant l'activité globale terrestre. De nombreux outils permettent d'expliquer les observations géophysiques, telles que les études de terrain (Précigout and Gueydan, 2009, Skemer et al., 2013, Warren and Hirth, 2006) mais également les expériences en laboratoire qui permettent de déterminer les processus géologiques se produisant en profondeur (Hashim et al., 2013, Pommier et al., 2015, Sifré et al., 2014).

La taille des cristaux dans les roches polycristallines est un paramètre crucial, qui affecte à la fois les observations géophysiques du manteau (e.g. l'atténuation des ondes sismiques, Behn et al., 2009), la perméabilité des roches (e.g. pour la modélisation numérique des écoulements biphasiques, Richard et al., 2012) ainsi que leur rhéologie (Hirth and Kohlstedt, 2003). Cependant, les roches polycristallines tendent à minimiser l'énergie interne du système, ce qui entraîne une variation de la taille de grains moyenne avec le temps (Atkinson, 1988, Burke and Turnbull, 1952). Cette dernière notion constitue le coeur de ce manuscrit de thèse. De nombreux facteurs influencent la taille de grains, en particulier les processus de déformation qui sont gouvernés par les défauts intergranulaires (e.g. les dislocations et les disinclinaisons Cordier et al., 2014, Karato, 2008). Dans ce cas, nous observons une réduction de la taille de grains moyenne à travers la recristallisation dynamique, par exemple, processus majeur dans le domaine de fluage dislocation (Karato et al., 1980, Urai et al., 1986). Un transfert vers le domaine du fluage diffusion ou glissement aux joints de grains (processus de déformation influencée par la taille de grains) est alors initiée lorsque la taille de grains moyenne devient suffisamment petite. Ce changement de régime de déformation permet donc à la croissance cristalline de devenir le processus majeur dans le cycle évolutif de la taille des grains. Cependant, ceci implique un cycle mécanique complexe : une compétition s'établit entre les processus de croissance de grains et de recristallisation dynamique, qui est induite par l'alternance des régimes de déformation des domaines dépendant et indépendant de la taille de grains (Austin and Evans, 2007, Hall and Parmentier, 2003, Pearce and Wheeler, 2011).

De plus, l'évolution de la taille de grains est particulièrement critique pour extrapoler de nos échelles de temps à celles de l'ordre géologique. L'extrapolation des expériences en laboratoire aux conditions naturelles nécessitent alors une loi de croissance précise en prenant appui sur la théorie/les mathématiques qui régissent la physique de la croissance de grains.

La croissance de grains est définie par une augmentation de la taille de grains d'un matériau. Ce processus peut être divisé en deux catégories : (i) un processus continu, durant lequel les grains du matériau grossissent de manière uniforme, appelé *croissance de grains normale*, et (ii)

un processus discontinu, *croissance de grains anormale* (ou recristallisation secondaire), pendant lequel certains gros grains grossissent au dépens des grains plus petits formant la matrice. Dans le cas de la croissance de grains normale, la taille et la forme des cristaux présentent des distributions étroites qui sont des marqueurs de l'indépendance au temps de ce type de processus (Fig. 1(a)). Au contraire, dans le cas de la croissance de grains anormale, la distribution de la taille de grains est bimodale puisque les gros grains phagocytent les plus petits constituant la matrice (Fig. 1(b)). Au bout d'un certain temps, les plus petits grains disparaissent complètement, permettant à la croissance de grains normale de reprendre le dessus (Fig. 1(b)).

En laboratoire, la croissance de grains est caractérisée en mesurant la taille des cristaux des agrégats polycristallins expérimentaux. Les paramètres de croissance sont alors définis empiriquement grâce à la formulation suivante (Atkinson, 1988, Burke and Turnbull, 1952) :

$$r_f^n - r_i^n = t \cdot k_0 \exp\left(-\frac{E_a}{RT}\right) \tag{2}$$

où r_f et r_i sont les rayons des grains finaux et initiaux (en m), n est l'exposant à la taille des grains, t, la durée expérimentale (en s), k_0 est le terme pre-exponentiel qui dépend du type de matériau étudié (en $\mathrm{m^n\,s^{-1}}$), E_a est l'énergie d'activation pour la croissance de grains (en $\mathrm{J\,mol^{-1}}$), R, la constante des gaz parfaits (en $\mathrm{J\,K^{-1}\,mol^{-1}}$) et T, la température absolue (en K). L'exposant à la taille de grain, n, doit cependant être préalablement établi avant de procéder à la détermination des valeurs des autres paramètres de Eq. (2). Ces derniers sont alors définis en procédant à une régression linéaire des données, en présentant celles-ci dans un graphique du type $\log_{10}(r_f^n - r_i^n)$ vs. $\log_{10}(t)$. Déterminer la valeur de l'exposant à la taille des grains est alors critique quant à l'extrapolation des données en laboratoire à des durées plus longues, e.g. de l'ordre géologique.

Un grand nombre d'études expérimentales ont été réalisées afin de déterminer une loi de croissance pour l'olivine, dans des conditions statiques. Ces études se sont plus spécifiquement penchées sur l'influence sur la croissance de l'olivine par des éléments, telles que l'eau (Karato, 1989, Ohuchi and Nakamura, 2007b), la fugacité d'oxygène (f_{O_2} Nichols and Mackwell, 1991), la présence de liquide silicaté (Cabane et al., 2005, Faul and Scott, 2006) ou encore la présence de phase secondaire solide ou gazeux, par exemple les pores (Karato, 1989, Nichols and Mackwell, 1991), les orthopyroxènes (Hiraga et al., 2010, Tasaka and Hiraga, 2013) et les clinopyroxènes (Ohuchi and Nakamura, 2007a,b). Ces études ont utilisées deux types d'olivine pour caractériser la croissance de grains : (i) des polycristaux d'olivine naturelle (généralement de l'olivine de San Carlos $\sim$ Fo_{90}) et (ii) de l'olivine fabriquée synthétiquement (soit à base de solution-gelation (sol-gel), soit à base de mélange de nano-oxydes). Ces expériences ont été réalisées à différentes températures allant de 1200 à 1450 °C, des pressions allant de la pression atmosphérique (1-atm) jusqu'à 1.2 GPa et pour des durées expérimentales allant jusqu'à 763 h ($\sim$ 32 jours). En procédant à une régression linéaire de cette base de données sur la croissance de grains de l'olivine, nous observons que la valeur de l'exposant à la taille des grains varie considérablement d'une étude à l'autre. En général, cet exposant est cependant contraint entre 4 et 5.

Les différentes études sur la croissance de grains d'olivine indiquent une très grande disparité quant aux paramètres de la loi de croissance. Aujourd'hui, il n'existe toujours pas de loi de croissance sans équivoque qui permettrait d'être appliquée aux expériences de rhéologie, mais surtout, transposables aux conditions géologiques naturelles.

L'objectif de cette thèse est donc d'augmenter la base de données sur la croissance de grains d'olivine en réalisant des expériences haute température/haute pression, et de confronter les résultats expérimentaux ainsi obtenus à la base de données pré-existantes. Il en découlera ainsi une loi de croissance d'olivine formelle qui se basera sur les processus physiques adéquats.

Dans ce manuscrit de thèse, j'utilise les données expérimentales sur la croissance d'olivine publiées dans la littérature. Ces données sont résumées dans la Fig. 2. Pour comparer les données les unes autres, l'exposant à la taille de grains a été fixé à $n = 4.37$, qui correspond à la moyenne

de n déterminée dans ces différentes études. Cette figure montre les taux de croissance (i.e. $(G_f^n - G_i^n)/t$, G étant le diamètre du grain) en fonction de la température réciproque absolue. Nous observons ainsi deux effets principaux : (i) les expériences réalisées sous condition réellement anhydre (pression atmosphérique, symboles ouverts sur la Fig. 2, Hiraga et al., 2010, Karato, 1989, Nichols and Mackwell, 1991, Tasaka and Hiraga, 2013) et (ii) les expériences comportant de l'eau et/ou du liquide silicaté (symboles orange et bleu), réalisées à haute pression (Cabane et al., 2005, Faul and Scott, 2006, Ohuchi and Nakamura, 2007a,b, Ohuchi et al., 2010). Cette figure montre bien que les agrégats contenant des liquides (silicatés ou acqueux) présentent des taux de croissance plus rapides que les agrégats réellement anhydres. Ceci suggère donc deux régimes de croissance, notamment un régime lent sous condition anhydre et un régime rapide en présence de liquide.

Ce manuscrit de thèse est ainsi divisé en trois grands chapitres. Le *premier chapitre* présente la base de données de croissance d'olivine anhydre, ainsi que la croissance de grains d'un point de vue théorique/thermodynamique. J'établis dans ce chapitre une loi de croissance d'olivine anhydre en me basant sur les propriétés de diffusion dans les agrégats d'olivine anhydre. Le *deuxième chapitre* résume les expériences de croissance d'olivine en présence de liquide (silicaté ou acqueux) réalisées au laboratoire de l'Institut des Sciences de la Terre d'Orléans (ISTO), et qui sont ensuite comparées aux données de la littérature sur des agrégats de même composition. Dans ce chapitre y est inscrit une partie théorique sur la croissance de grains en présence de liquide, qui sera utilisée pour déterminer une loi de croissance combinant à la fois les processus de croissance anhydre et de croissance en présence de liquide.

Le *chapitre trois* concerne un autre paramètre physique fondamental au fonctionnement de notre planète, notamment la viscosité. Ce chapitre est sous format article qui a été publié dans *Earth and Planetary Science Letters* et présente des données expérimentales de mesure de viscosité et de conductivité électrique de roches crustales partiellement fondues. Ces expériences ont été réalisées dans une presse Paterson (autoclave à chauffage interne équipé de modules de déformation) avec des métapélites himalayennes afin de mieux comprendre les anomalies géophysiques détectées sous le système orogénique Tibéto-Himalayen.

À la suite de la *bibliographie*, le lecteur trouvera *quatre annexes*, dans lesquelles (A) je démontre que l'exposant à la taille de grains n ne peut pas être défini sans équivoque avec le formalisme de Eq. (2), (B) je décris les méthodes de détermination de taille de grains, l'effet de coupe, les incertitudes liées à la mesure de la taille de grains, ainsi qu'un tableau présentant la base de données expérimentales complète sur la croissance de grains d'olivine, (C) je présente des figures complémentaires du chapitre 2 et (D) je présente un court projet de recherche accepté par le Deutscher Akademischer Austauschdienst (DAAD, Allemagne) pour une durée de six mois au Helmholtz-Zentrum Potsdam – Deutsches GeoForschungsZentrum (GFZ) à Potsdam (Allemagne). Ce projet explique la nécessité de réaliser de l'imagerie nanotomographique des films de liquide silicaté dans les agrégats d'olivine partiellement fondus afin de mieux comprendre les propriétés de mouillage des échantillons à faible taux de fusion. Un test de faisabilité est introduit dans cette annexe.

Chapter 1

On the theory and experimental investigations of dry olivine grain growth

Contents

Summary

As outlined in the introduction, two types of growth rates are observed from previously published experimental studies. In this chapter, we present the atmospheric olivine grain growth experiments that indicate dry and slow grain growth rates. The empirical growth laws deduced from these studies display contrasting values, in particular on the grain size exponent, n. The atmospheric grain growth experiments are therefore briefly introduced and then followed by a theoretical section explaining the physics governing static grain growth in a single-phase polycrystalline aggregate. Starting with the Burke and Turnbull (1952) analysis, I have derived the ruling equations for grain growth from the total grain volume change, Fick's first law and the driving force for grain boundary migration. I thereby establish the rate-law equations considering that grain growth is either rate-limited by grain boundary or lattice diffusion.

In the following section, I show that the discrepancies on the empirically determined values for olivine grain growth can be reconciled by using the existing data on the diffusion properties of dry olivine aggregates. Application of grain boundary and lattice diffusion coefficients to olivine grain growth indicates that diffusion of silicon at grain boundaries is the rate-limiting factor. From the atmospheric olivine grain growth database, the effective grain boundary width was determined ($\delta = \sim 30\,\text{nm}$), which is a factor 30 larger than the structural grain boundary width ($\delta = \sim 1\,\text{nm}$, Hiraga and Kohlstedt, 2007).

I then discuss the resulting diffusion-limited grain growth law with the empirical laws determined in the previously published atmospheric olivine grain growth experiments and extrapolate these laws to geological time scales. The grain growth law derived in this chapter is then extrapolated to mantle depths, by investigating the known pressure effect on the grain boundary diffusion coefficient of Si (Fei et al., 2016). Water-undersaturated olivine solubility conditions are also considered through its effect on the Si grain boundary diffusion coefficient.

The grain growth equation determined in this chapter is then applied as a first-order approximation to an olivine-rich mantle under static conditions. Dynamic recrystallization is then briefly examined by reformulating the work of Hall and Parmentier (2003) and by applying it to the lithosphere-asthenosphere boundary.

Théorie et études expérimentales sur la croissance de l'olivine en condition anhydre

Comme démontré dans l'introduction, deux régimes de croissance sont observés pour les agrégats d'olivine. Ce chapitre se focalise sur les expériences de croissance d'olivine réalisées à pression atmosphérique et qui est, ainsi, caractéristique du régime de croissance anhydre. D'après les études précédemment publiées, il n'y a pas de valeur d'exposant à la taille de grains, n, sans équivoque. Ce chapitre présente ainsi dans un premier temps la base de données anhydres, puis dans un second temps, sera présentée une section théorique sur la croissance cristalline d'un point de vue thermodynamique. Les points clés physiques régissant la croissance de grains d'agrégats polycristallins monominéralogique sont alors mis en avant. En commençant avec l'analyse de Burke and Turnbull (1952), j'ai dérivé les lois régissant la croissance de grains grâce au changement de volume d'un grain, de la première loi de Fick et de la loi motrice pour la migration des joints de grains. J'établis ainsi les lois de croissance en considérant qu'elles sont soit limitées par la diffusion au joint de grains, soit limitées par la diffusion dans le volume du grain.

La section suivante montre que les contradictions sur les paramètres de croissance, préalablement établis dans la littérature, peuvent être réconciliées en utilisant les données expérimentales sur les propriétés de diffusion d'agrégats d'olivine anhydre. La diffusion au joint de grains de la silice, constituant ionique de l'olivine le plus lent, permet donc de caractériser de manière marquante la loi de croissance d'olivine anhydre. La taille effective du joint de grains, épaisseur sur la laquelle la diffusion s'opère, est ainsi déterminée à $\sim 30\,\text{nm}$, qui est 30 fois plus importante que la taille structurale du joint de grains ($\sim 1\,\text{nm}$, Hiraga and Kohlstedt, 2007).

Je discute ensuite la loi de croissance déterminée dans cette étude en la comparant avec celles précédemment publiées. Ces différentes lois sont extrapolées aux échelles de temps géologiques, montrant des tailles de grains fondamentalement différentes de plusieurs ordres de grandeur. Une extrapolation aux profondeurs du manteau est également réalisée en utilisant l'effet de pression connu sur le coefficient de diffusion aux joints de grains de Si (Fei et al., 2016). L'effet de l'eau est également considéré en utilisant le coefficient de diffusion aux joints de grains de Si en condition hydratée.

À la fin de ce chapitre, le lecteur trouvera une courte discussion autour d'un manteau supérieur riche en olivine. La taille de grains du manteau supérieur est donc calculée pour chaque profondeur en suivant un géotherme de 10 My. Je considère enfin le cas de la recristallisation dynamique en reformulant les travaux de Hall and Parmentier (2003) et en appliquant cette reformulation à la frontière lithosphère/asthénosphère.

1.1 Experimentally-derived olivine grain growth

Grain growth kinetics are classically investigated through experiments, where grain sizes of polycrystalline aggregates are measured in order to empirically determine the grain growth parameters, which is of the form (Atkinson, 1988, Burke and Turnbull, 1952):

$$r_f^n - r_i^n = t \cdot k_0 \exp\left(-\frac{E_a}{RT}\right) \tag{1.1}$$

with r_f and r_i, the final and initial grain radii (in m), n, the grain size exponent, t, the time (in s), k_0, a material-dependent pre-exponential factor (in $\mathrm{m^n\,s^{-1}}$) and E_a, the empirical activation energy for grain growth (in $\mathrm{J\,mol^{-1}}$). These parameters are usually determined by a linear least squares fit of the data in a $\log_{10}(r_f^n - r_i^n)$ vs. $\log_{10}(t)$ plot, where the grain size exponent, n, must be previously ascertained.

In order to determine the growth kinetics of melt and water-free olivine aggregates, a number of studies have conducted experiments under atmospheric conditions by using natural San Carlos olivines (Karato, 1989, Nichols and Mackwell, 1991) or synthetic forsterite aggregates (Hiraga et al., 2010, Tasaka and Hiraga, 2013). Different effects have been investigated in these experimental studies, in particular the oxygen fugacity effect, f_{O_2} (Nichols and Mackwell, 1991) and the presence of secondary phases, such as pores or orthopyroxenes (Hiraga et al., 2010, Karato, 1989, Nichols and Mackwell, 1991, Tasaka and Hiraga, 2013).

The empirically-derived values for grain growth of olivine aggregates are very different in these studies. The main difference arises from the grain size exponent value, which has drastic implications on the values of the other parameters. Since n varies from 2 (Karato, 1989) to 9.2 (Hiraga et al., 2010), comparison of the existing data is not straightforward. Furthermore, it has been shown that n can be fitted by a wide range of values (see also Appendix A; German et al., 1997), which infers uncertain application of these growth laws to geological length and time scales. In addition, we would like to highlight that the n values from Hiraga et al. (2010), Tasaka and Hiraga (2013) were determined by considering a negligible effect of the starting grain size (i.e. $G_f^n - G_i^n \approx G_f^n$, with G, the grain diameter). This assumption is however delicate since once raised to the power n, the initial grain size becomes important, particularly for experiments that have already underwent grain coarsening (e.g. experimental durations $>0.5\,\mathrm{h}$). The main disagreements on the empirical values from these studies therefore justifies the importance of determining an unambiguous grain growth law for dry melt-free olivine aggregates.

As a consequence, we have plotted the raw experimental data of these studies in a $\log_{10}$ growth rate ($(G_f^2 - G_i^2)/t$) vs. absolute reciprocal temperature plot, with $n = 2$ as will be demonstrated in the next section. As expected from Eq. (1.1), experimental olivine grain size increases with increasing temperature. Furthermore, all the experimental data seem to lay on the same trends, where the effects of pores and of starting composition (natural San Carlos olivine vs. synthetic forsterite) are not distinguishable.

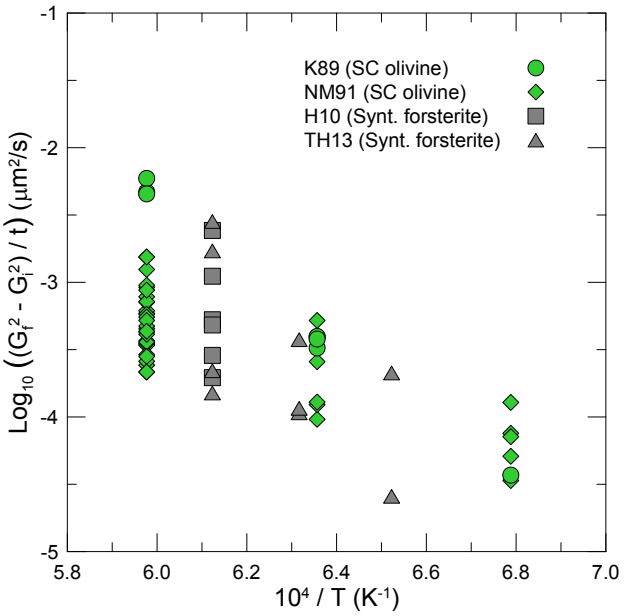

Figure 1.1 – Atmospheric pressure olivine grain growth experiments as a function of absolute reciprocal temperature. Experiments are from Karato (1989) (K89), Nichols and Mackwell (1991) (NM91), Hiraga et al. (2010) (H10) and Tasaka and Hiraga (2013) (TH13). Green symbols represent San Carlos olivine aggregates containing pores whereas gray symbols mark the synthetic forsterite samples containing <3 wt. % orthopyroxenes. The experiments from NM91 (green diamonds) were conducted under varying f_{O_2} whereas those of K89 (green circles) were performed at fixed f_{O_2} (near the iron/wüstite buffer). Since the samples from H10 and TH13 (gray squares and triangles, respectively) were exempt of iron, the f_{O_2} was not buffered in their experiments.

1.2 Theory behind grain growth

In a polycrystalline aggregate, it is the migration of the grain boundaries that leads to the evolution of the microstructure. A grain boundary (or homophase interface) is defined as the interface transition between two single crystals of the *same* phase with *different* crystallographic orientations. This typically curved transitional region is considered as a planar defect of a few atoms in thickness and can be structurally viewed as two-dimensional imperfections in a crystalline material. The structure of grain boundaries is dependent on the local displacements at the atomic level and therefore provide high diffusion pathways that are not available in single crystals.

Grain growth occurs by the minimization of the Gibbs free energy (ΔG) of the system. Three possible driving forces act on this minimization: (i) a reduction of the curvature of the grain boundary (the boundary will move towards its own center of curvature), (ii) an externally applied pressure (development of a pressure gradient) and (iii) a chemical reaction arising from a chemical gradient. In this section, we will be demonstrating the theoretical diffusion-controlled grain growth equations that are summarized in Table 1.1.

The driving force, F_{gb} (in N), is related to the chemical potential, $d\mu$ (in $\mathrm{J\,mol^{-1}}$), and the pressure gradient, ΔP (in Pa), through (Burke and Turnbull, 1952):

$$F_{gb} = \frac{d\mu}{dx} = \frac{\Omega d(\Delta P)}{dx} \tag{1.2}$$

where $dx = \delta$, the grain boundary width (in m) and Ω is the molar volume of the growing crystal (in $\mathrm{m^3\,mol^{-1}}$). The pressure gradient is defined by the Young-Laplace equation, of the form:

Table 1.1 – Single-phase growth kinetics.

Mechanism	Equation[(a)]
Lattice diffusion	$r_f^3 - r_i^3 = 3\dfrac{\alpha \cdot \gamma_{gb} \cdot \Omega^2 \cdot C^i \cdot D^i_{lat}}{\xi \cdot RT}\, t$
Grain boundary diffusion	$r_f^2 - r_i^2 = 2\dfrac{\alpha \cdot \gamma_{gb} \cdot \Omega^2 \cdot C^i \cdot D^i_{gb}}{\delta_{gb} \cdot \xi \cdot RT}\, t$

[(a)] i denotes the slowest ionic species.

$$\Delta P = \gamma \left(\frac{1}{r_1} + \frac{1}{r_2} \right) \tag{1.3}$$

where γ is the interface energy (in $\mathrm{J\,m^{-2}}$) and r_1 and r_2 are the principal radii of curvature of the boundary (in m). If we assume that the grain can be approximated by a sphere of radius r, then $r = r_1 = r_2$, which leads to $\Delta P = \gamma\alpha/r$, with $\alpha = 2$.

Furthermore, the rate of total grain volume change, dV/dt, is related to the flux of atoms, J, through:

$$\frac{dV}{dt} = 4\pi r^2 \frac{J \cdot \Omega}{\xi} \tag{1.4}$$

with ξ, a stoichiometric coefficient defined as the number of moles of the considered growing grain due to the transport of one mole of species i. Additionally, dV/dt is also related to the grain boundary volume, $4/3\pi(r+dr)^3$ by:

$$\begin{aligned} \frac{dV}{dt} &= \left(\frac{4}{3}\pi(r+dr)^3 - \frac{4}{3}\pi r^3 \right) \frac{1}{dt} \\ &= 4\pi r^2 \frac{dr}{dt}. \end{aligned} \tag{1.5}$$

Therefore, Eqs. (1.4) and (1.5) yield the following relation:

$$\frac{dr}{dt} = \frac{J \cdot \Omega}{\xi}. \tag{1.6}$$

Furthermore, according to Fick's first law:

$$J = -\frac{D^i \cdot C^i}{RT} \frac{d\mu}{dx} \tag{1.7}$$

with D^i, the diffusion coefficient of species i (in $\mathrm{m^2\,s^{-1}}$), C^i, the concentration of i (in $\mathrm{mol\,m^{-3}}$), R, the gas constant (in $\mathrm{J\,K^{-1}\,mol^{-1}}$), T, the absolute temperature (in K), and $dx = \delta$ and $dx = r$ for grain boundary (GB) and lattice diffusion-limited grain growths, respectively. As a result, by combining Eqs. (1.2), (1.6) and (1.7), the average grain growth rate is:

$$\frac{dr}{dt} = \frac{\alpha \cdot \gamma \cdot \Omega^2 \cdot C^i \cdot D^i}{dx \cdot r \cdot \xi \cdot RT}, \tag{1.8}$$

which, in the case of GB diffusion-limited grain growth, leads by integration to the following final form:

$$r_f^2 - r_i^2 = 2\frac{\alpha \cdot \gamma \cdot \Omega^2 \cdot C^i \cdot D^i_{gb}}{\delta \cdot \xi \cdot RT}\, t \tag{1.9}$$

and, in the case of lattice diffusion-limited grain growth, Eq. (1.8) leads to the integrated form of:

$$r_f^3 - r_i^3 = 3\frac{\alpha \cdot \gamma \cdot \Omega^2 \cdot C^i \cdot D^i_{lat}}{\xi \cdot RT}\, t. \tag{1.10}$$

In the latter equations, r_f is the grain radius (in m) at time t (in s) and r_i is the initial grain radius at time $t = 0\,\mathrm{s}$. Additionally, it is important to mention that Eqs. (1.9) and (1.10) yield substantial different final grain sizes when applied to geological time scales due to the different grain size exponents.

Note that if the grain diameter, G, is used instead of the grain radius, r, then Eqs. (1.9) and (1.10) become respectively:

$$G_f^2 - G_i^2 = 8\,\frac{\alpha \cdot \gamma \cdot \Omega^2 \cdot C^i \cdot D^i_{gb}}{\delta \cdot \xi \cdot RT}\, t \tag{1.11}$$

$$G_f^3 - G_i^3 = 24\,\frac{\alpha \cdot \gamma \cdot \Omega^2 \cdot C^i \cdot D^i_{lat}}{\xi \cdot RT}\, t. \tag{1.12}$$

1.3 Olivine grain growth predictions from diffusion data

In this section, we will be showing that the discrepancies on the empirically determined values for olivine grain growth can be reconciled by using existing data on the diffusion properties of dry olivine aggregates. We will show here that the rate-limiting process during olivine grain growth is the diffusion of Si at GB and that by applying the GB diffusion-limited grain growth equation (Eq. (1.9)), we were able to determine the length-scale upon which GB diffusion effectively operates, i.e. the effective dry grain boundary width, δ.

1.3.1 Diffusion coefficients

In order to apply Eqs. (1.9) and (1.10), we have taken dry GB and lattice diffusion coefficients in olivine aggregates from the literature. Three ionic species have been considered, namely magnesium, oxygen and silicon for both lattice (Chakraborty et al., 1994, Dohmen et al., 2002, Fei et al., 2012) and grain boundaries (Farver and Yund, 2000, Farver et al., 1994, Fei et al., 2016, Gardés and Heinrich, 2011). Since diffusion is a thermally-activated process, it follows an Arrhenius law of the form:

$$\begin{aligned} D^i_{lat} &= D^i_{lat,0} \exp\left(-\frac{E_a}{RT}\right) \\ D^i_{gb} &= D^i_{gb,0} \exp\left(-\frac{E_a}{RT}\right) \\ \delta D^i_{gb} &= \delta D^i_{gb,0} \exp\left(-\frac{E_a}{RT}\right) \end{aligned} \tag{1.13}$$

where D^i_{lat} and D^i_{gb} are the diffusion coefficients of the lattice and grain boundary, respectively (in $\mathrm{m^2\,s^{-1}}$), $D^i_{lat,0}$ and $D^i_{gb,0}$ are the pre-exponential factors of the lattice and grain boundary diffusion coefficients, respectively (in $\mathrm{m^2\,s^{-1}}$), δ is the grain boundary width (in m), and E_a, the activation energy for diffusion (in $\mathrm{J\,mol^{-1}}$). The Arrhenius parameters for dry GB and lattice diffusions are summarized in Table 1.2 and the resulting diffusion coefficients as a function of temperature are shown in Fig. 1.2, with a structural grain boundary width of $\delta = 1\,\mathrm{nm}$ (Hiraga and Kohlstedt, 2007). Magnesium thus appears to be the fastest ionic species along olivine grain

boundaries and within the lattice whereas silicon seems to be the slowest ionic species in both GB and lattice diffusions.

Table 1.2 – Arrhenius parameters for dry lattice and grain boundary diffusions.

Diffusion type	Species i	D_0^i ($m^2\,s^{-1}$)	E_a ($kJ\,mol^{-1}$)	Reference
Lattice diffusion	Mg	$5.60 \cdot 10^{-8}$	275 ± 25	Chakraborty et al. (1994)
	O	$4.57 \cdot 10^{-9}$	338 ± 14	Dohmen et al. (2002)
	Si	$2.51 \cdot 10^{-7}$	410 ± 30	Fei et al. (2012)
GB diffusion	Mg	$7.70 \cdot 10^{-10}$	376 ± 47	Farver et al. (1994)
	O	$1.95 \cdot 10^{-3}$	329 ± 30	Gardés and Heinrich (2011)
	Si	$5.01 \cdot 10^{-8}$	220 ± 30	Fei et al. (2016)

The Arrhenius law is of the form $D^i = D_0^i \exp(-E_a/RT)$. δ is assumed to be 1 nm when δD_{gb}^i was given in the literature instead of solely D_{gb}^i.

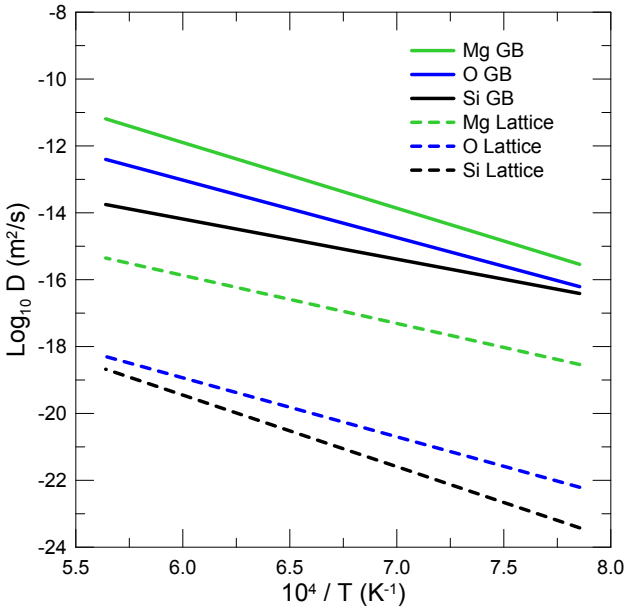

Figure 1.2 – Dry grain boundary (full lines) and lattice (dashed lines) diffusion coefficients as a function of absolute reciprocal temperature. Arrhenius laws are taken from Fei et al. (2016) for D_{gb}^{Si}, Farver et al. (1994) for D_{gb}^{Mg}, Gardés and Heinrich (2011) for D_{gb}^{O}, Fei et al. (2012) for D_{lat}^{Si}, Chakraborty et al. (1994) for D_{lat}^{Mg}, Dohmen et al. (2002) for D_{lat}^{O}.

1.3.2 Calculated dry olivine grain growth rates

Although diffusion-controlled grain growth appears to be limited by the slowest ionic species, we have simulated grain growths according to Eqs. (1.9) and (1.10) by using the diffusion coefficients presented in Table 1.2. These results are presented in a calculated final grain size vs. $\log_{10}(t)$ plot in Fig. 1.3, where the temperature, initial grain size and structural grain boundary width are fixed at 1200 °C, 2 µm and 1 nm, respectively. The other parameters in Eqs. (1.9) and (1.10) are $\gamma = 0.9\,J\,m^{-2}$ (Cooper and Kohlstedt, 1982), $\Omega = 43.8\,cm^3\,mol^{-1}$ for forsterite (Gottschalk, 1997) and $C^i = \xi/\Omega$ (Joesten, 1991).

Calculations therefore indicate that lattice diffusion-limited olivine grain growth rates are expected to be considerably slow. Indeed, Fig. 1.3 clearly shows that for D_{lat}^{Mg} grain sizes moderately start to increase after 12 days whereas for D_{lat}^{O} and D_{lat}^{Si} 114 years are needed to detect a change in grain sizes. On the contrary, GB diffusion-limited grain growth rates are predicted to be faster by several orders of magnitude, as expected by the diffusion coefficient behaviors (Fig. 1.2). Considering $\delta = 1\,\text{nm}$, grain growth is instantly initiated for D_{gb}^{Mg} and D_{gb}^{O} whereas olivine aggregates begin to coarsen after 3 h for D_{gb}^{Si}.

To assess which diffusion mechanism is the limiting factor for olivine grain growth, we have indicated in Fig. 1.3 the measured experimental grain sizes in olivine aggregates under the same temperature and initial grain size conditions (Nichols and Mackwell, 1991). Whether lattice diffusion or GB diffusion with $\delta = 1\,\text{nm}$ is used, our model does not calculate the appropriate grain growth rates. Therefore, we have simulated Si GB diffusion-limited grain growths by considering wider grain boundaries, i.e. $\delta = 10$ and 100 nm. As a consequence, Fig. 1.3 shows that the experimental grain sizes are well reproduced with $\delta \sim 10\,\text{nm}$.

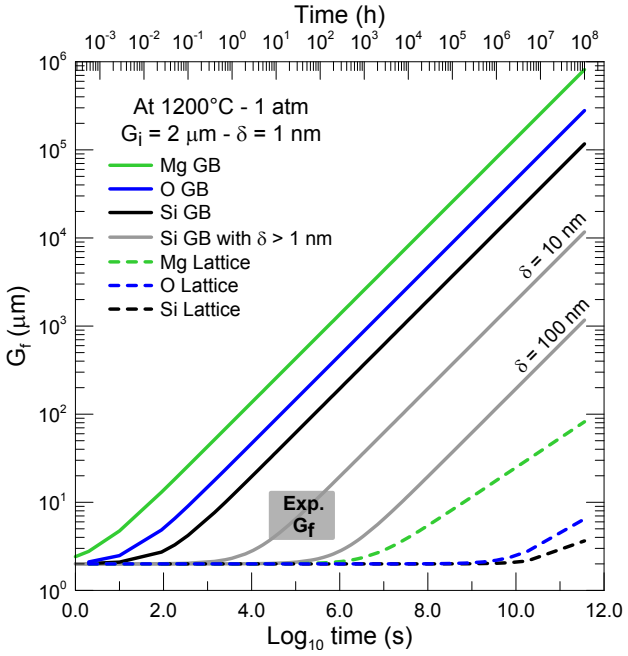

Figure 1.3 – Theoretical final grain sizes as a function of time considering different lattice and grain boundary diffusion coefficients. Temperature is fixed at 1200 °C, initial grain size is 2 µm and the grain boundary width is 1 nm (Hiraga and Kohlstedt, 2007). The gray box corresponds to experimental grain sizes measured under the same temperature and initial grain size conditions (Nichols and Mackwell, 1991). Grain growth rates were also simulated with wider grain boundaries (10 and 100 nm).

Since growth rate of olivine aggregates is limited by the diffusion of Si at GB, we have used the 1 atm database on natural and synthetic olivine aggregates to determine the effective grain boundary width, which corresponds to the permeable zone for diffusion. As a result, least-squares fit to the data yield $\delta = 29.21^{+37}_{-16}\text{nm}$, where the uncertainties on δ were calculated by solely propagating those on the diffusion coefficient. Since the uncertainties on D_{gb}^{Si} are greater than those on the measured grain sizes, we were able to neglect the latter. The effective grain boundary thickness from this study is in good agreement with a transmission electron microscope study on diffusion in garnet (Marquardt et al., 2011) that showed that the effective and structural grain boundary thicknesses are of 18 and 2 nm, respectively.

Despite varying experimental conditions (e.g. varying f_{O_2} and olivine chemical compositions),

our model appropriately reproduces the experimental grain sizes within uncertainties as shown in Fig. 1.4. However, we would like to emphasize that the grain sizes at T ≥1300 °C from the study of Karato (1989) are off trend, i.e. our model underestimates the growth rates. This could be due to the presence of pores at grain boundaries in the experimental samples of Karato (1989) as previously hypothesized (Austin and Evans, 2007, Behn et al., 2009, Evans et al., 2001, Faul and Scott, 2006, Nichols and Mackwell, 1991), which would in theory considerably decrease grain growth rates. However, this hypothesis is highly uncertain since the experimental samples in the study of Nichols and Mackwell (1991) also contain a significant amount of pores and their growth rates are clearly well constrained by our model (Fig. 1.4). Since the measured grain sizes are larger than those modeled in this study, we discard the pore effect and suggest that the samples used at high temperatures in the study of Karato (1989) contained a small amount of melt, therefore increasing growth rates (see Chapter 2 for the melt effect).

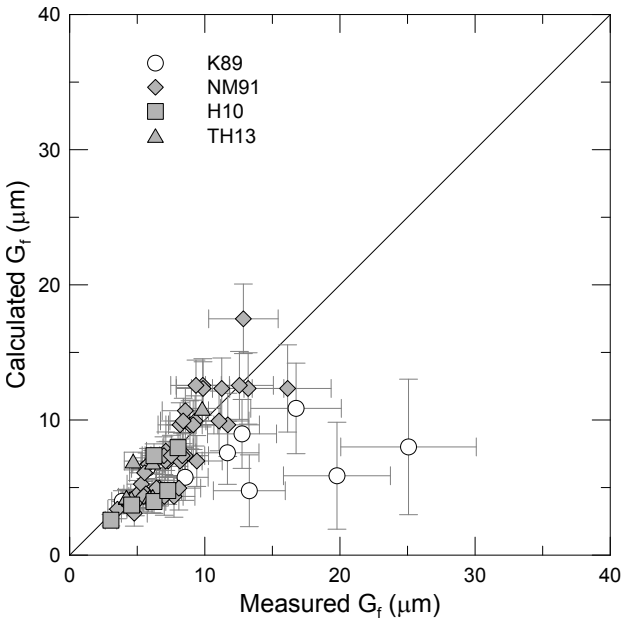

Figure 1.4 – Calculated vs. measured final grain sizes for dry melt-free olivine grain growth. The open symbols indicate that the model underestimates the growth rates for the study of Karato (1989) for temperatures ≥1300 °C. Experiments are from Karato (1989) (K89), Nichols and Mackwell (1991) (NM91), Hiraga et al. (2010) (H10) and Tasaka and Hiraga (2013) (TH13).

1.4 Discussion

1.4.1 Comparison of the existing models on olivine grain growth

To compare the existing models on olivine grain growth, we have used the Arrhenius parameters from the studies of Hiraga et al. (2010), Karato (1989), Nichols and Mackwell (1991), Tasaka and Hiraga (2013) to calculate the grain size as a function of time (Fig. 1.5). Since the model of Hiraga et al. (2010) was only elaborated for a fixed temperature of 1360 °C, the initial conditions of the models in Fig. 1.5 are fixed at the same temperature, an initial grain size of 1.91 µm and an effective grain boundary width of 29.21 nm for our model. Experimental grain sizes from the study of Hiraga et al. (2010) are also represented in Fig. 1.5 and are well reproduced by the empirical growth laws from Hiraga et al. (2010), Tasaka and Hiraga (2013) as well by our diffusion-limited model. Under these conditions, grain growth rates modeled by the Arrhenius

law of Nichols and Mackwell (1991) are too fast whereas those modeled by the empirical law of Karato (1989) are considerably slow. Furthermore, at 1360 °C and under static dry melt-free conditions, extrapolation of the growth models to geological time scales (e.g. $t \sim 1\,\mathrm{My}$) shows that sub-millimeter- to millimeter-scale grain sizes are expected according to the models from Hiraga et al. (2010), Nichols and Mackwell (1991), Tasaka and Hiraga (2013), whereas only a few tens of micrometer are predicted by the study of Karato (1989) because of slow growth kinetics. Our model, however, calculates greater grain sizes under these conditions, where for $t \sim 1\,\mathrm{My}$, grain sizes are expected to reach $\sim 1\,\mathrm{dm}$.

We would like to emphasize that this kind of extrapolation does not necessarily reflect real mantle conditions since other parameters are likely to influence grain size, notably secondary phases (e.g. pyroxenes, melt, fluids, Cabane et al. (2005), Faul and Scott (2006), Hiraga et al. (2010), Ohuchi and Nakamura (2007a,b), Ohuchi et al. (2010), Tasaka and Hiraga (2013)), deformation processes (Karato, 1989, Tasaka et al., 2013), where dynamic recrystallization is known to play a considerable part on grain growth (Austin and Evans, 2007, Behn et al., 2009, Evans et al., 2001, Hall and Parmentier, 2003, Karato, 1989), the presence of water (Karato, 1989, Ohuchi and Nakamura, 2007a,b, Ohuchi et al., 2010), particularly through its influence on D_{gb}^{Si} (Fei et al., 2016).

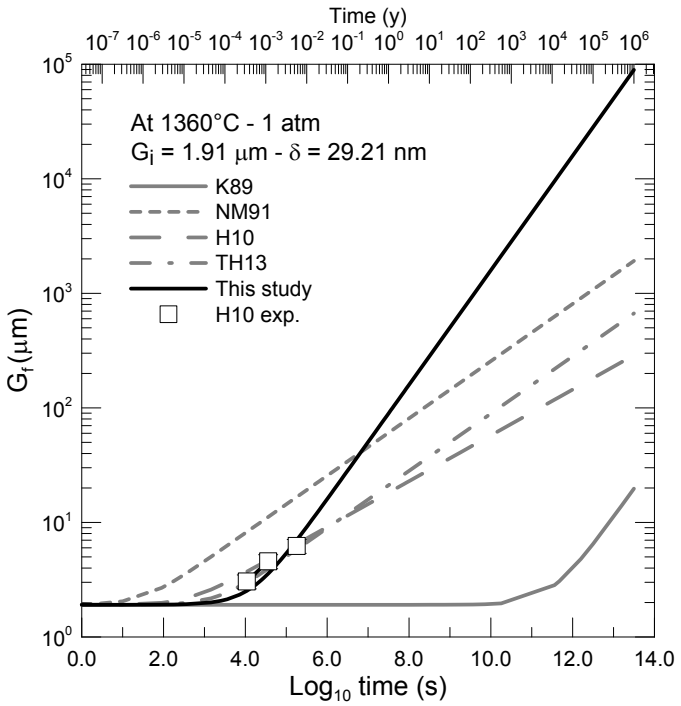

Figure 1.5 – Final calculated grain sizes as a function of time considering all atmospheric olivine grain growth models at 1360 °C and for an initial grain size of 1.91 µm. Squared symbols indicate the experimental final grain sizes from Hiraga et al. (2010) for the same experimental conditions. Experiments are from Karato (1989) (K89), Nichols and Mackwell (1991) (NM91), Hiraga et al. (2010) (H10) and Tasaka and Hiraga (2013) (TH13).

1.4.2 Pressure and water effects on grain size

Fei et al. (2016) have investigated the pressure and water effects on silicon diffusion at grain boundaries. The pressure effect was included in the Arrhenius law (Eq. (1.13)) with $E_a = \Delta H_a + P\Delta V$, where ΔH_a is the activation enthalpy for diffusion (in $\mathrm{J\,mol^{-1}}$), P is the pressure

(in Pa) and ΔV is the activation volume (in $m^3\,mol^{-1}$). In the study of Fei et al. (2016), the water effect was investigated solely at 8 GPa, with $D^{Si}_{gb,wet}$ as a function of temperature and water concentration within GB ($C^{H_2O}_{gb}$). For our modeling purposes and since we do not know with certainty the amount of water within olivine GB under mantle conditions, we have reformulated their GB diffusion law as a function of the bulk water content contained in olivine ($C^{H_2O}_{bulk}$), such that:

$$\delta D^{Si}_{gb,wet} = \delta D_{gb,wet,0} \left(C^{H_2O}_{bulk}\right)^r \exp\left(-\frac{\Delta H_{a,wet} + P\Delta V}{RT}\right) \tag{1.14}$$

with $\delta D_{gb,wet,0} = 6.88 \cdot 10^{-17}\,m^3\,s^{-1}$, $r = 0.16$, the concentration exponent, $\Delta H_{a,wet} = 225.63\,kJ\,mol^{-1}$ and $\Delta V = 4.29\,cm^3\,mol^{-1}$. It is important to note that water does not influence the value of ΔV (for comparison, Fei et al. (2016) found a dry activation volume of $4.0 \pm 0.7\,cm^3\,mol^{-1}$). Through the influence of pressure and water on the diffusion coefficient, we have thus explored their effects on grain size, as represented in Fig. 1.6. As indicated in Fei et al. (2016), pressure decreases the diffusion coefficient of Si at GB, which therefore decreases grain sizes by more than half an order of magnitude at constant duration (Fig. 1.6). For undersaturated olivine solubility conditions, an increase in $C^{H_2O}_{bulk}$ from 0 to 300 wt. ppm slightly increases the grain size. We can therefore expect that the small quantities of water present in olivine will not drastically modify grain sizes in the mantle if only normal grain growth is acting at depth.

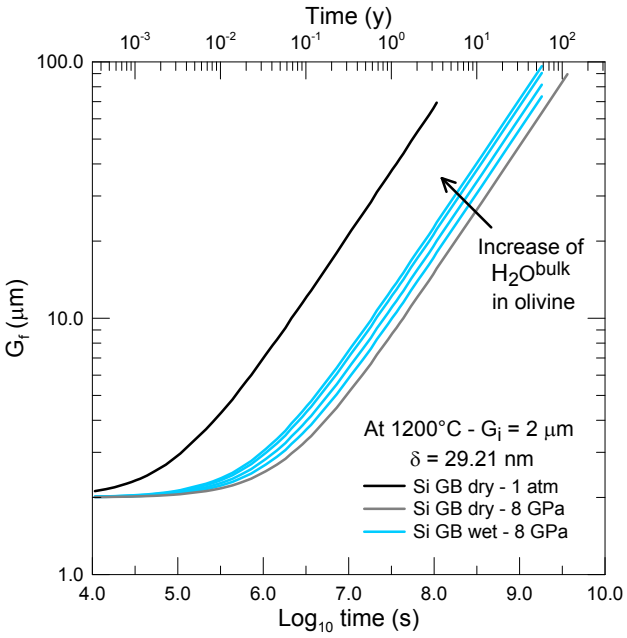

Figure 1.6 – Water effect on grain size at 1200 °C, an initial grain size of 2 µm and for bulk water contents in olivine ranging from 0 to 300 wt. ppm.

1.4.3 Application to an olivine-rich mantle

We use our model to determine the grain sizes in an olivine-rich mantle by considering an oceanic lithospheric geotherm of 100 My (Stixrude and Lithgow-Bertelloni, 2005). While this approach ignores secondary effects, such as the presence of liquids (i.e. melt or fluids), secondary phases (e.g. pyroxenes, garnet), it nevertheless provides a first-order approximation of the grain sizes prevailing in the mantle if normal grain growth (NGG) is the dominant mechanism acting

at depth. Fig. 1.7 illustrates the predicted grain sizes as governed by Eqs. (1.9) and (1.14), with $\delta = 29.21\,\text{nm}$, an arbitrary initial grain size of 1 µm, $C_{bulk}^{H_2O}$ contents of 0 and 150 wt. ppm and time spanning from 10 y to 10 My, where $t = 0$ represents the onset of olivine grain growth. Additionally, we would like to highlight that unlike at depths larger than 300 km, where it is possible to incorporate ∼500 wt. ppm H_2O in olivine, solubility of water in olivine is <50 wt. ppm for depths <100 km (Ardia et al., 2012, Hirschmann et al., 2009). If the water content is higher than its solubility in olivine, then partial melting could eventually take place (Fei et al., 2013, Naif et al., 2013, Sifré et al., 2014). The high water contents in this approach is to eventually show any significant differences with dry conditions.

For both dry and hydrated conditions, Fig. 1.7 shows that grain size increases with depth, which directly results from the temperature effect on both the diffusion of Si at GB (Eq. (1.13)) and on grain growth (Eq. (1.9)). Furthermore, as time increases, grain growth is initiated at shallower depths, e.g. grain growth under dry conditions (Fig. 1.7(a)) is initiated at ∼75 km depth after 10 y whereas grain size start to increase at ∼40 km depth after 10 My. Since we previously showed that water does not significantly influence grain growth, it is to no surprise that by adding 150 wt. ppm bulk water in olivine, the grain sizes do not show any substantial difference (Fig. 1.7(b)).

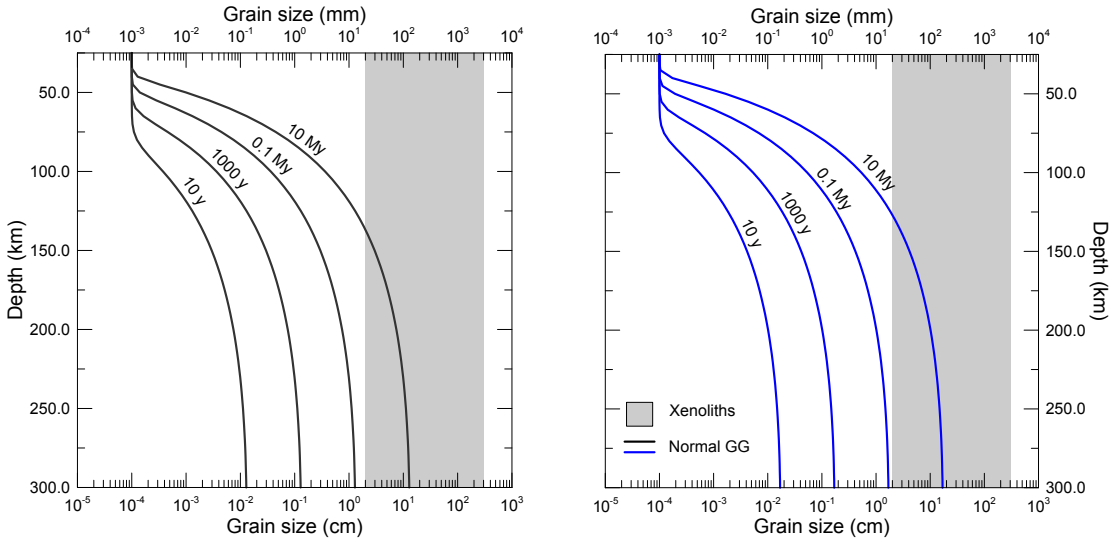

(a) Dry mantle olivine grain sizes. Initial grain size is 1 µm.

(b) Wet mantle olivine grain sizes with $C_{bulk}^{H_2O} = 150$ wt.ppm in olivine. Initial grain size is 1 µm.

Figure 1.7 – Prediction of grain sizes in the mantle as a function of depth for an oceanic lithospheric geotherm of 100 My (Stixrude and Lithgow-Bertelloni, 2005) by considering NGG governed by diffusion-limited GB processes for durations from 10 y to 10 My. Note that the hydrated case (Fig. 1.7(b)) is an overestimation of water solubility in olivine for depths <150 km (Ardia et al., 2012, Hirschmann et al., 2009). The gray zone indicates olivine grain sizes measured in mantle xenoliths for comparison (Evans et al., 2001, and references therein).

As mentioned above, deformation processes play an important role in determining the grain size, especially in the dislocation creep regime which substantially contributes to dynamic recrystallization (DR). An interesting geological application would be the lithosphere-asthenosphere boundary (LAB), where a mechanically strong mantle region (lithosphere) overlies a mechanically weak mantle region (asthenosphere), bounded between 50 and ∼80 km depth (Schmerr, 2012). A localized zone of intense deformation might therefore result at the LAB (Höink et al., 2011). Following the work of Hall and Parmentier (2003), we have calculated the grain size undergoing both NGG and DR, i.e.:

$$\frac{dG}{dt} = \left.\frac{dG}{dt}\right|_{NGG} - \left.\frac{dG}{dt}\right|_{DR} \tag{1.15}$$

where $dG/dt|_{NGG}$ and $dG/dt|_{DR}$ stands for NGG- and DR-affected grain growth rates, respectively. This application is however a preliminary step, which will be investigated in further details in the near future (namely for the defense presentation). Firstly, we have calculated the equilibrium time, t_{eq}, needed to reach a steady-state grain size, in other words, the equilibrium grain size as $t \to \infty$ resulting from balanced rates of NGG and DR, so that (Behn et al., 2009, Hall and Parmentier, 2003):

$$t_{eq} = (n\lambda\dot{\epsilon}_{disl})^{-1} \tag{1.16}$$

with $n = 2$, the grain size exponent, λ, the reciprocal of the accumulated strain required to reach a new equilibrium grain size after an instantaneous change in strain rate and $\dot{\epsilon}_{disl}$, the dislocation creep rate. While Hall and Parmentier (2003) showed that $0.5 < \lambda < 2$ from the deformation experiments performed by Bystricky et al. (2000), we have chosen to use here $\lambda = 1$. Natural deformation rates are known to be constrained between $1 \cdot 10^{-10}$ and $1 \cdot 10^{-15}\,\mathrm{s}^{-1}$, thus we apply $\dot{\epsilon}_{disl} = 1 \cdot 10^{-13}\,\mathrm{s}^{-1}$. By applying these values to Eq. (1.16), we find $t_{eq} = 0.16\,\mathrm{My}$.

After Behn et al. (2009), Hall and Parmentier (2003), the final grain size is expressed as:

$$G_f = \left[\left(\frac{k}{n\lambda\dot{\epsilon}_{disl}}\right) + \left(G_0^n - \frac{k}{n\lambda\dot{\epsilon}_{disl}}\right)\exp(-n\lambda\dot{\epsilon}_{disl}t)\right]^{1/n} \tag{1.17}$$

with $k = k_0 \exp(-E_a/RT)$ from Eq. (1.1). Substituting k by the right-hand term of Eq. (1.11), we get for olivine:

$$G_f = \left[\left(\frac{8\,\alpha\gamma\Omega D_{gb}^{Si}}{n\delta\lambda\dot{\epsilon}_{disl}RT}\right) + \left(G_0^n - \frac{8\,\alpha\gamma\Omega D_{gb}^{Si}}{n\delta\lambda\dot{\epsilon}_{disl}RT}\right)\exp(-n\lambda\dot{\epsilon}_{disl}t)\right]^{1/n}. \tag{1.18}$$

Based on Eqs. (1.9), (1.16) and (1.18), we have constructed Fig. 1.8 which indicates the expected grain sizes as a function of depth considering an oceanic lithospheric geotherm of 100 My. The influence of deformation on grain sizes is represented by the full curves, where the balanced rates of NGG and DR were applied for depths ranging from 50 to 80 km (LAB). At shallower and greater depths than the LAB, solely NGG was considered. The dashed curves in Fig. 1.8 indicate deformation-free grain growths (NGG). We can thus observe that by applying a strain rate of $\dot{\epsilon}_{disl} = 1 \cdot 10^{-13}\,\mathrm{s}^{-1}$, grain sizes are reduced by only a factor 3 compared to static grain growth. This figure also shows the influence of initial grain size, ranging from 1 µm (black curves) to 10 cm (magenta curves). Comparison of the resulting olivine grain sizes for $G_i \leq 1$ mm shows that they are identical at depths ≥ 120 km, regardless of the initial grain size conditions. For $G_i > 1$ cm, grain growth is expected to be considerably slower to nonexistent (e.g. $G_i = 10$ cm). As a consequence, at depths greater than the LAB, we observe that the reduced grain sizes rapidly reach those of NGG, which indicates that once the deformation stops in the asthenosphere, the healing process is quite instantaneous.

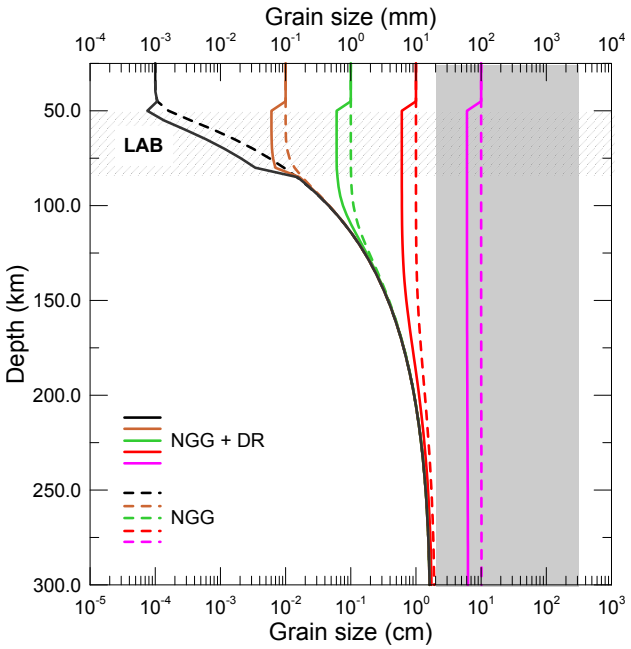

Figure 1.8 – Grain sizes as a function of depth considering an oceanic lithospheric geotherm of 100 My (Stixrude and Lithgow-Bertelloni, 2005) for a duration of $t_{eq} = 0.16$ My. Normal grain growth was considered for depths <50 and >80 km (dotted curves) whereas for the LAB, grain size was calculated following Eq. (1.18) (full curves). The different curves correspond to differences in initial grain sizes (ranging from 1 µm to 10 cm).

1.5 Conclusion

We have demonstrated here that dry olivine normal grain growth is rate-limited by diffusion of Si at grain boundaries, which reconciles the experimental discrepancies observed at atmospheric pressures. Dry grain growth therefore likely occurs with a grain size exponent of $n = 2$ for application to geological length and time scales. By using the existing 1 atm database, we have determined the effective grain boundary thickness at $\delta = 29.21^{+37}_{-16}$nm, which is considerably different from the structural grain boundary thickness (i.e. 1 nm, Hiraga and Kohlstedt, 2007). The water effect on olivine normal grain growth for H_2O-undersaturated solubility conditions was investigated with $D^{Si}_{gb,wet}$, which indicates that it has a negligible effect on grain growth rates. Finally, we have applied our model to determine the grain sizes in an olivine-rich mantle undergoing deformation in the dislocation creep regime and found that once deformation stops, the healing process in the asthenosphere is effectively instantaneous.

Chapter 2

Olivine grain growth: from laboratory experiments to a unified grain growth law

Contents

Summary

In the previous chapter, I have demonstrated that the dry and slow olivine grain growth rates are limited by diffusion of silicon at grain boundaries. In this chapter, I investigate the faster growth rate regime for liquid-bearing aggregates as highlighted in the general introduction. In order to thoroughly investigate the melt and fluid effects on olivine grain growth rates, I report new high temperature (T = 1200 to 1350 °C) and high pressure (P = 0.3 to 3.0 GPa) experiments that were performed in a piston cylinder apparatus and in an internally heated pressure vessel. The starting materials consisted of (i) natural olivine aggregates containing a wide range of melt contents (from nominally melt-free to 80 wt. % melt) or water under H_2O-saturated conditions and (ii) a genuinely dry and melt-free synthetic olivine sample. The first part of this chapter therefore presents the materials and the followed protocol for these experiments. Since grain growth is established through the measurement of the grain sizes, the material and methods section also indicates the detailed procedure used for grain size determination. In addition, this section includes the analytical protocol used for chemical analyses, for infrared spectroscopy and for Raman spectroscopy analyses.

I then indicate the results that are divided as follows: (i) microstructural results by use of a scanning electron microscope, (ii) the chemical analysis results from electron microprobe measurements, (iii) the measured melt water contents by infrared and Raman spectroscopy, (iv) the grain size distributions and finally the evolution of grain sizes of the different experimental samples as a function of time, temperature, melt contents and pressure. The main results indicate that all the samples used in this study contained melt or fluids, with an emphasize on the nominally melt-free samples and an exception for the synthetic olivine aggregate sample, which is well fitted by dry olivine grain growth determined in Chapter 1. Comparison of the resulting experimental grain sizes with the dry olivine grain growth law indicates that the growth rates are indeed faster, whether the samples contain a melt or a fluid phase. Furthermore, for high temperature experiments (i.e. T >1250 °C), we observe a significant pressure effect on grain growth.

The results are then followed by a theoretical section, where I briefly introduce Otswald ripening (i.e. grain growth in the presence of a secondary phase, whether solid or liquid), defined by two rate-limiting cases, namely diffusion-limited and interface reaction-limited (Greenwood, 1956, Lifshitz and Slyozov, 1961, Wagner, 1961). However, since the classical expression for liquid diffusion-limited grain growth during Otswald ripening does not take into account the diffusion length through the liquid (i.e. the width of melt separating each olivine grains, δ_l), liquid-bearing grain growth equations are derived following three different liquid geometries, namely liquid films surrounding the grains with (i) δ_l smaller than the grain size and (ii) δ_l bigger than the grain size, and (iii) liquid films and tubes (based on the same formalism as in Chapter 1). Through the dissolution rate constant, the interface reaction-controlled grain growth equation is also presented in this theoretical section.

The discussion section includes a comparison of the results on liquid-bearing grain growth aggregates with analogous samples from the literature, showing that this study is in agreement with previously published experiments. Application of the liquid diffusion-limited grain growth equations to the data appears to be inconclusive, thus setting aside the diffusion properties of the liquid medium as a key parameter for grain growth. Grain growth for liquid-bearing aggregates must therefore occur through interface reaction processes, which is justified by the similar growth rates for melt- and fluid-bearing aggregates. Modeling interface reaction-controlled grain growths however necessitates the knowledge of a fundamental parameter, the wetness, φ, that includes the liquid fraction of the aggregates, which was reformulated from the study of Yoshino et al. (2005). The grain sizes determined in this study were used to define a thermally-activated precipitation constant as the rate-limiting factor for liquid-bearing aggregate grain growth. The resulting law allows grain growth to be calculated under a wide range of liquid fraction, namely from 0 to 100 wt. % liquid.

La croissance de l'olivine : des expériences en laboratoire vers une loi de croissance unifiée

J'ai démontré dans le chapitre précédent que la croissance d'olivine anhydre, assez lente, est limitée par la diffusion du silicium aux joints de grains. Ce *chapitre deux* concerne les taux de croissance plus rapides, caractéristiques des agrégats d'olivine en présence de liquide silicaté ou acqueux (Fig. 2). Afin d'étudier de manière rigoureuse l'effet d'un liquide magmatique ou d'un fluide acqueux sur la croissance de grains d'olivine, je présente ici de nouvelles expériences haute température (T = 1200 à 1350 °C) et haute pression (P = 0.3 à 3.0 GPa), réalisées dans un piston cylindre ainsi que dans un autoclave à chauffage interne. Les matériaux de départ sont constitués (i) d'agrégats d'olivine naturelle contenant différentes quantités de liquide silicaté (de nominalement 0 à 80 % pds.) ou de l'eau en conditions sur-saturées et (ii) un échantillon d'olivine synthétique réellement anhydre et sans liquide silicaté. La première partie de ce chapitre se focalise sur les matériaux de départ ainsi que sur le protocole expérimental. Cette partie inclut également la procédure détaillée utilisée pour la détermination de la taille de grains pour chaque produit expérimental, étape critique quant à l'élaboration d'une loi de croissance unifiée. Cette partie contient également le protocol analytique utilisé pour les analyses chimiques, ainsi que pour les analyses réalisées à la spectroscopie infrarouge et à la spectroscopie Raman.

Les résultats sont ensuite divisés comme suit : (i) les résultats microstructuraux récoltés à l'aide d'un microscope électronique à balayage, (ii) les résultats chimiques, obtenus à l'aide d'une microsonde électronique, (iii) les quantités d'eau mesurées par spectroscopie infrarouge et Raman, (iv) les distributions de taille de grains et finalement, l'évolution de la taille de grains pour chaque produit expérimental en fonction du temps, de la température, des quantités de liquide silicaté et d'eau et de la pression. Les résultats principaux montrent que tous les échantillons contiennent une certaine quantité de liquide silicaté, en particulier les échantillons nominalement sans liquide silicaté, à l'exception de l'échantillon fabriqué synthétiquement. Ce dernier échantillon est très bien contraint par la loi de croissance sèche déterminée dans le Chapter 1. Une comparaison entre les taux de croissance des échantillons expérimentaux de ce chapitre et la loi de croissance anhydre de l'olivine indique que la croissance est en effet bien plus rapide pour les échantillons contenant des liquides silicaté ou acqueux. De plus, pour les échantillons ayant subi une très haute température (i.e. >1250 °C), nous observons un effet de pression important sur la croissance de grains.

Une partie théorique sur la croissance de grains en présence de liquide suit la partie résultats expérimentaux. La notion d'Ostwald ripening (i.e. croissance de grains en présence de phase secondaire, que cette phase soit liquide ou solide) y est introduite. Ce type de croissance est limitée soit par la diffusion, soit par des réactions aux interfaces (Greenwood, 1956, Lifshitz and Slyozov, 1961, Wagner, 1961). Cependant, je reformule les équations de croissance limitée par la diffusion afin de prendre en compte l'épaisseur du liquide séparant deux cristaux (δ_l), sur laquelle s'opère la diffusion dans le liquide. Trois types de géométrie sont alors considérés : (i) δ_l est plus petit que la taille des cristaux, (ii) δ_l est plus grand que la taille des cristaux et (iii) le liquide est sous forme de film ou de tube (suivant le même formalisme que dans le Chapter 1). L'équation de croissance limitée par les réactions aux interfaces est également présentée dans cette partie, où j'introduis le terme de constante de dissolution.

La discussion se focalise dans un premier temps sur une comparaison des résultats expérimentaux de ce chapitre avec les données de la littérature sur des échantillons de même composition. Les taux de croissance mesurés dans ce chapitre sont en accord avec ceux de la littérature. Je tente ensuite d'appliquer les équations de croissance limitées par la diffusion, mais ceci reste peu concluant. Ainsi, la croissance de grains en présence de liquide ne semble pas être limitée par la diffusion, mais plutôt par les réactions aux interfaces, qui est justifiée par les taux de croissance similaires observés dans les échantillons contenant du liquide silicaté ou de l'eau. Modéliser de telles croissances nécessite cependant un paramètre fondamental : la mouillabilité du liquide, φ. Ce paramètre tient compte de la quantité de liquide présent dans l'échantillon et a été reformulé dans ce manuscrit d'après l'étude de Yoshino et al. (2005). Les tailles de grains déterminées dans

cette étude ont été utilisées pour définir une constante de précipitation (dépendante de la température) limitant ainsi la croissance d'olivine en présence de liquide silicaté ou acqueux. La loi de croissance unifiée permet ainsi de calculer les taux de croissance pour des échantillons contenant une quantité de liquide variant entre 0 et 100 % pds..

2.1 Material and methods

2.1.1 Starting material

Grain growth experiments were performed on four types of olivine + basalt aggregates containing different melt contents: nominally 0, 1, 2 and 12 wt. % (namely 0PR, 1PR, 2PR and 12PR, respectively). To check the effect of water on olivine grain growth, a mixture of olivine + H_2O under water-saturated conditions (namely H_2O sat. experiments) was also prepared (2 wt. % H_2O in IHPV1 and PC19, and 20 wt. % H_2O in PC20). Additionally, four experiments were run with capsules consisting of 20 wt. % olivine + 80 wt. % basalt (i.e. 80PR experiments) in order to facilitate water content measurements by infrared spectroscopy (FTIR) and chemical analyses by electron microprobe (EMP) in the glass phase. Finally, one experiment was run with a solution-gelation (sol-gel) material of iron-free olivine (Fo_{100}) to assess grain growth rates of genuinely melt- and water-free olivine. Its fabrication process is described later in this section.

Natural San Carlos olivines (Arizona, USA) were handpicked, coarsely ground in an agate mortar and annealed at atmospheric pressure at the Fayalite-Magnetite-Quartz (FMQ) buffer and 1100 °C for 7 to 15 h in order to eliminate all impurities such as serpentine or liquid (melt and/or fluid) inclusions. After this annealing step, olivine crystals were ground and sieved down to initial grain sizes ranging from 5 to 15 µm. Two batches of sieved grain sizes were made (i.e. SM1 and SM2). The average initial grain sizes were measured from electron back-scattered diffraction (EBSD) maps on the initial starting powders of San Carlos olivine and indicated average grain sizes of 5.33 ± 0.20 µm (SM1) and 10.84 ± 1.06 µm (SM2). Starting composition was determined at SARM (Service d'Analyse de Roche et de Minéraux) at Nancy, France (CRPG – Centre de Recherche Pétrographiques et Géochimiques) and is indicated in Table 2.1. The melt phase was composed of natural basalt ("popping" rock, hereafter named PR, Javoy and Pineau (1991)), initially containing 6000 ppm H_2O and 500 ppm CO_2. The basalt was placed in a Pt crucible for dehydration and decarbonation in an atmospheric furnace at 600 °C overnight. It was then melted at atmospheric pressure and 1400 °C for 2 h in order to obtain a glass phase. The resulting glass was coarsely crushed, placed in an open $Au_{80}Pd_{20}$ capsule and annealed at 1250 °C, FMQ buffer for 1 h before drop-quenching the material. This resulted in a bubble-free glass, which was used as starting powder (Table 2.1).

The sol-gel method consists of a mixture of reactants, that is subsequently reaction-sintered in order to form a fine-grained polycrystalline solid. In our case, magnesium nitrate was required for a forsteritic composition ($MgSiO_4$). The correct amount of magnesium nitrate was placed in a teflon beaker containing a magnetic stirrer before being consecutively mixed with HNO_3 (ammonia) + H_2O and a mixture of ethanol + tetra-ethyl orthosilicate (TEOS) (1:1 ratio) for the silica component of forsterite. To initiate the gelation of the solution, a few drops of HNO_3 (nitric acid) + H_2O was added. The gel was then placed on a hot plate overnight for drying. In order to continue the drying process and to remove the impurities from the gel, such as NO_2 and NH_3, the gel was transferred to a silica beaker before being placed under a fume-hood in an atmospheric furnace and fired at 800 °C for >12 h. The dried gel was then ground and placed in two open Pt capsules that were annealed at 1400 °C for 13 h for complete drying. Once the annealing step was completed, one capsule was welded shut for the experimental run whereas the powder of the second capsule was retrieved and mounted in epoxy for starting grain size characterization by EBSD mapping. The starting grain size was therefore determined to be <1 µm for the sol-gel experiment.

Table 2.1 – Bulk starting compositions (wt.%).

	SiO_2	TiO_2	Al_2O_3	FeO	MnO	MgO	CaO	Na_2O	K_2O	P_2O_5	Total
San Carlos	40.31	<dl	0.10	8.50	0.13	49.50	0.13	<dl	<dl	<dl	99.64
PR	49.52	<dl	14.46	9.96	0.17	8.04	10.53	2.79	0.63	0.29	99.02

dl – detection limit.

2.1.2 Experimental conditions

Except for the sol-gel experiment, initial mixtures were placed in welded $Au_{80}Pd_{20}$ capsules (6 mm height and 2.5 mm internal diameter) to minimize iron loss from the sample to the capsule. Two experiments (IHPV1 and IHPV2, Table 2.2) were run in internally heated pressure vessels for relatively low pressure conditions (0.3 GPa), which were ended by drop-quench. For higher pressure conditions ($\geq$0.5 GPa), the capsules were cold-pressed at 500 bar (Ar gas) before being positioned in $^3/_4$-inch piston cylinder assemblages (experiments PC2 to PC26, Table 2.2) consisting of talc/Pyrex/graphite/alumina jackets (Fig. 2.1). Solely experiments PC25 and PC27 (Table 2.2) were run in $^1/_2$-inch piston cylinder anvil. For an easy removal from the piston cylinder anvil after the experiment, teflon plaster was placed around the assemblage.

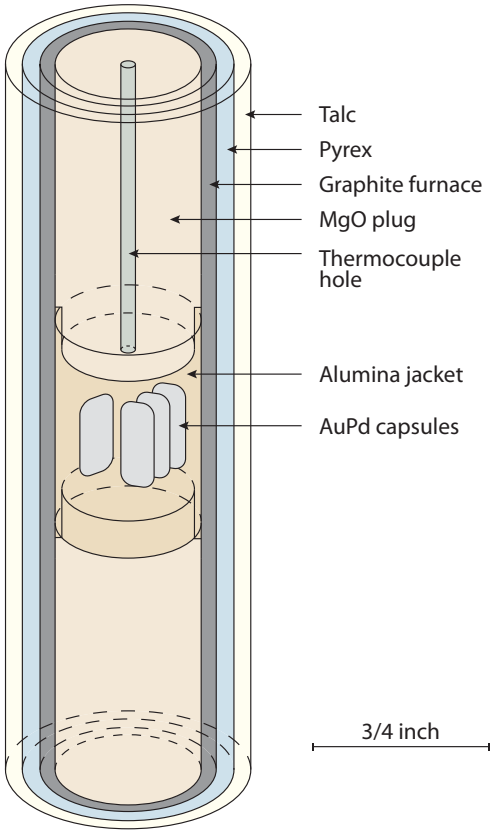

Figure 2.1 – Piston cylinder assemblage consisting of talc/Pyrex/graphite/alumina jacket. Here, the assemblage is represented for the experiments containing four capsules with four different melt contents.

MgO plugs were adjusted at the top and the bottom of the assemblage in order to place the capsules within the graphite furnace, where the thermal gradient is at its lowest. For the majority of the experiments run in this study, the empty space between the capsules was filled with AlSiMag powder, which did not interact with the capsules during the experiments. These experiments are referred hereafter as AlSiMag experiments. The oxygen fugacity (f_{O_2}) of the latter experiments was not controlled but the presence of graphite (i.e. the furnace) would imply an f_{O_2} close to the FMQ buffer. Under these conditions, it is known that diffusion of water from the high-pressure solid media through the noble metal capsule could take place (although in our experiments, we used $Au_{80}Pd_{20}$ capsules thus minimizing this effect; Truckenbrodt and Johannes (1999)). To verify whether our grain growth rates were affected by the assemblage, a series of piston cylinder experiments was conducted with hematite powder as pressure medium

(hereafter referred as hematite experiments), limiting the degree of sample hydration by hydrogen (H_2) incorporation within the capsule. Only the sol-gel experiment was run with MgO powder as pressure medium. For the IHPV series, the use of pure Ar gas as pressure medium without addition of hydrogen allowed oxidized conditions to be reached, namely $f_{O_2} >$ FMQ + 1 (Gaillard et al., 2003, Iacono-Marziano et al., 2012).

Since grain growth is time-dependent, experiments at 1250 °C and 0.5 GPa were run for 1, 12, 72 and 360 h. For these runs, four capsules containing different melt contents (i.e. nominally melt-free, 1 wt. % melt, 2 wt. % melt and 12 wt. % melt-bearing olivine aggregates) were inserted within the assembly. Since no major melt effect on grain growth was observed for these experiments, as indicated in Section 2.2, all the other experiments were run with nominally melt-free and 1 wt. % melt-bearing olivine capsules. To account for the temperature dependence on grain growth and to determine whether pressure effectively has an effect, we performed experiments at (i) 1200 °C and pressures of 0.3 and 0.5 GPa, (ii) 1250 °C and pressures of 0.5 and 1.5 GPa and (ii) 1350 °C and pressures of 1.5 and 3.0 GPa. AlSiMag experiments at T = 1250 °C and P = 0.5–1.5 GPa were reproduced with hematite experiments. The sol-gel experiment was conducted at 1350 °C and 1 GPa for 2 h. Water-saturated conditions were examined with experiments performed within IHPV and piston cylinder runs with hematite powder as pressure medium. Finally, for FTIR and EMP analyses, experiments PC4, PC5, PC13 and PC18 were duplicated with 80PR mixtures. The experimental runs are summarized in Table 2.2.

Table 2.2 – Experimental conditions – All experiments were run with San Carlos olivine without added melt (0PR) or with added melt (1 wt. % = 1PR; 2 wt. % = 2PR; 12 wt. % = 12PR) except for run PC25, which contained sol-gel (Fo_{100}).

Run No.	Temperature (°C)	Pressure (GPa)	Time (h)	Capsule type	Inner pressure medium
IHPV2	1200	0.3	1	0PR 1PR H_2O sat.	Ar gas
IHPV1	1200	0.3	12	0PR 1PR H_2O sat.	Ar gas
PC12	1200	0.5	1	0PR 1PR	AlSiMag
PC8	1200	0.5	12	0PR 1PR 2PR 12PR	AlSiMag
PC2	1250	0.5	1	0PR 1PR 2PR 12PR	AlSiMag
PC4	1250	0.5	12	0PR 1PR 2PR 12PR	AlSiMag
PC23	1250	0.5	12	80PR	AlSiMag
PC5	1250	0.5	72	0PR 1PR 2PR 12PR	AlSiMag
PC21	1250	0.5	72	80PR	AlSiMag

Experimental conditions (continued).

Run No.	Temperature (°C)	Pressure (GPa)	Time (h)	Capsule type	Pressure medium
PC6	1250	0.5	360	0PR 1PR 2PR 12PR	AlSiMag
PC15	1250	0.5	1	0PR 1PR	Hematite
PC14	1250	0.5	12	0PR 1PR	Hematite
PC20	1250	0.5	75	0PR 1PR H_2O sat. 80PR	Hematite
PC16	1250	1.5	1	0PR 1PR	AlSiMag
PC13	1250	1.5	12	0PR 1PR	AlSiMag
PC22	1250	1.5	12	80PR	AlSiMag
PC19	1250	1.5	12	0PR 1PR H_2O sat. 80PR	Hematite
PC25	1350	1.0	2	Fo_{100}	MgO
PC17	1350	1.5	1	0PR 1PR	AlSiMag
PC18	1350	1.5	12	0PR 1PR	AlSiMag
PC26	1350	1.5	12	80PR	AlSiMag
PC27	1350	3.0	12	1PR	AlSiMag

2.1.3 Grain size determination

After the experiments, samples were retrieved from the capsules and mounted in epoxy for grain size determination. The mounts were mechanically polished using diamond pastes of various grain sizes down to 0.25 µm and finally chemically-mechanically polished using water-based colloidal silica suspension (particle size of 0.04 µm). EBSD analysis was performed to map the crystallographic preferred orientation of the starting materials and of the experimental run products. EBSD measurements were carried out on samples 0PR–, 02PR-PC2; 1PR-PC4; 0PR–, 1PR-PC5; 0PR–, 12PR-PC6 using an EDAX DigiView EBSD Camera in a scanning electron microscope equipped with a field emission gun (SEM-FEG) installed at Institut des Sciences de la Terre d'Orléans (ISTO, France), at 20 kV acceleration voltage and a beam intensity of 18 nA. Automatic EBSD mapping of the zones of interests was performed at step sizes $\leq$1.0 µm and a working distance of 18 mm. Run products from experiments IHPV1, IHPV2, PC19, PC20, PC25 as well as the starting material batch SM2 and the starting sol-gel powder were mapped using a SEM-FEG at the Institut de Chimie Moléculaire et des Matériaux d'Orsay (ICMMO, France)

at 30 kV acceleration voltage and a beam intensity of 1–2 nA. Automatic EBSD mapping of the samples was executed at step sizes $\leq$1.0 µm and a working distance of 13 mm. The rest of the experimental run products and SM1 were mapped by using an EDAX-TLS Digiview 3 in a FEI Quanta 3D FEG installed at GFZ-Potsdam, at 20 kV acceleration voltage and a beam current of 8 nA. For these analyses, automatic EBSD mapping was achieved at step sizes $\leq$1.6 µm and a working distance of $\leq$15 mm. In these machines, reliable diffraction patterns were produced by inclining the samples at 70° to the electron beam current and by using the SEM low-vacuum mode with 5 and 15 Pa pressure of N gas at ISTO and ICMMO, respectively, and 5 Pa of water vapor at GFZ-Potsdam to minimize charging at the surface of the samples. Automated identification of the patterns was made possible using Orientation Imaging Microscopy (OIM™) Data Collection and Data Analysis softwares.

Before the segmentation step, Data Analysis software was used to retrieve two types of maps: (i) Unique Grain (UG) maps (Fig. 2.2) and (ii) Image Quality (IQ) maps (e.g. Fig. B.1). The latter maps indicate whether the diffraction pattern identified by the EBSD detector is of good quality (i.e. perfection of the crystal lattice in the diffracting volume). On these kind of maps, if a diffraction pattern of good quality is detected, the pixel is white; whereas, on the contrary, the pixel is dark; these maps therefore display ranges of gray values. Melt pockets distributed throughout the melt-bearing samples and grain boundaries were therefore clearly visible on IQ maps (indicated by dark/black pixels). For the UG maps, a clean up procedure was applied to the raw data thanks to the software. A first step consisted of cleaning the data by applying the Neighbor Confidence Index clean up with a minimum confidence index of 0.12. This step led to an increase of the grain areas on the UG maps compared to the raw data. Secondly, a correction of the well-known pseudosymmetry of olivine of 60° around the [100] axis was applied to the raw data (Bystricky et al., 2006). No further clean up procedure was applied after these two steps. For the majority of the samples (i.e. number of grains >100 in Table 2.6), segmentation of the maps was performed by using Image-SXM, which detected grain boundaries from the UG maps. Since melt is present at grain boundaries and at triple junctions and because the clean up procedure increased the grain areas, the grain boundary images acquired with Image-SXM were superimposed upon the IQ maps. By using the look-up tables (LUTs) in Image-SXM, which directly operate on the gray values, triple junctions and accurate grain boundaries were recovered on the resulting images. On some images, however, certain grain boundaries needed manual segmentation. This procedure was systematically applied until the resulting images were considered to be the accurate microstructure of the sample. Images were then converted into bitmaps, where individual grains were identified as black pixels separated by white pixels representing the grain boundaries and triple junctions (Fig. 2.3). Particle analysis was then executed in Image-SXM in order to obtain the area (S) of each grain. The grain size for each grain was calculated through the conventional $2\sqrt{S/\pi}$ assuming that each grain is equiaxed and can be represented by a perfect sphere. To account for the cut-section effect, a correction factor of $4/\pi$ was applied to all calculated grain sizes (Royet, 1991, Underwood, 1972, see also Appendix B). An average 2D value, $\bar{G}$, was consequently obtained for each experimental run. For a conversion from the 2D average value to a 3D grain size, the reader is invited to apply a factor of $4/\pi$ to the grain sizes indicated in Table 2.6 (Seyhan et al., 1996, Underwood, 1970).

We compared the mean grain sizes obtained between measurements of 100 and of more than 300 grains in samples 2PR-PC2, 0PR-PC12, 1PR-PC13 and 1PR-PC15 to test if the number of grains affected the calculated average areas and we found that it did not. Therefore, another (faster) method was applied to the rest of the IQ maps (i.e. number of grains = 100 in Table 2.6), which consisted of randomly drawing segments over the IQ maps and manually outlining the grain boundaries of the intersected grains by using ImageJ (Fig. 2.4). We also used this method to determine the grain sizes from two samples of the 80PR series based on microphotographs of the doubly polished chips prepared for FTIR measurements. Since the number of crystals was limited in this series, only 40 and 14 grains were measured in samples 80PR-PC20 and 80PR-PC23, respectively. We have therefore decided to adjust the uncertainties of these samples by adding 20% error to the standard deviation of the measurements.

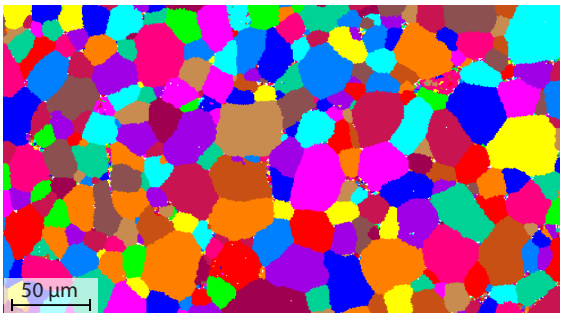

Figure 2.2 – Example of a UG map (sample 2PR-PC5).

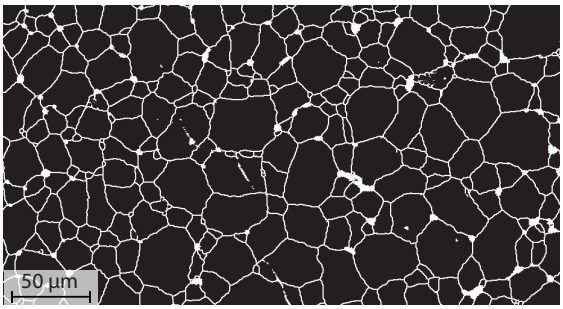

Figure 2.3 – Example of a segmented image after the procedure explained in the text by using Image-SXM (sample 2PR-PC5). White pixels contained in some grains were manually separated from the grain boundaries. Image-SXM does not take into account these white pixels when calculating the area.

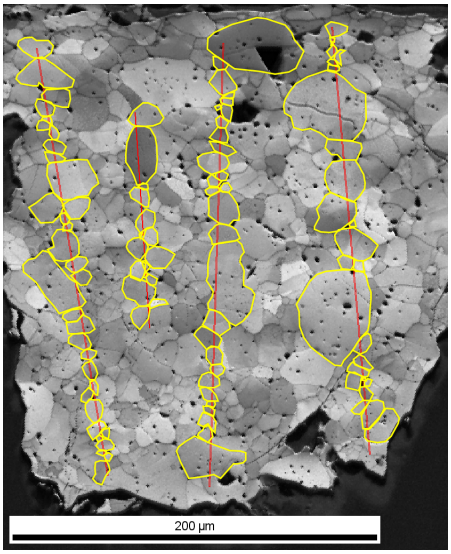

Figure 2.4 – Example of grain boundary outlines after the procedure explained in the text by using ImageJ (IQ map of sample 1PR-PC14).

We also want to highlight that we tested the commonly used linear intercept method, which consists of drawing lines of known lengths across an optical or SEM image and dividing the lengths by the number of intersected grains (for more details, see Appendix B). Usually, the deduced apparent grain size is multiplied by a factor ≥1.5 (Karato, 1989, Nichols and Mackwell, 1991). We therefore tried to obtain an intercept/area (Image-SXM) calibration with samples 2PR-PC2, 0PR-PC12, 1PR-PC13 and 1PR-PC15, but neither the number of intercepted grains nor the way we measured the intercept length (parallel, perpendicular or even at random distance from the intercept segment) rendered any satisfactory calibration.

2.1.4 Chemical analyses

Chemical compositions of the olivine and melt phases within the post-mortem samples were obtained by using an SXFive electron microprobe at ISTO. EMP analyses were conducted at 15 kV, 6 nA and 2 nA for olivine and melt phases, respectively, and 10 s counting on peak elements. The melt phase was systematically analyzed in defocused mode (2 µm beam diameter). Melt composition is assumed to remain constant at a given T/P/time condition independently of melt content. Therefore, mass balance calculations were performed by using the melt composition of samples 12PR when samples containing lower melt contents were difficult to analyze.

2.1.5 Melt water contents

Water concentrations of the quenched melt phases were determined by transmission FTIR spectroscopy on doubly polished chips (thicknesses ranging from ∼30 to 120 µm) using a Nicolet Continuµum (Thermo Scientific) spectrometer equipped with an IR microscope, a CaF_2 beam-splitter and a liquid nitrogen cooled Mercury Cadmium Telluride (MCT) wide range detector (250 µm). The microscope runs in confocal mode, using a 15× infinity corrected Scwharzschild objective and a matching 15× condenser. IR spectra were acquired in the range 1000–5000 cm^{-1} with 256 scans and a resolution of 4 cm^{-1}. The diameter of the analyzed spot was 50 µm. The peak heights were determined using linear background corrections (e.g. Lesne et al., 2011). The total water was calculated from the absorbance of the fundamental OH-stretching vibration at about 3530 cm^{-1} and using the linear extinction coefficient in Stolper (1982).

For samples containing 12 wt. % melt, no melt pockets were large enough to solely analyze the water content of the melt phase as shown in Fig. 2.5(a). Therefore, a correction of the measured water contents was applied by taking into account the olivine crystals crossed by the FTIR beam. The melt pockets were estimated to 6% of the total analyzed zone. The error on the calculated melt water contents takes into account the standard deviation but also the previously mentioned estimation. Unlike the 12 wt. % melt series, the 80 wt. % melt samples were easier to analyze since few olivine crystals were present in the glass phase (Fig. 2.5(b)). Melt water contents were measured where the sample presented a homogeneous thickness for FTIR analyses. For both type of samples, the thickness was double-checked after analyses by using the microscope gear for every single measurement.

2.1.6 Raman spectroscopy

As will be presented in Section 2.2, sample 0PR-PC6 showed anomalous features such as melt at triple junctions and grain boundaries although the starting material was dry and melt-free. To better understand the unexpected partial melting in this sample, micro-Raman spectroscopy was used to evaluate the volatile contents of the melt phase, such as H_2O or CO_2. The Raman system used for these measurements is a Jobin-Yvon Labram spectrometer (focal distance = 300 mm) equipped with a 2400 grooves/mm grating and a CCD detector. The light source is an Ar laser Innova 300-5W from Coherent©, which operates at 514.5 nm. The output laser power was set at 50 mW. Analyses on the glass phase were performed in confocal mode (hole = 500 µm, slit = 200 µm) with a 40× Leitz objective. Raman spectra were acquired between 200 and 4000 cm^{-1}. Characterization of CO_2−CO scattering and the OH stretching band was

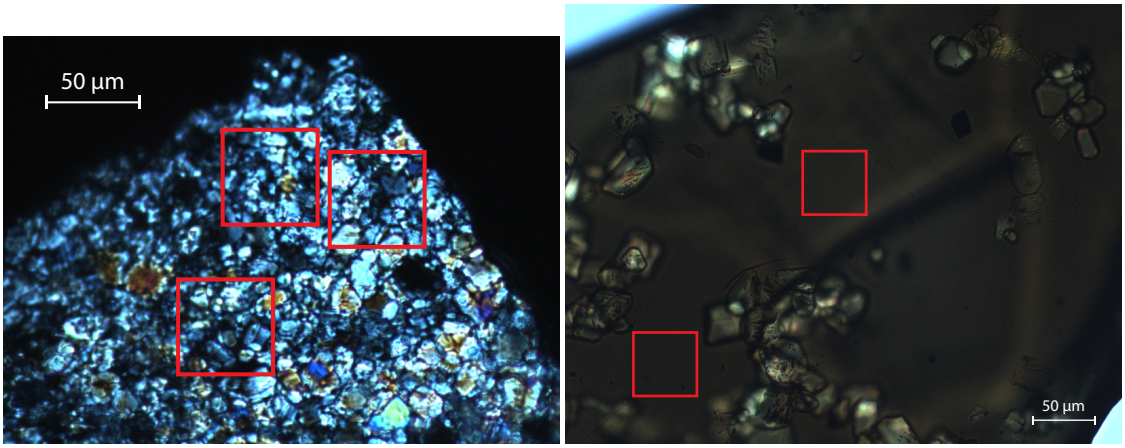

(a) Crossed polarized light microphotograph of sample 12PR-PC2

(b) Plane polarized light microphotograph of sample 80PR-PC20

Figure 2.5 – Optical microscopy photographs of samples analyzed by FTIR spectroscopy. Red squares indicate analyzed zones where the majority of the beam crossed olivine crystals for samples containing 12 wt.% in (a), whereas in the case of higher melt contents (i.e. 80 wt.% melt, (b)), special care was taken so that the beam would only cross the glass phase where the thickness was homogeneous.

done in the 200 and 1200 cm^{-1} and 2700 and 3800 cm^{-1} ranges, respectively. The spectral frequency position was monitored with the emission lines of Ne- and Hg-lamps and metal-Si chip. The accuracy of the results is within $\pm 1\,cm^{-1}$. To obtain a relatively good signal to noise ratio, the acquisition time was within 45 to 90 s.

2.2 Results

2.2.1 Microstructure

2.2.1.1 Nominally melt-free and melt-bearing samples ($\leq$12 wt. % melt series)

Typical SEM images of 1 h-long experiments are shown in Fig. 2.6. For such short annealing periods, nominally melt-free samples (Fig. 2.6(a)) show notable porosity (6.1 vol.%) but as melt content increases, the porosity decreases significantly down to 0 vol.% for high melt contents (12 wt. % melt samples). We would like to highlight that such high porosities can also be due to grain plucking during the polishing step.

Longer duration runs show considerable decrease of porosity for nominally melt-free samples (1.8 vol. %) and decreases down to 0 vol. % for samples containing $\geq$1 wt. % melt. Grains are euhedral and no variation in aspect ratio was noticed during grain growth. For 12 h-long runs at various pressures (i.e. 0.3 and 1.5 GPa), SEM imaging has showed that the nominally melt-free samples contained very small amounts of melt ($\ll$1 wt. %, Figs. 2.7 and 2.8). Therefore, regardless of the temperature or pressure conditions undergone by the experimental sample, nominally melt-free samples are hereafter regarded as samples bearing between >0 to $\ll$1 wt. % melt. The melt is inhomogeneously distributed throughout the samples for melt contents $\leq$2 wt. % and mainly resides in triple or quadruple junctions for melt contents >2 wt. % (Fig. 2.9).

One sample showed anomalous features, namely 0PR-PC6, which initially did not contain any melt. After a 15 days-long run, this sample showed melt present at grain boundaries and triple junctions as highlighted in Fig. 2.10. The timing of the beginning of partial melting in this sample is delicate because of its long experimental duration, but we can however estimate that partial melting was initiated between 72 and 360 h since no anomalous features was detected in melt-free and melt-bearing samples run for durations $\leq$72 h.

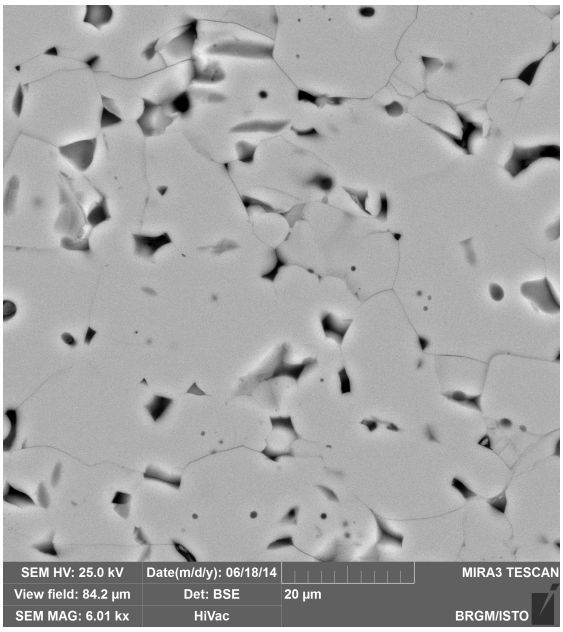

(a) Sample 0PR-PC2 containing 0 wt. % melt

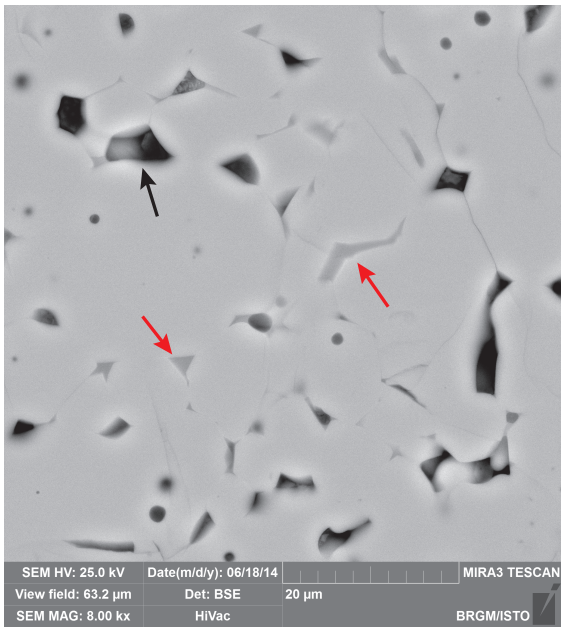

(b) Sample 1PR-PC2 containing 1 wt. % melt

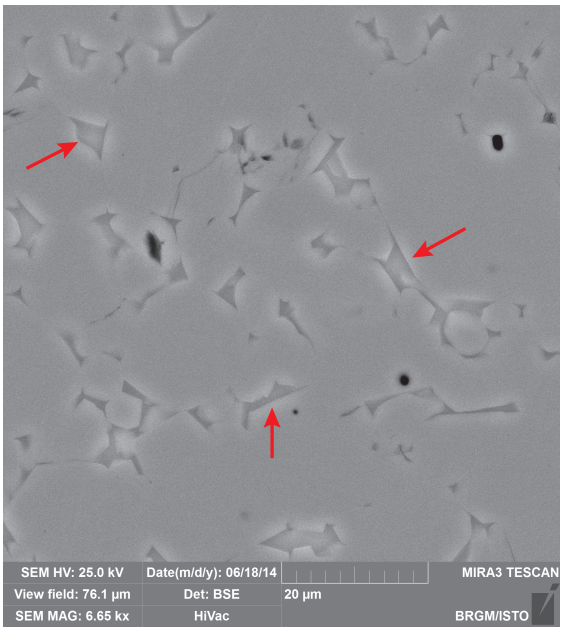

(c) Sample 12PR-PC2 containing 12 wt. % melt

Figure 2.6 – Scanning electron microscope images of run PC2 annealed at 1250 °C, 0.5 GPa and 1 h. Dark gray areas represent melt pockets located at triple or quadruple junctions (indicated by red arrows) whereas black areas are porosity of the samples or holes resulting by grain plucking due to polishing (e.g. black arrow in (b)). Scale bar is 20 µm for all images.

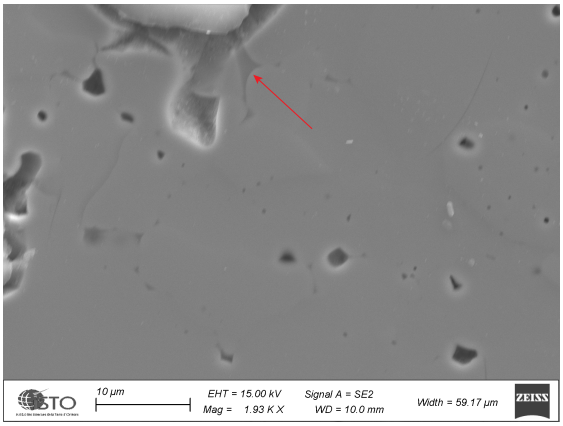

(a) Sample 0PR-IHPV1 (1200 °C and 0.3 GPa) containing ∼0 wt. % melt. Scale bar is 10 µm.

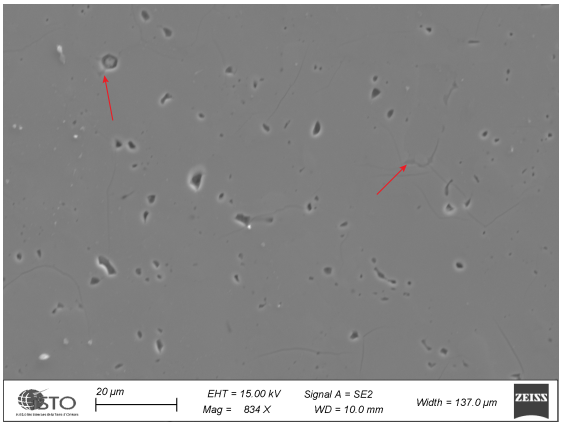

(b) Sample 0PR-IHPV1 (1200 °C and 0.3 GPa) containing ∼0 wt. % melt. Scale bar is 20 µm.

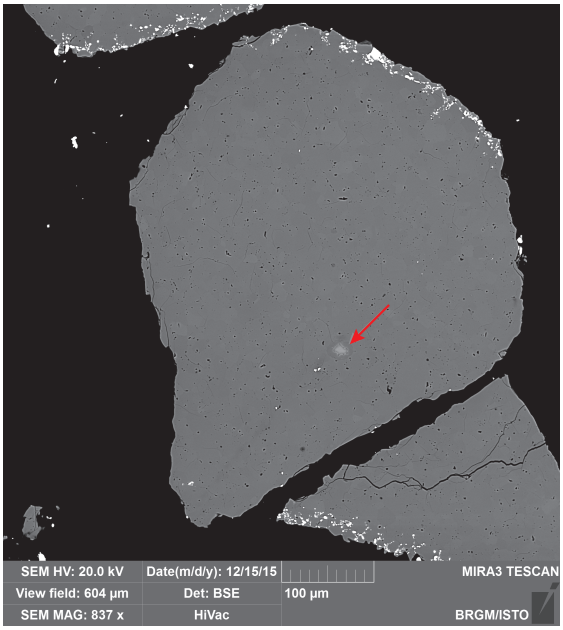

(c) Sample 0PR-PC19 (1250 °C and 1.5 GPa) containing ∼0 wt. % melt. Scale bar is 100 µm.

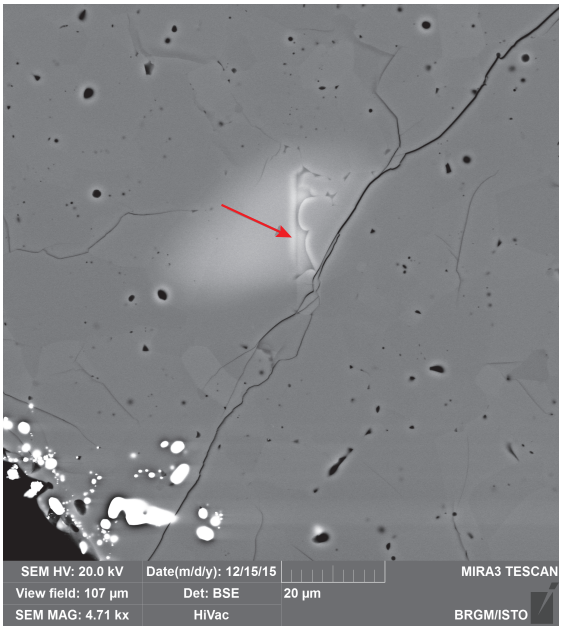

(d) Sample 0PR-PC19 (1250 °C and 1.5 GPa) containing ∼0 wt. % melt. Scale bar is 20 µm.

Figure 2.7 – SEM images of nominally melt-free samples. Red arrows indicate melt mainly located at triple or quadruple junctions. Melt content is estimated ≪1 wt. %.

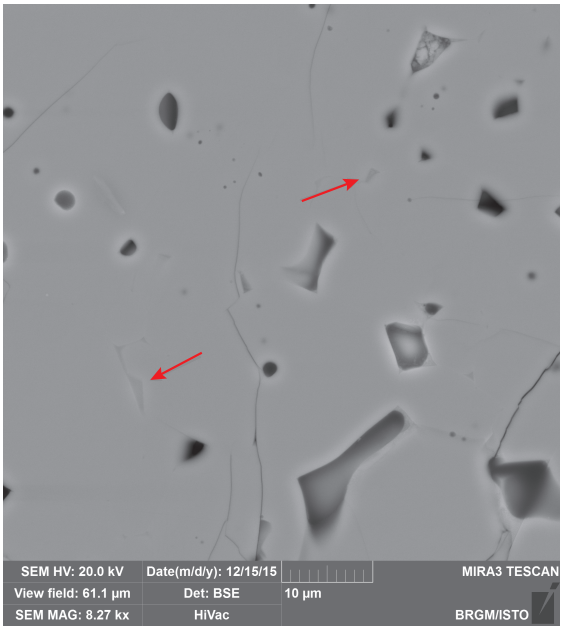

(e) Sample 0PR-PC18 (1350 °C and 1.5 GPa) containing ∼0 wt. % melt. Scale bar is 10 µm.

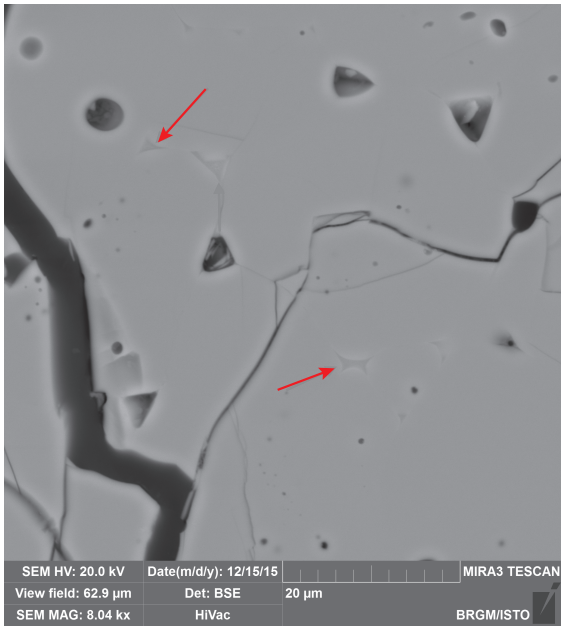

(f) Sample 0PR-PC19 (1350 °C and 1.5 GPa) containing ∼0 wt. % melt. Scale bar is 20 µm.

Figure 2.8 – (Cont.).

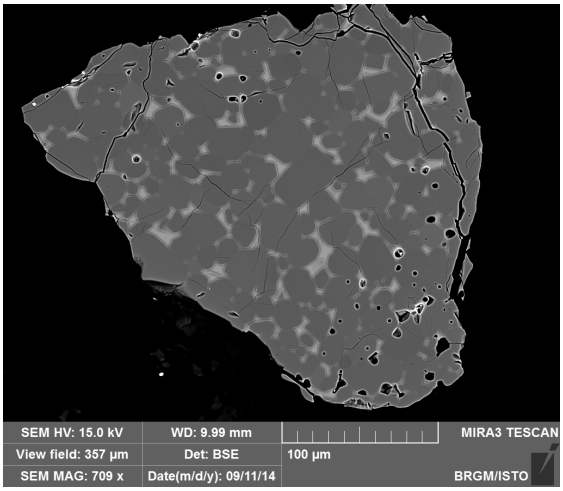

(a) Sample 12PR-PC4 containing 12 wt. % melt. Scale bar is 100 µm.

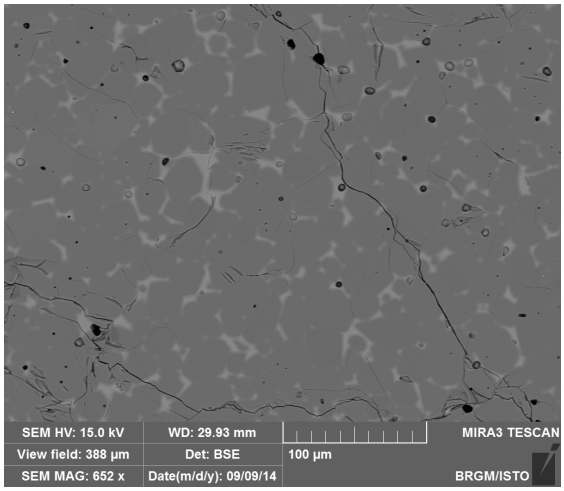

(b) Sample 12PR-PC5 containing 12 wt. % melt. Scale bar is 100 µm.

Figure 2.9 – SEM images of 12 wt. % melt samples annealed at 1250 °C, 0.5 GPa and >12 h. Light gray areas represent melt at triple and quadruple junctions..

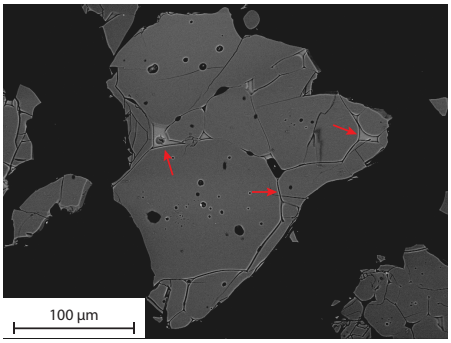

Figure 2.10 – SEM image of sample 0PR-PC6 showing melt present at grain boundaries and triple junctions (red arrows).

2.2.1.2 Water-saturated samples (H_2O-saturated series)

Water-saturated samples at 0.3 and 1.5 GPa showed the formation of secondary phases (Fig. 2.11), i.e. spinel and orthopyroxene crystals (Fig. 2.11(b)). We determined the porosity to be high (10.1 vol.%) in the low pressure sample (0.3 GPa), which indicates the presence of a fluid phase. Samples from higher pressure runs (1.5 GPa) presented a porosity of 1.3 vol. %.

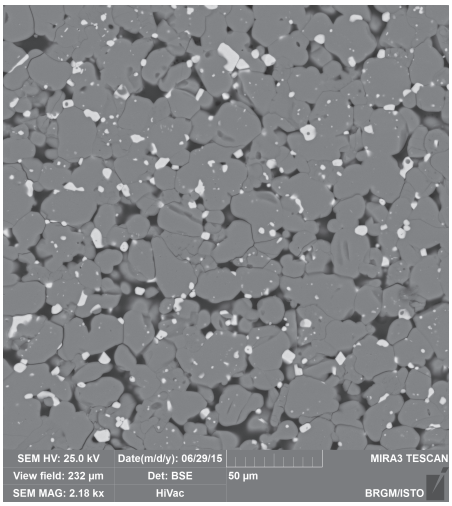

(a) Sample H_2O-sat.-IHPV1 run at 1200 °C, 0.3 GPa

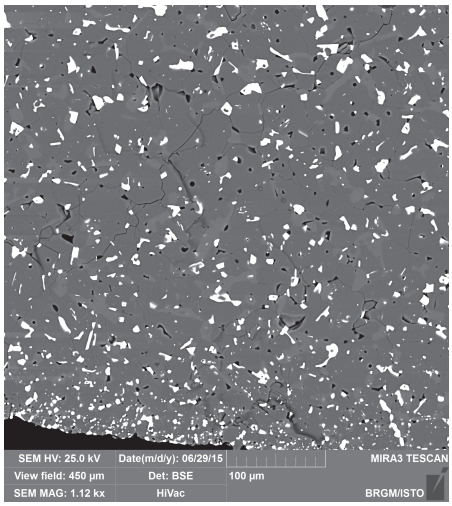

(b) Sample H_2O-sat.-PC19 run at 1250 °C, 1.5 GPa with hematite as pressure medium

Figure 2.11 – SEM images of water-saturated samples run for 12 h. Both samples indicate formation of a secondary phase (white crystals), potentially spinel crystals as indicated by EMP analyses. Orthopyroxene crystals (light gray crystals on SEM image) crystallized at 1.5 GPa.

2.2.1.3 High melt content samples (80 wt. % melt series)

Fig. 2.5(b) typically shows the microstructure of 80 wt. % melt samples, where a few crystals reside in melt pools, therefore facilitating FTIR and EMP analyses. However, two samples, namely 80PR-PC19 (hematite experiment at 1250 °C and 1.5 GPa) and 80PR-PC22 (AlSiMag experiment at 1250 °C and 1.5 GPa), were fully crystallized once retrieved from the capsules and were therefore not used for melt water content determinations. Sample 80PR-PC19 also exhibited clinopyroxene crystals (up to 47.1 wt. % from mass balance calculations) therefore reducing the proportions of olivine and melt phases.

2.2.1.4 Iron-free olivine (sol-gel serie)

The iron-free sol-gel olivine showed no porosity and euhedral grains. No elongation of the grains was noticed. Furthermore, SEM imaging did not indicate the presence of a melt phase.

2.2.2 Melt/solid chemical equilibrium

Mass balance calculations based on chemical compositions obtained from EMP analyses reveal no significant melt content variation during the experiments (Table 2.3). This indicates that the melt is in chemical equilibrium with the San Carlos olivine, even for short experimental durations (1 h experiments). Except for the 15 day-long experiment (PC6), all melt compositions display no significant deviation in total composition compared to the initial basalt (Table 2.4), which does not clearly indicate any H_2O-gain by diffusion from the piston cylinder assembly within the capsule for experimental durations $\leq$72 h.

Two samples from experiment PC6 (i.e. 0 and 12 wt. % melt, namely 0PR-PC6 and 12PR-PC6, respectively, Table 2.4) were analyzed by EMP and showed anomalous chemical compositions. The unexpected melt phase from sample 0PR-PC6 indicates a total close to 81 wt. %, which might result from the low amperage (2 nA) during the EMP analyses. The melt volatile content of this sample will be presented in Section 2.2.3. Mass balance calculations reveal that a maximum of 2.09% melt was produced. On the other hand, sample 12PR-PC6 presents a melt and olivine compositions that are strongly Fe-depleted. We also note a considerable deviation in total melt composition with the initial basalt (Table 2.4). These two observations suggest hydration of the melt phase presumably according to the following reaction:

$$H_2{}^{PC} + FeO^{melt} = H_2O^{melt} + Fe^{capsule} \tag{2.1}$$

where PC corresponds to the piston cylinder assemblage (specifically the talc cylinder), FeO^{melt} corresponds to the Fe content of the melt phase, H_2O^{melt} is the water dissolved in the melt phase and $Fe^{capsule}$ is the Fe entrapped in the capsule. We therefore performed a mass balance calculation to determine the water content in the melt phase if all the FeO is reduced to Fe and found that the melt would contain 4.26 wt. % H_2O. This result is in agreement with the total weight deficit from EMP analyses, which implies a volatile content of 5.03 ± 1.59 wt. %.

Table 2.3 – Melt contents of experiments run at 1250 °C, 0.5 GPa based on mass balance calculations.

Sample	Duration (h)	Initial melt content	Final melt content
1PR-PC2	1	0.99	0.95 ± 0.03
1PR-PC4	12	0.99	0.91 ± 0.02
1PR-PC5	72	0.99	0.95 ± 0.02
2PR-PC2	1	2.29	2.20 ± 0.06
2PR-PC4	12	2.29	2.12 ± 0.05
2PR-PC5	72	2.29	2.19 ± 0.04
12PR-PC2	1	11.76	11.28 ± 0.32
12PR-PC4	12	11.76	10.87 ± 0.23
12PR-PC5	72	11.76	11.27 ± 0.22
12PR-PC6	360	11.76	23.02
0PR-PC6	360	0.00	2.09

Table 2.4 – Post-experimental compositions from EMP analyses (in wt. %). The initial basalt and olivine compositions are also added to this table. Olivine composition remained constant for all T/P/time conditions, thus only 12PR-PC4 is reported in this table. Experiments 0PR-PC6, 12PR-PC6 and H_2O-sat. show different olivine compositions. Crystal compositions are normalized to 100 wt. %.

Sample	No. meas.	SiO_2	TiO_2	Al_2O_3	FeO	MnO	MgO	CaO	Na_2O	K_2O	P_2O_5	Cr_2O_3	NiO	Total
Melt compositions														
Initial basalt	20	51.39 (0.59)	1.79 (0.11)	14.44 (0.30)	9.55 (0.67)	0.15 (0.07)	8.23 (0.09)	10.65 (0.20)	2.82 (0.09)	0.63 (0.05)	0.26 (0.09)	0.04 (0.06)	0.05 (0.07)	97.81 (0.88)
80PR-PC20	22	50.28 (0.37)	1.70 (0.12)	13.31 (0.26)	9.68 (0.41)	0.19 (0.07)	9.96 (0.33)	9.48 (0.15)	2.95 (0.07)	0.56 (0.05)	0.16 (0.08)	0.03 (0.02)	0.04 (0.07)	98.32 (0.65)
80PR-PC19	11	51.83 (0.96)	3.11 (0.30)	20.27 (0.67)	8.86 (0.74)	0.08 (0.74)	2.75 (0.81)	4.51 (0.87)	3.59 (0.81)	1.73 (0.26)	0.41 (0.09)	0.02 (0.03)	0.04 (0.07)	97.21 (0.94)
12PR-PC8	10	55.35 (0.65)	1.71 (0.09)	13.51 (0.45)	5.82 (0.46)	0.51 (0.19)	5.70 (1.40)	11.23 (0.74)	2.26 (0.09)	0.58 (0.06)	0.16 (0.12)	0.04 (0.02)	0.02 (0.04)	96.90 (0.60)
12PR-PC2	10	53.04 (0.45)	1.62 (0.11)	13.33 (0.23)	7.19 (0.51)	0.21 (0.03)	7.35 (1.06)	10.29 (0.46)	2.37 (0.32)	0.61 (0.10)	0.27 (0.14)	0.02 (0.04)	0.06 (0.05)	96.35 (0.72)
12PR-PC4	5	53.86 (0.40)	1.78 (0.08)	13.80 (0.21)	7.38 (0.39)	0.39 (0.11)	4.67 (0.51)	11.17 (0.22)	2.27 (0.12)	0.60 (0.05)	0.22 (0.09)	0.03 (0.03)	0.05 (0.06)	96.22 (0.56)
12PR-PC5	8	53.32 (0.31)	1.79 (0.09)	14.40 (0.28)	6.84 (0.39)	0.40 (0.09)	6.15 (0.67)	11.22 (0.22)	2.59 (0.16)	0.60 (0.05)	0.24 (0.12)	0.03 (0.02)	0.04 (0.05)	97.63 (0.59)
12PR-PC6	15	50.86 (0.83)	1.34 (0.12)	12.98 (0.38)	0.16 (0.08)	0.05 (0.08)	15.37 (0.96)	8.96 (0.47)	2.14 (0.16)	0.53 (0.06)	0.32 (0.07)	0.02 (0.02)	0.04 (0.05)	92.78 (0.71)

Post-experimental compositions from EMP analyses (in wt. %) (continued).

Sample	No. meas.	SiO_2	TiO_2	Al_2O_3	FeO	MnO	MgO	CaO	Na_2O	K_2O	P_2O_5	Cr_2O_3	NiO	Total
0PR-PC6	11	40.47 (0.46)	0.25 (0.06)	6.86 (0.37)	5.56 (0.14)	1.02 (0.16)	18.76 (0.82)	6.30 (0.14)	0.57 (0.17)	0.36 (0.16)	0.69 (0.38)	0.04 (0.03)	0.22 (0.37)	81.09 (0.62)
Olivine compositions														
San Carlos		41.83	0.03	0.03	6.14	0.14	51.28	0.22	0.02	0.02	0.01	0.02	0.27	100.00
H_2Osat-IHPV1	10	42.19 (0.31)	0.01 (0.02)	0.02 (0.02)	3.85 (0.21)	0.10 (0.10)	53.33 (0.23)	0.05 (0.02)	0.01 (0.01)	0.01 (0.02)	0.01 (0.01)	0.03 (0.03)	0.38 (0.18)	101.16 (0.69)
12PR-PC4	5	41.20 (0.40)	0.02 (0.02)	0.06 (0.03)	7.57 (0.42)	0.32 (0.14)	50.35 (0.41)	0.19 (0.03)	0.00 (0.00)	0.02 (0.02)	0.02 (0.04)	0.01 (0.01)	0.26 (0.12)	100.81 (0.36)
80PR-PC20	8	41.83 (0.25)	0.03 (0.06)	0.03 (0.03)	6.14 (0.39)	0.14 (0.09)	51.28 (0.27)	0.22 (0.03)	0.02 (0.02)	0.02 (0.02)	0.01 (0.02)	0.02 (0.02)	0.27 (0.14)	101.05 (0.64)
H_2Osat-PC20	13	41.47 (0.72)	0.02 (0.04)	0.04 (0.02)	8.67 (0.35)	0.13 (0.11)	49.17 (0.63)	0.07 (0.03)	0.02 (0.02)	0.01 (0.01)	0.02 (0.03)	0.02 (0.02)	0.36 (0.15)	101.22 (0.64)
H_2Osat-PC19	14	42.79 (0.70)	0.02 (0.03)	0.02 (0.01)	1.79 (0.12)	0.08 (0.07)	54.88 (0.37)	0.02 (0.02)	0.02 (0.01)	0.01 (0.01)	0.01 (0.02)	0.01 (0.01)	0.35 (0.14)	101.48 (0.55)
12PR-PC6	12	42.87 (0.49)	0.02 (0.03)	0.05 (0.04)	0.19 (0.08)	0.03 (0.06)	56.63 (0.59)	0.13 (0.02)	0.01 (0.01)	0.01 (0.02)	0.03 (0.04)	0.00 (0.01)	0.02 (0.04)	100.89 (0.44)
0PR-PC6	7	41.70 (0.24)	0.02 (0.03)	0.04 (0.05)	4.45 (0.28)	0.35 (0.12)	53.17 (0.18)	0.05 (0.03)	0.01 (0.01)	0.03 (0.03)	0.03 (0.03)	0.13 (0.14)	0.02 (0.03)	100.93 (0.47)

Post-experimental compositions from EMP analyses (in wt. %) (continued).

Sample	No. meas.	SiO_2	TiO_2	Al_2O_3	FeO	MnO	MgO	CaO	Na_2O	K_2O	P_2O_5	Cr_2O_3	NiO	Total
							Spinel							
H_2Osat-IHPV1	5	0.22 (0.11)	0.02 (0.02)	0.36 (0.03)	84.53 (0.39)	0.14 (0.12)	13.62 (0.21)	0.00 (0.00)	0.02 (0.03)	0.02 (0.02)	0.05 (0.03)	0.21 (0.02)	0.81 (0.15)	88.04 (0.55)
H_2Osat-PC20	1	0.79	0.77	4.25	70.92	0.25	11.08	0.00	0.03	0.07	0.01	1.90	0.54	90.61
H_2Osat-PC19	13	0.29 (0.07)	0.02 (0.03)	0.21 (0.04)	80.84 (0.61)	0.26 (0.10)	17.21 (0.18)	0.01 (0.01)	0.01 (0.02)	0.01 (0.01)	0.01 (0.02)	0.29 (0.04)	0.84 (0.27)	88.13 (0.76)
							Pyroxene compositions							
80PR-PC19	8	50.93 (0.65)	0.65 (0.08)	7.65 (0.43)	6.98 (0.32)	0.15 (0.09)	18.27 (0.54)	13.86 (0.45)	1.26 (0.08)	0.02 (0.02)	0.03 (0.02)	0.10 (0.03)	0.10 (0.08)	99.66 (0.77)
H_2Osat-PC19	6	58.62 (0.61)	0.04 (0.04)	0.04 (0.02)	2.58 (0.29)	0.09 (0.08)	38.40 (0.66)	0.10 (0.02)	0.01 (0.02)	0.00 (0.00)	0.01 (0.01)	0.01 (0.01)	0.10 (0.11)	101.88 (0.80)

nd – not determined
Numbers in parentheses represent one standard deviation.

2.2.3 Measured melt water contents

Water contents and infrared absorption spectra are shown in Table 2.5 and Fig. C.1, respectively. Small amounts of water was measured by FTIR, with a maximum measured water content in the melt phase of 1.88 ± 0.95 wt. % for experiment 12PR-PC4 (i.e. 12 wt. % melt, 1250 °C, 0.5 GPa and 72 h). The FTIR results are in agreement with the total weight deficits from EMP analyses performed on the same melts. To determine whether free water at grain boundaries could be present in these experiments, we calculated the water solubility in these melts (Iacono-Marziano et al., 2012, `https://www.calcul.isto.cnrs-orleans.fr/apps/h2o-co2-systems/`) and found that they could incorporate up to 13.49 wt. % H_2O (Table 2.5). The latter results, as well as the measured melt water contents, indicate that the melt phases did not reach their solubility threshold and that free water at grain boundaries is quite unlikely. However, this might not be the case for the nominally melt-free samples (i.e. 0PR samples). Such samples were not analyzed by FTIR.

Experiments 80PR-PC20 and 80PR-PC21 were run under the same T/P/time conditions but with different pressure media in the piston cylinder assembly (i.e. hematite and AlSiMag powders, respectively). The melt water contents differ by 0.2 wt. %, most presumably due to the hematite powder outside the capsule reacting with H_2 from the assembly through the reaction $Fe_2O_3 + H_2 = 2FeO + H_2O$. The hematite powder therefore acts as a barrier, limiting molecular hydrogen diffusion in and out of the capsules.

Based on the FTIR measurements, bulk and olivine water contents of the samples were calculated (Table 2.5) with the following equations:

$$C^{bulk}_{H_2O} = C^{melt}_{H_2O} \cdot \left(X^{melt} + (1 - X^{melt}) D^{ol/melt}_{H_2O} \right) \tag{2.2}$$

$$C^{ol}_{H_2O} = C^{melt}_{H_2O} \cdot D^{ol/melt}_{H_2O} \tag{2.3}$$

with $C^{bulk}_{H_2O}$, $C^{melt}_{H_2O}$ and $C^{ol}_{H_2O}$, the water concentrations in the bulk, the melt phase and olivine crystals, respectively, X^{melt}, the melt fraction and $D^{ol/melt}_{H_2O}$, the partitioning coefficient between olivine and melt, equal to $1.7 \cdot 10^{-3}$ (Hirschmann et al., 2009). These results show that as pressure increases, the bulk water contents increase accordingly.

Table 2.5 – Melt water contents analyzed by FTIR and calculated bulk water contents.

Sample	No. meas.	Melt water content (wt. %)	Water solubility (wt. %)	Bulk water content (wt. %)	Olivine water content (wt. ppm)
12PR-PC2	5	0.88 ± 0.45	10.15	0.11	14.88
12PR-PC4	2	1.88 ± 0.95	10.15	0.23	32.10
12PR-PC8	7	1.44 ± 0.74	8.76	0.17	24.48
80PR-PC20[a]	4	0.13 ± 0.01	13.49	0.11	2.25
80PR-PC21	6	0.34 ± 0.05	9.75	0.27	5.75
80PR-PC23	9	0.38 ± 0.05	10.15	0.30	6.37
80PR-PC26	3	0.63 ± 0.01	nd[b]	0.50	10.68

[a] Hematite experiment
[b] nd – not determined. Experimental conditions were outside the model limits of Iacono-Marziano et al. (2012).

Raman spectroscopy was used on sample 0PR-PC6 to determine the presence of volatiles, such as CO_2 or H_2O (Fig. 2.12). We observe that narrow peaks are present at 823, 855, 881, 920 and 958 cm^{-1}, which correspond to typical olivine signatures, whereas the peaks at 1110 and 1187 cm^{-1} results from the epoxy used to create the mount. The presence of CO_2 would be marked by a peak 1080 cm^{-1}, which is clearly not visible on Fig. 2.12(a). The presence of H_2O is usually marked by a peak in the range of 3550 and 3680 cm^{-1}. The melt phase in sample 0PR-

PC6 shows a small inflexion in this range, suggesting a very small amount of water, estimated <0.5 wt. %.

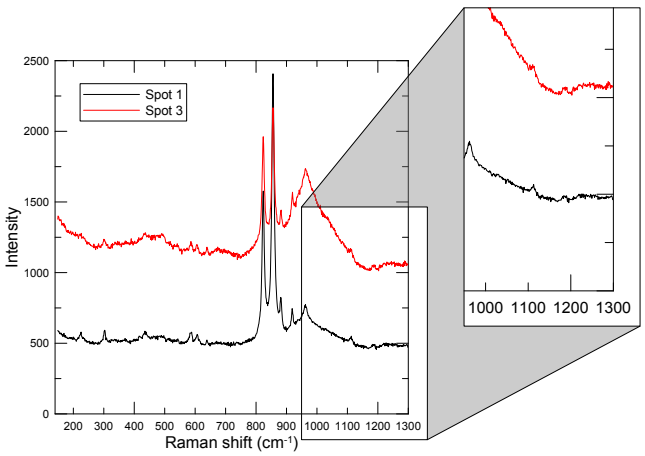

(a) Narrow peaks are typical olivine signatures. No noticeable peak at 1080 cm^{-1} is detected which would indicate the presence of CO_2.

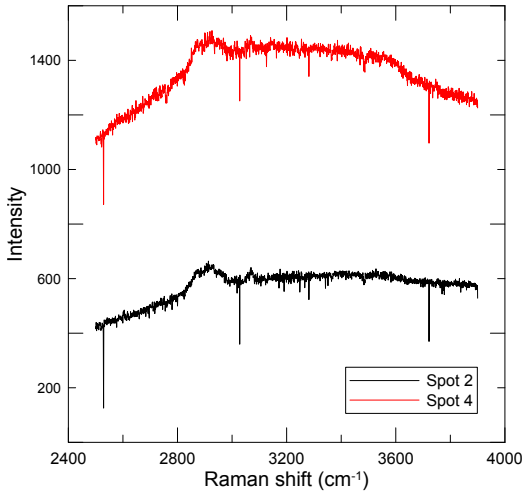

(b) A light inflexion for spot 2 can be observed, suggesting low water contents in the melt (<0.5 wt. %). The peak at 2900 cm^{-1} is due to CH-groups and is probably due to the epoxy used to mount the sample.

Figure 2.12 – Raman results on sample 0PR-PC6.

2.2.4 Grain size distributions

During normal grain growth, a self-similar distribution is expected, exhibiting the same shape at all times when plotted as a function of a normalized grain size. The normalized grain size corresponds to the grain size divided by a time-dependent grain size, which can be the average, mode or median (Faul and Scott, 2006, German and Olevsky, 1998). The distributions from this study are therefore normalized by the median as suggested by Keeping (1995), thus clearly showing the size halfway through the distribution (at $G/G_{median} = 1$).

The grain sizes display narrow self-similar distributions and suggest a time-invariant character as shown in Fig. C.2. Experimental samples containing ≤1 wt. % melt indicate a longer tail (Fig. C.2(b) to Fig. C.2(d)), which corresponds to bigger grain sizes than the median grain size. This feature could be due to faster growing grains in contact with melt, either at grain boundaries or at triple/quadruple junctions. For samples with >1 wt. % melt (Figs. C.3(a) and C.3(b)), this feature disappears, suggesting that the majority of the grains might be affected by the higher melt contents within the aggregates.

2.2.5 Evolution of grain size with time and temperature

Since the experiments were performed with different initial grain sizes (SM1, SM2 and sol-gel), the average grain sizes are illustrated in $\log_{10}$-$\log_{10}$ plots in Figs. 2.13 and 2.14, where the grain sizes are indicated as $G_f^2 - G_i^2$ as a function of annealing time. For convenience (and as justified in the next sections), the grain size exponent was chosen as $n = 2$. Note that for $n > 2$, the trends are unchanged, which does not impact the result description. Dry normal grain growth (NGG) of olivine melt-free aggregates are also illustrated as full lines in Figs. 2.13 and 2.14 for comparison. Dry NGG was calculated at the same T/P conditions in each figure with Eq. (1.11). Furthermore, the average grain size values and their respective uncertainties are also listed in Table 2.6. The uncertainties plotted in Figs. 2.13 and 2.14 were calculated using:

$$\begin{aligned}\Delta(G_f^2 - G_i^2)_{max} &= (G_f + \Delta G_{f,max})^2 - (G_i + \Delta G_{i,max})^2 \\ \Delta(G_f^2 - G_i^2)_{min} &= (G_f + \Delta G_{f,min})^2 - (G_i + \Delta G_{i,min})^2.\end{aligned} \tag{2.4}$$

Although we are aware that this kind of uncertainty propagation is not rigorous, it nonetheless indicates the maximum uncertainty on the calculated $G_f^2 - G_i^2$ values. The confidence interval for such calculated uncertainties is presumably above 2σ.

Grain growth being a time- and temperature-dependent process, we naturally observe that the average grain size increases with annealing time and increasing temperature at constant pressure condition. One exception is however apparent, namely sample 0PR-IHPV2 annealed at 1200 °C and 0.3 GPa for 1 h, exhibiting identical initial and final grain sizes. Potential reasons for its constant grain size might be due to the relatively short experimental duration combined to its very low melt contents (∼0 wt. % melt).

For experimental pressures ≤0.5 GPa, Figs. 2.13(a), 2.13(b) and 2.14(a) indicate no considerable difference in grain growth rates (within calculated uncertainties), regardless of melt and water contents or applied pressure media. To better illustrate this observation, as an example at 1250 °C, 0.5 GPa and 72 h (Fig. 2.14(a)) average grain sizes from the different starting materials (e.g. variable melt and water contents) are indistinguishable.

For all T/P/time conditions, H_2O-saturated samples display similar grain sizes as nominally melt-free samples. Nevertheless, as previously highlighted, these samples present secondary phases (i.e. spinel and pyroxenes), which could have acted as inhibitors for grain growth (i.e. Zener pinning; Atkinson, 1988, Evans et al., 2001, Hiraga et al., 2010, Smith, 1948, Tasaka and Hiraga, 2013).

At 0.5 GPa, comparison between hematite and AlSiMag experiments reveals that the measured grain sizes are of the same order, regardless of the melt content (Fig. 2.14(a)). However, at higher pressure (1.5 GPa) and for nominally melt-free samples, hematite experiments present smaller grain sizes than AlSiMag experiments by one order of magnitude (Fig. 2.14(b)).

Finally, the Fe-free sol-gel olivine shows very low growth rates compared to the naturally-derived samples at the same temperature conditions (diamond vs. squared symbols in Fig. 2.14). This sample is appropriately modeled by dry NGG (within uncertainties).

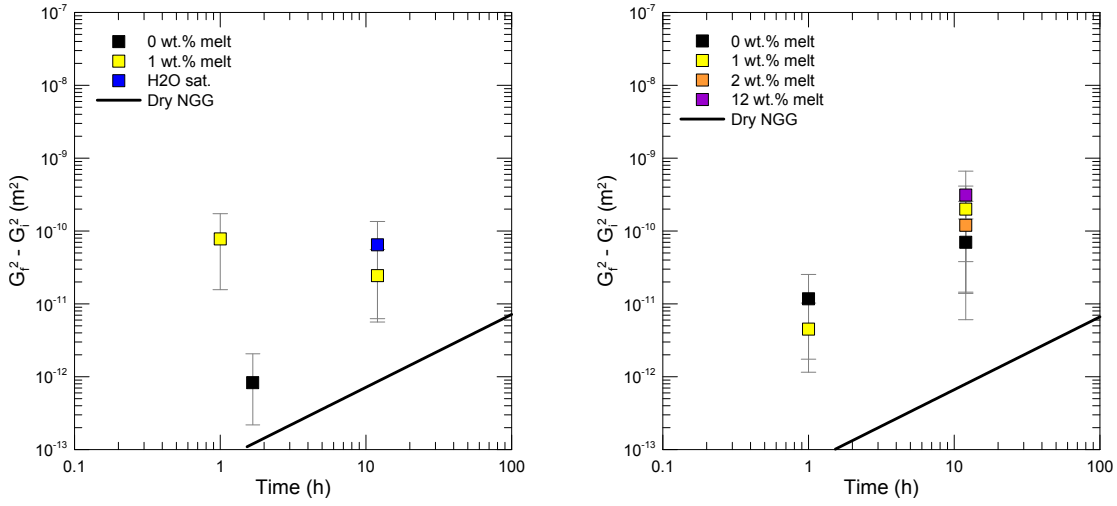

(a) T = 1200 °C – P = 0.3 GPa.

(b) T = 1200 °C – P = 0.5 GPa.

Figure 2.13 – Log_{10}-log_{10} plot of grain size vs. time. Squared symbols indicate AlSiMag experiments whereas rounded symbols represent hematite experiments. Full lines indicate dry normal grain growth (NGG) of olivine aggregates calculated at the same T/P conditions with Eq. (1.11).

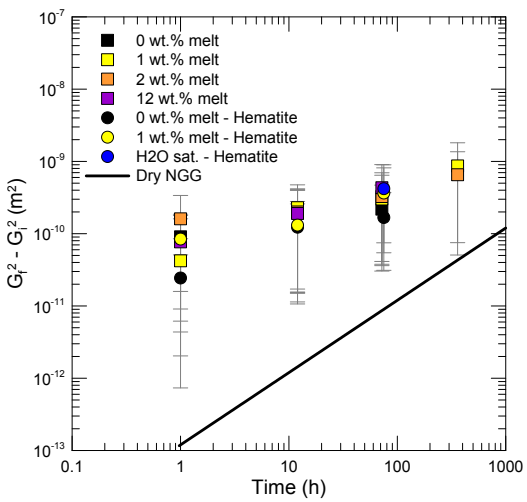

(a) T = 1250 °C – P = 0.5 GPa

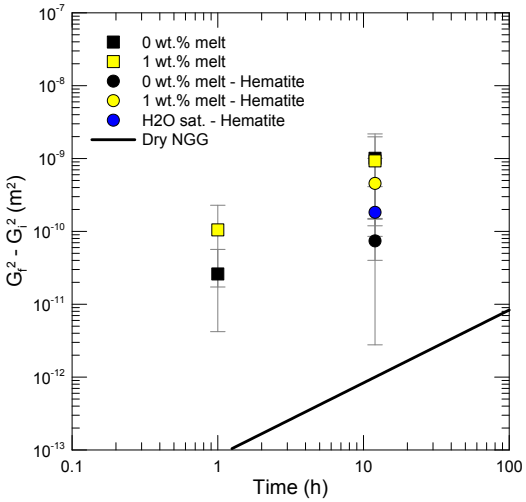

(b) T = 1250 °C – P = 1.5 GPa

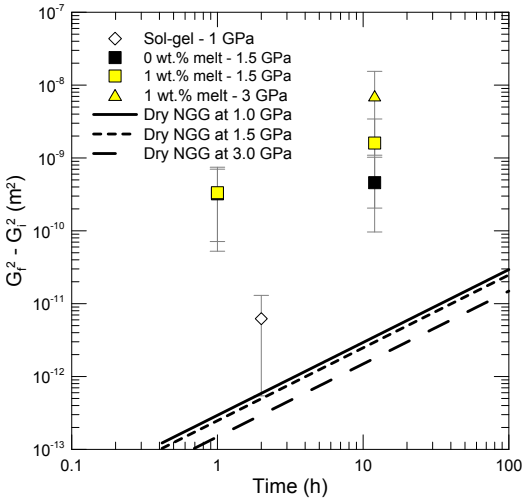

Figure 2.14 – Log_{10}-log_{10} plot of grain size vs. time at T = 1350 °C and P = 1.0 to 3.0 GPa. Squared symbols indicate AlSiMag experiments whereas rounded symbols represent hematite experiments. Full lines indicate dry normal grain growth (NGG) of olivine aggregates calculated at the same T/P conditions with Eq. (1.11).

Table 2.6 – Experimental grain sizes – Final grain size corresponds here to the average measured grain size.

Run No.	Sample	Initial grain size (µm)	Final grain size (µm)	Number of grains
IHPV2	0PR	10.84 ± 1.06	10.87 ± 0.97	100
	1PR	5.33 ± 0.20	10.31 ± 0.90	100
IHPV1	1PR	5.33 ± 0.20	7.27 ± 0.60	100
	H_2O sat.	10.84 ± 1.06	13.50 ± 1.06	100
PC12	0PR	5.33 ± 0.20	6.34 ± 0.31	507
	1PR	5.33 ± 0.20	5.74 ± 0.29	600
PC8	0PR	5.33 ± 0.20	9.93 ± 0.42	935
	1PR	5.33 ± 0.20	15.11 ± 0.54	625

Experimental grain sizes (continued).

Run No.	Sample	Initial grain size (µm)	Final grain size (µm)	Number of grains
	2PR	5.33 ± 0.20	12.18 ± 0.70	428
	12PR	5.33 ± 0.20	18.45 ± 1.12	226
PC2	0PR	5.33 ± 0.20	10.91 ± 0.30	1126
	1PR	5.33 ± 0.20	8.40 ± 0.17	1954
	2PR	5.33 ± 0.20	13.75 ± 0.67	443
	12PR	5.33 ± 0.20	10.28 ± 0.41	706
PC4	0PR	5.33 ± 0.20	15.06 ± 0.43	1273
	1PR	5.33 ± 0.20	16.06 ± 0.54	492
	2PR	5.33 ± 0.20	15.11 ± 0.65	597
	12PR	5.33 ± 0.20	14.80 ± 0.61	585
PC23	80PR	10.84 ± 1.06	29.99 ± 8.99	14
PC5	0PR	5.33 ± 0.20	15.72 ± 1.07	243
	1PR	5.33 ± 0.20	18.18 ± 1.13	244
	2PR	5.33 ± 0.20	18.84 ± 1.19	211
	12PR	5.33 ± 0.20	21.48 ± 0.91	453
PC6	0PR	5.33 ± 0.20	22.73 ± 1.55	146
	1PR	5.33 ± 0.20	29.92 ± 1.32	642
	2PR	5.33 ± 0.20	26.13 ± 1.03	798
	12PR	5.33 ± 0.20	26.80 ± 1.08	386
PC15	0PR	5.33 ± 0.20	7.27 ± 0.29	100
	1PR	5.33 ± 0.20	10.62 ± 0.54	451
PC14	0PR	5.33 ± 0.20	12.31 ± 0.56	794
	1PR	5.33 ± 0.20	12.64 ± 0.71	100
PC20	0PR	10.84 ± 1.06	16.88 ± 1.65	100
	1PR	5.33 ± 0.20	19.85 ± 2.04	100
	80PR	10.84 ± 1.06	34.43 ± 8.94	40
	H_2O sat.	10.84 ± 1.06	23.17 ± 1.71	100
PC16	0PR	5.33 ± 0.20	7.38 ± 0.44	480
	1PR	5.33 ± 0.20	11.55 ± 0.87	100
PC13	0PR	5.33 ± 0.20	32.21 ± 2.40	270
	1PR	5.33 ± 0.20	30.94 ± 2.03	366
PC19	0PR	10.84 ± 1.06	13.84 ± 0.92	100
	1PR	5.33 ± 0.20	22.01 ± 2.09	100
	H_2O sat.	10.84 ± 1.06	17.33 ± 1.89	100
PC25	Fo100	1.00 ± 0.10	2.69 ± 0.14	100
PC17	0PR	5.33 ± 0.20	18.72 ± 1.52	177
	1PR	5.33 ± 0.20	19.02 ± 2.04	100
PC18	0PR	5.33 ± 0.20	22.07 ± 2.36	100
	1PR	5.33 ± 0.20	40.39 ± 2.65	331
PC27	1PR	5.33 ± 0.20	84.68 ± 6.72	100

2.2.6 Melt effect

To account for the melt effect, grain sizes determined from experiments at 1250 °C and 0.5 GPa are plotted as a function of melt content in Fig. 2.15. Except for the 1 h-long experiment (white squared symbols in Fig. 2.15), which shows inconsistent grain growth with increasing melt content, average grain sizes remain constant for melt contents <25 wt. %, regardless of the experimental duration. Despite the chemical heterogeneities detected in the 15 day-long experiment (black squared symbols in Fig. 2.15), the measured grain sizes in these samples are greater than experiments run for shorter durations.

Furthermore, comparison of dry normal grain growth (NGG) with melt-bearing aggregates (full lines vs. symbols in Figs. 2.13 and 2.14) shows that grain growth for melt-bearing aggregates is clearly affected by the melt content, even at very low melt percentages (i.e. $\ll$1 wt. % melt). The sol-gel sample (diamond symbol in Fig. 2.14) is relatively well constrained by the dry NGG model, indicating that it is the only sample from this experimental study that is genuinely melt-free.

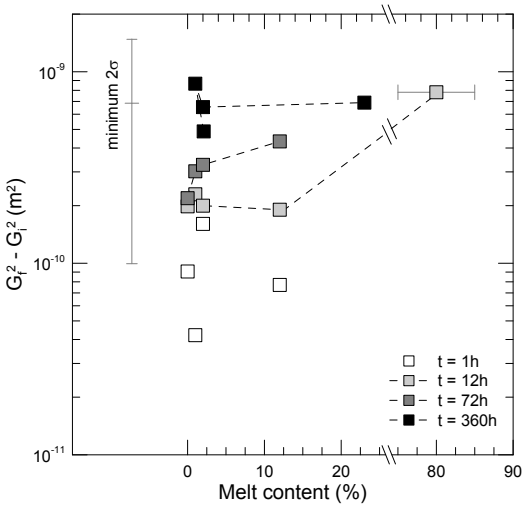

Figure 2.15 – Melt effect at 1250 °C and 0.5 GPa.

2.2.7 Pressure effect

To better illustrate the pressure effect on grain growth, Fig. 2.16 depicts the grain sizes as a function of pressure. Two temperatures were investigated at different pressures, namely 1250 °C at 0.5 and 1.5 GPa and 1350 °C at 1.0 to 3.0 GPa. For experiments run at 1250 °C (Fig. 2.16(a)), there is no significant change with increasing pressure. The absolute values of the grain sizes seem however to indicate a decrease with increasing pressure. This trend is likely due to crystallization of the melt phase with increasing pressure, therefore increasing the small grain size content. At higher temperature (i.e. 1350 °C, Fig. 2.16(b)), we observe an increase of the average absolute grain size with increasing pressure. For such high temperatures, no melt crystallization is expected which indicates that pressure most likely has an increasing effect on grain growth rates.

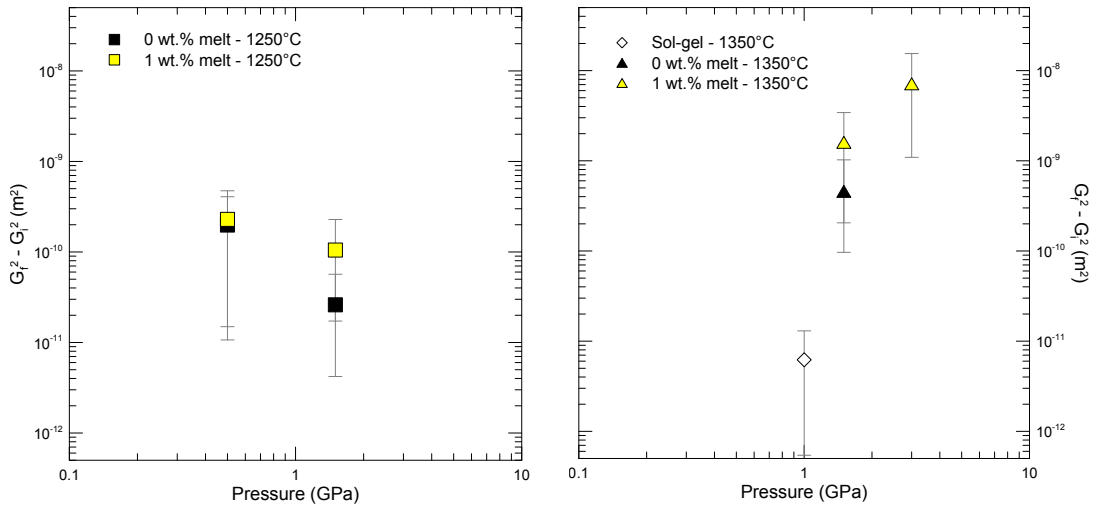

(a) Pressure effect at 1250 °C

(b) Pressure effect at 1350 °C

Figure 2.16 – Grain size as a function of pressure.

2.3 On the theoretical grain growth for melt-bearing aggregates

If crystals are dispersed in a matrix consisting of a secondary phase, either solid or liquid (i.e. melt or fluid), the difference in surface area between the large and small grains is the driving force for grain growth and therefore leads to a difference in solubility. This type of grain growth is known as Otswald ripening, which was first considered by Greenwood (1956) and later derived by Lifshitz and Slyozov (1961), Wagner (1961) (i.e. the LSW theory).

This theory considers that for an ideal solution of α crystalline phase, of composition $C^i_\alpha \approx 1$ and mean radius $\bar{r}$, dispersed in a β phase, in which component i is very dilute (i.e. $C^i_\beta(\infty) \approx 0$), the solubility of species i in β may be written as:

$$d\mu = RT \ln \left(\frac{C^i_\beta(r)}{C^i_\beta(\infty)} \right) \tag{2.5}$$

where $d\mu = \mu^i_\alpha - \mu^i_\beta$ is the chemical potential gradient (in J mol^{-1}) and $C^i_\beta(r)$ is the concentration of i in β (in mole fraction) at the interface with a spherical grain α of radius r (in m).

Since $d\mu = \alpha^* \gamma \Omega / r$ (i.e. the Gibbs-Thompson equation*), we get:

$$\ln \frac{C^i_\beta(r)}{C^i_\beta(\infty)} = \frac{\alpha^* \gamma \Omega}{rRT} \tag{2.6}$$

with $\alpha^* = 2$, γ, the interfacial energy (in J m^{-2}) and Ω, the molar volume of the growing crystal (in m^3 mol^{-1}). The right-hand-side of the latter equation being generally $\ll 1$, Eq. (2.6) is usually simplified to:

$$C^i_\beta(r) = C^i_\beta(\infty) \left(1 + \frac{\alpha^* \gamma \Omega}{rRT} \right). \tag{2.7}$$

If the system behaves as an ideal solution, then the equilibrium concentration of i in β is equal to that in equilibrium with a grain α of radius $\bar{r}$, so that $C^i_\beta(\infty) = C^i_\beta(\bar{r})$. This means that the β phase will be locally oversaturated in i at the contact with grains α with $r > \bar{r}$, therefore

*For reading convenience, the term α from Section 1.2 is in this chapter referred to as α^*.

precipitating additional α on the existing grains, whereas phase β will be locally undersaturated in species i at the contact with grains α of radius $r < \bar{r}$, thus dissolving α grains.

Fig. 2.17 illustrates the concentration profiles of a solute in a secondary liquid phase between a small and a large grain in case of diffusion-controlled (Fig. 2.17(a)) and in case of interface reaction-controlled (Fig. 2.17(b)) grain growths. The LSW theory therefore predicts a stationary grain size distribution and steady-state kinetic equations, where the cube (in case of diffusion-control) or the square (in case of interface reaction-control) of the average grain size is proportional to the annealing time.

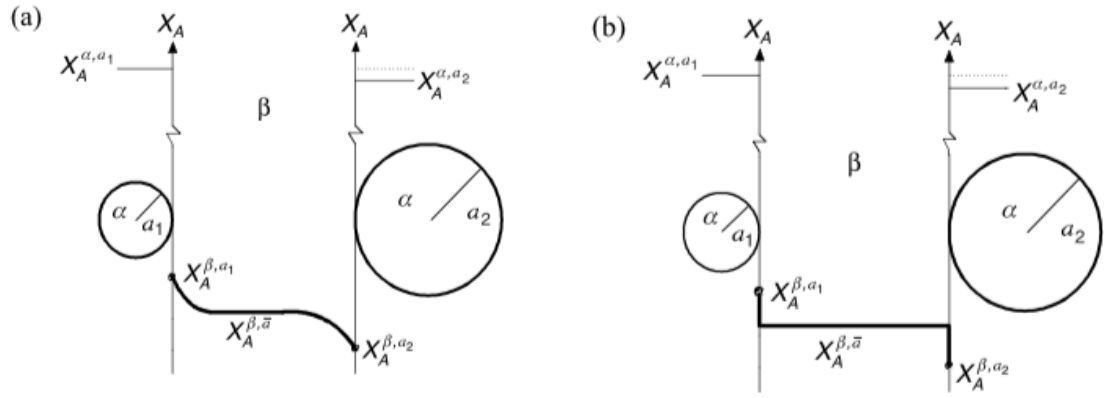

(a) Diffusion-controlled grain growth

(b) Interface-reaction controlled grain growth

Figure 2.17 – Illustration of solute concentration gradient in a liquid matrix between two particles of size a_1 and a_2 for (a) diffusion-controlled and (b) interface-reaction controlled grain growths (from Kang, 2005). Here X_A^{α,a_1} and X_A^{α,a_2} are the mole fractions of A in phase α of grains a_1 and a_2, respectively; X_A^{β,a_1}, X_A^{β,a_2} and $X_A^{\beta,\bar{a}}$ are the mole fractions of A in phase β of grains a_1, a_2 and of the average sized grain, $\bar{a}$, respectively. Note that a, X_A^{α} and X_A^{β} are respectively denoted r, C_α^i and C_β^i in the text.

Since we are interested in growth rates in the presence of a liquid phase to explain the experimental liquid-bearing olivine grain growths in our study, we will be demonstrating hereafter the theory for liquid-controlled crystal growth in the case of diffusion-limited and interface reaction-controlled grain growths.

2.3.1 Diffusion-limited grain growth

The classic expression for diffusion-limited grain growth based on the LSW theory is as follows (Greenwood, 1956, 1969, Kang, 2005, Martin and Doherty, 1976):

$$r_f^3 - r_i^3 = \frac{8}{9}\frac{\alpha^* \cdot \gamma_{sl} \cdot \Omega \cdot D_l^i \cdot C_l^i(\infty)}{RT}t, \tag{2.8}$$

where r_f and r_i are the grain radii (in m) at time t (in s) and $t = 0\,\mathrm{s}$, respectively, γ_{sl} is the interfacial energy at the liquid/crystal interface, D_l^i is the diffusion coefficient of species i in the liquid (in $\mathrm{m^2\,s^{-1}}$) and C_l^i is the concentration of species i in the liquid (in $\mathrm{mol\,m^{-3}}$). This equation is however unsatisfactory since it is strikingly similar to lattice diffusion-limited grain growth, as indicated in Eq. (1.10), where the distance between two grains separated by a liquid phase is not taken into consideration. Since diffusion within the liquid must take place across the liquid distance, δ_l, we thus expect δ_l to influence grain growth rates, as for grain boundary diffusion-limited grain growth (Eq. (1.9)). We therefore apply here the same formalism as in Chapter 1 in order to derive the grain growth equation for liquid diffusion-limited grain growth.

We consider here that the driving force for grain growth, F (in N), is related to the chemical potential, $d\mu$ (in $\mathrm{J\,mol^{-1}}$) and the pressure gradient, ΔP (in Pa) by (Burke and Turnbull, 1952):

$$F = \frac{d\mu}{\delta_l} = \frac{\Omega d(\Delta P)}{\delta_l} \tag{2.9}$$

where δ_l is the liquid width between two grains (in m). As demonstrated in Chapter 1, by using the total grain volume change (Eq. (1.6)), Fick's first law (Eq. (1.7)) and the driving force, F (Eq. (2.9)), we get:

$$\frac{dr}{dt} = \frac{\alpha^* \cdot \gamma_{sl} \cdot \Omega^2 \cdot D_l^i \cdot C_l^i}{\delta_l \cdot r \cdot \xi \cdot RT}. \tag{2.10}$$

To determine δ_l, we have investigated two melt configurations: (i) $\delta_l \ll r$, (ii) $\delta_l \gg r$ (Fig. 2.18(a)). We have also examined the influence of melt residing in triple junctions (Fig. 2.18(b)). Derivation of these growth kinetics are explained in the following sections.

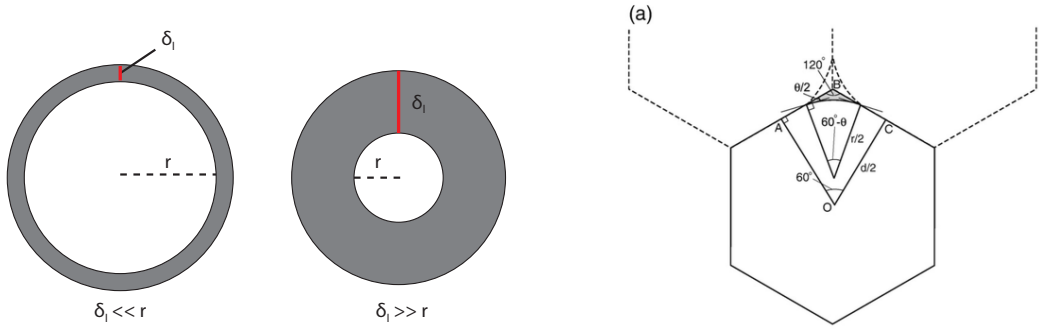

(a) Spherical grain of radius r surrounded by a liquid layer of width δ_l

(b) Liquid residing in a triple junction

Figure 2.18 – Liquid geometries for liquid diffusion-controlled grain growth. (b) is from Takei and Hier-Majumder (2009).

2.3.1.1 Liquid diffusion-limited grain growth with $\delta_l \ll r$

As depicted in Fig. 2.18(a), the melt volume is $V_{melt} = 4\pi r^2 \delta_l/2$, and the grain volume is $V_{grain} = 4/3\pi r^3$. As a consequence, the fraction of melt, Φ, is:

$$\Phi = \frac{V_{melt}}{V_{grain}} = \frac{3\delta_l}{2r}. \tag{2.11}$$

The liquid width therefore is a function of melt and grain radius, and by substitution in Eq. (2.10), we get:

$$\frac{dr}{dt} = \frac{3}{2}\frac{\alpha^* \cdot \gamma_{sl} \cdot \Omega^2 \cdot D_l^i \cdot C_l^i}{r^2 \cdot \Phi \cdot \xi \cdot RT}. \tag{2.12}$$

By integration, Eq. (2.12) becomes:

$$r_f^3 - r_i^3 = \frac{9}{2}\frac{\alpha^* \cdot \gamma_{sl} \cdot \Omega^2 \cdot D_l^i \cdot C_l^i}{\Phi \cdot \xi \cdot RT}\, t. \tag{2.13}$$

The grain size exponent is here $n = 3$. Note that if the grain diameter, G, is used instead of r, then Eq. (2.13) is:

$$G_f^3 - G_i^3 = 36\,\frac{\alpha^* \cdot \gamma_{sl} \cdot \Omega^2 \cdot D_l^i \cdot C_l^i}{\Phi \cdot \xi \cdot RT}\, t. \tag{2.14}$$

2.3.1.2 Liquid diffusion-limited grain growth with $\delta_l \gg r$

For this type of melt configuration, the melt volume is (Fig. 2.18(a)):

$$V_{melt} = \frac{4}{3}\pi\left(r + \frac{\delta_l}{2}\right)^3 - \frac{4}{3}\pi r^3. \tag{2.15}$$

The melt fraction therefore becomes:

$$\begin{aligned} \Phi &= \frac{4/3\pi\left(r + \delta_l/2\right)^3 - 4/3\pi r^3}{4/3\pi r^3} \\ &= \frac{\left(r + \delta_l/2\right)^3}{r^3} - 1 \\ &= \left(1 + \frac{\delta_l}{2r}\right) - 1. \end{aligned} \tag{2.16}$$

For $\delta_l \ll 1$, we have the same equation as Eq. (2.11), whereas for $\delta > 1$, the liquid width is:

$$\delta_l = 2r\left(\sqrt[3]{\Phi + 1} - 1\right). \tag{2.17}$$

By substitution in Eq. (2.10), we get:

$$\frac{dr}{dt} = \frac{\alpha^* \cdot \gamma_{sl} \cdot \Omega^2 \cdot D_l^i \cdot C_l^i}{2\,r^2 \cdot \left(\sqrt[3]{\Phi + 1} - 1\right) \cdot \xi \cdot RT}, \tag{2.18}$$

and by integration, Eq. (2.18) leads to:

$$r_f^3 - r_i^3 = \frac{3}{2}\frac{\alpha^* \cdot \gamma_{sl} \cdot \Omega^2 \cdot D_l^i \cdot C_l^i}{\left(\sqrt[3]{\Phi + 1} - 1\right) \cdot \xi \cdot RT}\,t. \tag{2.19}$$

This configuration also produces a grain size exponent of $n = 3$. Note that if the grain diameter, G, is used instead of r, then Eq. (2.19) is:

$$G_f^3 - G_i^3 = 12\,\frac{\alpha^* \cdot \gamma_{sl} \cdot \Omega^2 \cdot D_l^i \cdot C_l^i}{\Phi \cdot \xi \cdot RT}\,t. \tag{2.20}$$

2.3.1.3 Liquid diffusion-limited grain growth in triple junctions

Following the work of Takei and Hier-Majumder (2009), the pressure gradient, $\Delta P = \alpha^*\gamma_{sl}/R$ (with R, the mean curvature in m), is calculated as a function of the melt fraction with:

$$R = 4r\beta\sqrt{1 - \Phi} \tag{2.21}$$

with $\beta = \sqrt{\sqrt{3}/(2\pi)}$, a geometrical factor. The driving force, F, for grain growth therefore becomes:

$$F = \frac{\Omega\alpha^*\gamma_{sl}}{4r\beta\sqrt{1 - \Phi} \cdot \delta_l}. \tag{2.22}$$

Combination of Eqs. (1.6), (1.7), (2.9) and (2.22) leads to:

$$\frac{dr}{dt} = \frac{\alpha^* \cdot \gamma_{sl} \cdot \Omega^2 \cdot D_l^i \cdot C_l^i}{4r\beta\sqrt{1 - \Phi} \cdot \delta_l \cdot \xi \cdot RT}, \tag{2.23}$$

Integration of the latter equation leads to:

$$r_f^2 - r_i^2 = \frac{1}{2}\frac{\alpha^* \cdot \gamma_{sl} \cdot \Omega^2 \cdot D_l^i \cdot C_l^i}{\beta\sqrt{1 - \Phi} \cdot \delta_l \cdot \xi \cdot RT}\,t, \tag{2.24}$$

indicating that the grain size exponent is in this case $n = 2$. If G is used instead of r, then Eq. (2.25) becomes:

$$G_f^2 - G_i^2 = 2\,\frac{\alpha^* \cdot \gamma_{sl} \cdot \Omega^2 \cdot D_l^i \cdot C_l^i}{\beta\sqrt{1-\Phi} \cdot \delta_l \cdot \xi \cdot RT}\,t. \tag{2.25}$$

2.3.2 Interface reaction-controlled grain growth

Generally, the rate of diffusion, as demonstrated in the former section, is assumed to be slower than the rate of dissolution/precipitation at the liquid/crystal interface, mainly through the higher grain size exponent ($n = 3$) and through the fast liquid diffusion coefficient, D_l^i. Since the driving force for grain growth or dissolution of an α grain of radius r is the difference between the concentration of i at the liquid/crystal interface, $C_l^i(r)$, and the mean concentration of i in the matrix, $C_l^i(\bar{r})$, we get (Greenwood, 1969, Martin and Doherty, 1976):

$$\frac{dr}{dt} = K_s^i \left(C_l^i(\bar{r}) - C_l^i(r)\right) \tag{2.26}$$

with K_s^i, the constant of dissolution/precipitation at the liquid/crystal interface (in $\mathrm{m\,s^{-1}}$). By substituting Eq. (2.7) into Eq. (2.26), the rate of grain growth by dissolution/precipitation therefore becomes:

$$\frac{dr}{dt} = \frac{\alpha^* \cdot \gamma_{sl} \cdot \Omega \cdot K_s^i \cdot C_l^i(\infty)}{RT}\left(\frac{1}{\bar{r}} - \frac{1}{r}\right). \tag{2.27}$$

Furthermore, the grain size distribution of dissolution/precipitation-limited grain growth reaches a steady-state when the average grain size is $\bar{r} = 8/9r$ (Kang, 2005), which leads to the final integrated form of Eq. (2.27):

$$r_f^2 - r_i^2 = \frac{128}{81}\,\frac{\alpha^* \cdot \gamma_{sl} \cdot \Omega \cdot K_s^i \cdot C_l^i(\infty)}{RT}\,t. \tag{2.28}$$

The latter equation differs from that of Wagner (1961) through the proportionality constant, which was predicted to be 32/81 by considering that $\bar{r} = 4/9r$ during steady-state grain growth.

Notice that if G is used instead of r, then Eq. (2.28) becomes:

$$G_f^2 - G_i^2 = \frac{512}{81}\,\frac{\alpha^* \cdot \gamma_{sl} \cdot \Omega \cdot K_s^i \cdot C_l^i(\infty)}{RT}\,t. \tag{2.29}$$

2.4 Discussion

2.4.1 Comparison to previously published melt-bearing and H_2O-saturated olivine aggregates

We compare here our experimental results for melt-bearing and H_2O-saturated olivine aggregates with previously published experiments on the same type of aggregates. To our knowledge, two studies have investigated the melt effect on olivine grain growth, namely the study of Cabane et al. (2005), which was conducted at atmospheric pressure and with high melt contents (47 wt. % melt), and the study of Faul and Scott (2006), under high pressure conditions (1 GPa) and for lower melt contents (2 and 4 wt. % melt). As for H_2O-saturated olivine aggregates, we have compared our data to the studies of Ohuchi and Nakamura (2007a,b), Ohuchi et al. (2010). The comparison is illustrated in Fig. 2.19 where the growth rate ($(G_f^2 - G_i^2)/t$) is plotted as a function of absolute reciprocal temperature. We have also plotted dry olivine grain growth rates calculated with Eq. (1.9) at P = 1 atm and t = 763 h (i.e. the longest experimental duration from the grain growth database) to insist that melt and water does indeed increase olivine growth rates, regardless of the applied confining pressure: the orange diamonds, which contain high melt contents (Cabane et al., 2005) at 1 atm, display faster growth rates than dry NGG.

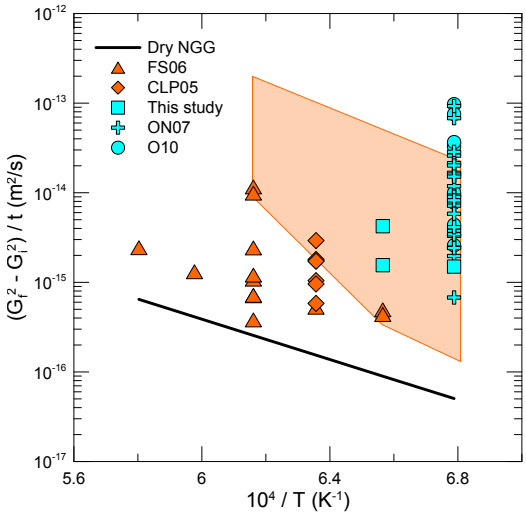

Figure 2.19 – Growth rates as a function of absolute reciprocal temperature. Orange symbols are for melt-bearing olivine aggregates (FS06: 2 and 4 wt. % melt, Faul and Scott (2006); CLP05: 47 wt. % melt, Cabane et al. (2005)) and blue symbols are for H_2O-saturated olivine aggregates (ON07: Ohuchi and Nakamura (2007a,b), O10: Ohuchi et al. (2010)). The orange zone corresponds to the growth rates of the melt-bearing aggregates from this study. The black line corresponds to dry normal grain growth of olivine aggregates calculated at P = 1 atm and for t = 763 h (i.e. longest duration of the plotted experimental data in this figure) with Eq. (1.11).

Firstly, we observe that our experimental results are in agreement with published data on these types of aggregates, whether they contain a melt or fluid phase. Secondly, we note that the complete dataset displays considerable scatter, in particular at fixed temperature, where the grain growth rates range well over two orders of magnitude. Since the theoretical background for liquid-bearing aggregate growth rates cannot explain this experimental scattering, we suggest that it could be due to the homogeneity of the starting material. As observed on our SEM images, the melt is not distributed homogeneously within the aggregates, meaning that a certain portion of grain boundaries are not wetted by an interstitial liquid phase. Grain growth in liquid-bearing aggregates should therefore result from a combination of (liquid-free) grain boundary migration and of interstitial liquid-controlled boundary migration. This type of process has already been suggested for liquid phase sintering of metallic alloys (Lu and German, 2001, Yang et al., 1990, among others), introducing a contiguity term, Ψ, which is defined by "the portion of the grain surface being in contact with the neighboring grains" (with $0 < \Psi < 1$, Takei, 1998). Contiguity, as well as its complementary parameter the wetness ($\varphi = 1 - \Psi$), are also highly used for the understanding of geological processes, notably in deformation processes, where grain-grain contacts have different physical properties than grain-liquid contacts (Garapić et al., 2013, Takei, 1998, 2002, Takei and Holtzman, 2009a,b,c, Walte et al., 2003, Yoshino et al., 2005, 2009).

As a result, to model liquid-controlled olivine grain growth, we employ the following formalism as suggested by Lu and German (2001):

$$\frac{dr}{dt} = \Psi \left.\frac{dr}{dt}\right|_{dry\,NGG} + \varphi \left.\frac{dr}{dt}\right|_{liquid\,NGG} \tag{2.30}$$

where $dr/dt|_{dry\,NGG}$ refers to Eq. (1.8) and $dr/dt|_{melt\,NGG}$ refers to one of the previously demonstrated liquid-controlled growth rates (i.e. Eqs. (2.12), (2.18), (2.23) and (2.27)).

Since we have not measured the wetness in the course of this study and because the studies of Cabane et al. (2005), Faul and Scott (2006), Ohuchi and Nakamura (2007a,b), Ohuchi et al. (2010) have not constrained this parameter neither, we have used the study of Yoshino et al. (2005) to constrain wetness as a function of the liquid content in melt-bearing olivine aggregates.

In the latter study, experiments were conducted under high pressure (1 GPa) and high temperature (1200 to 1350 °C) conditions in order to obtain textural equilibrium between the melt phase and the solid olivine crystals. Melt fractions and wetness of the grain boundaries were then measured by segmentation of SEM images of their experimental samples and a power-law relationship was established, so that $\varphi = A\Phi^{1/2}$, with $A = 2.3$ and Φ, the melt fraction. As illustrated in Fig. 2.20 (full black line), this relation does not hold since for $\Phi = 1$, $\varphi > 1$. We have therefore recalibrated this relationship (full red line in Fig. 2.20), leading to $\varphi = \Phi^{0.22}$, where for $\Phi = 1$, $\varphi = 1$. We will hereafter be using the latter relationship to model liquid-bearing aggregate growth rates.

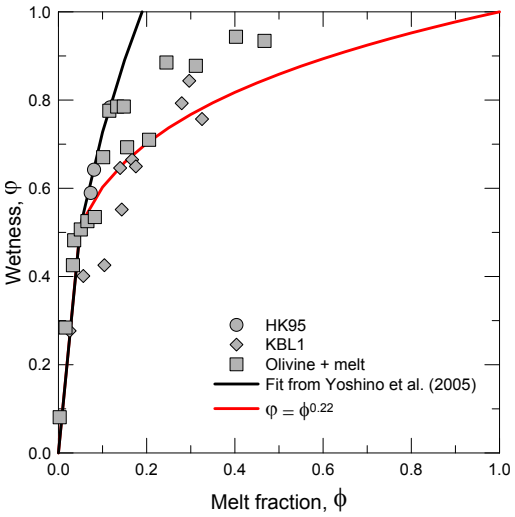

Figure 2.20 – Calibration of wetness as a function of melt fraction. Diamond (KBL1) and squared (olivine + melt) symbols are from the experiments performed by Yoshino et al. (2005), circle symbols are from the study of Hirth and Kohlstedt (1995a,b) (P = 0.3 GPa). The full black line represents the fit from Yoshino et al. (2005) where $\varphi = 2.3\Phi^{1/2}$ indicating that for $\Phi = 1$, $\varphi > 1$ whereas the full red line indicates our fit with $\varphi = \Phi^{0.22}$.

2.4.2 Are liquid-bearing olivine aggregates controlled by liquid diffusion-limited processes?

To test whether liquid-bearing olivine aggregates are controlled by diffusion through the liquid, we have simulated grain growths with the different geometrical melt configurations indicated in Section 2.3. The results are presented in a calculated final grain size vs. $\log_{10}(t)$ plot in Fig. 2.21, with a temperature of 1250 °C, a pressure of 0.5 GPa, an initial grain size of $G_i = 5.3\,\mu$m. The other parameters in Eqs. (2.13), (2.19) and (2.25) are $\gamma_{sl} = 0.5\,\mathrm{J\,m^{-2}}$ (Takei and Hier-Majumder, 2009, Takei and Holtzman, 2009b), $\Omega = 43.8\,\mathrm{cm^3}$ for forsterite (Gottschalk, 1997), $C_l = 2.44 \cdot 10^4\,\mathrm{mol\,m^{-3}}$ (EMP analyses from this study), $\xi = 0.5$ defined from the forsterite stoichiometry, and $D_l = 5.1 \cdot 10^{-12}\,\mathrm{m^2\,s^{-1}}$ at T = 1250 °C from Lesher et al. (1996). The melt fraction was fixed in our model at 0.02 in order to compare the results to the experimental grain sizes measured in this study at the same T/P/G_i/Φ conditions (gray zone in Fig. 2.21). The dry NGG implementation in the modeling (through Eq. (2.30)) uses the same parameters as in Chapter 1.

First, we have simply tested Eq. (2.10) at a fixed δ_l of 25 nm (as estimated from SEM imaging), which is the blue full line in Fig. 2.21. Diffusion through the melt phase is therefore too important and results in grain sizes that are $\sim$ 2 orders of magnitude greater than measured grain sizes from this study. On the opposite, dry NGG (full black line) is nearly too slow to appropriately model melt-bearing aggregate grain growths, as already outlined in the former sections.

Secondly, we have tested Eqs. (2.13) and (2.19) (i.e. $\delta_l \ll r$ and $\delta \gg r$), represented by the green lines in Fig. 2.21. We would like to highlight that although we used here Eq. (2.30), we are aware that it is analytically difficult to perform such integration since these growth rates present a grain size exponent of $n = 3$ and that dry NGG implies $n = 2$. This figure thus indicates the order of magnitude we expect for $\delta_l \ll r$ and $\delta_l \gg r$ and helps us determine whether this type of geometry could indeed explain the higher growth rates for liquid-bearing aggregates. The green lines in Fig. 2.21 start at a grain size of $G = \sim 15\,\mu m$ which is a result from the mathematical approximation we have used here. Notwithstanding, the grain sizes resulting from these geometries (Fig. 2.18(a)) are greater than the experimental grain sizes measured in this study, indicating that liquid diffusion-controlled grain growth rates are too fast for this type of geometry.

For melt residing in tubes (Fig. 2.18(b)), we have used a realistic melt layer of $\delta_l = 25\,nm$ as represented by the full red line in Fig. 2.21, which disagrees with the measured grain sizes from this study. To understand the effect of δ_l on the resulting grain sizes, we have therefore used a wider δ_l of $1\,\mu m$ as illustrated by the dashed red line. Increasing δ_l produces slower growth rates, which could be in agreement with the experimental grain sizes. However, as indicated by the microstructure results in this study and **??**, the low melt contents considered in our model ($\Phi = 0.02$) do not generate such large melt layers.

As a consequence, we can conclude here that diffusion through the melt induces faster grain growth rates than those observed in experimental studies.

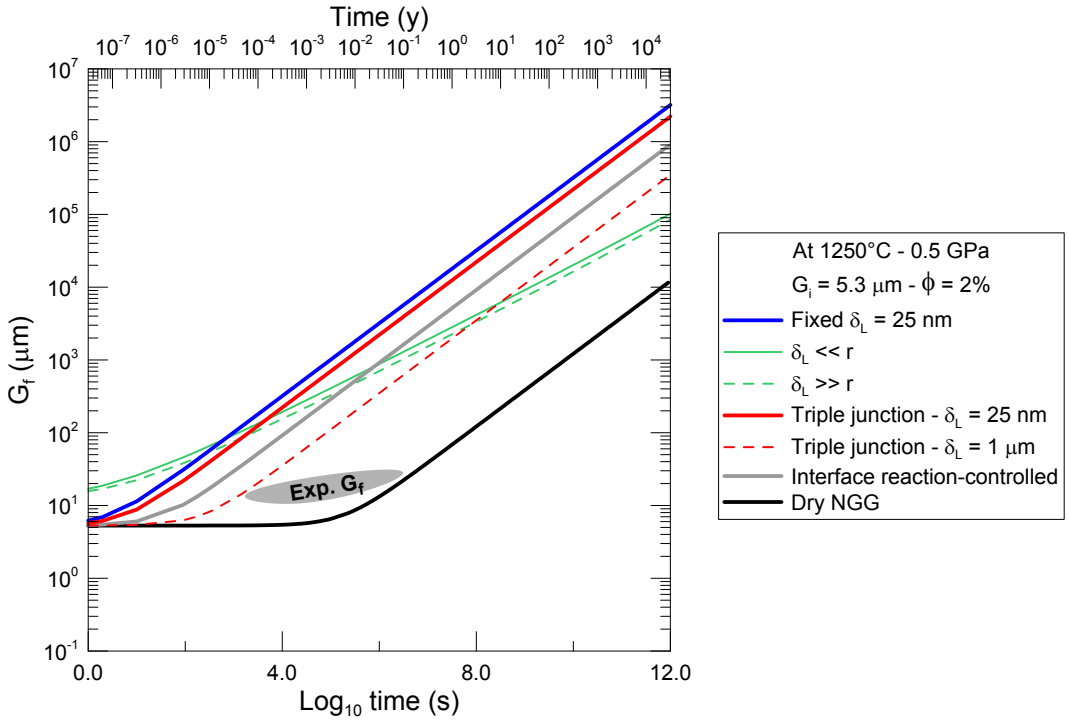

Figure 2.21 – Grain size vs. $\log_{10}$ time at a temperature of 1250 °C, a pressure of 0.5 GPa, an initial grain size of 5.3 µm and a melt fraction of 0.02. The gray zone corresponds to measured experimental grain size from this study at the same $T/P/G_i/\Phi$ conditions. The blue line corresponds to the integrated form of Eq. (2.10) with $\delta_l = 25\,nm$. Green lines correspond to melt films surrounding the grains with $\delta_l \propto \Phi$. Red lines correspond to melt residing in triple junctions and melt layers of $\delta_l = 25$ and 1000 nm. The gray line represents interface reaction-controlled grain growth. The black line corresponds to dry NGG as determined in Chapter 1.

2.4.3 Do interface reaction processes control liquid-bearing aggregate grain growths?

The dissolution constant, K_s, was constrained from the experimental studies of Brearly and Scarfe (1986), Donaldson (1990, 1985), Thornber and Huebner (1985), Zhang et al. (1989) (database in the review of Edwards and Russell (1996)), which has an Arrhenius form of:

$$K_s = K_{s,0} \exp\left(-\frac{\Delta H_a + P\Delta V}{RT}\right) \tag{2.31}$$

with $K_{s,0} = 4.14 \cdot 10^6\,\mathrm{m\,s^{-1}}$, $\Delta H_a = 446.63\,\mathrm{kJ\,mol^{-1}}$ and $\Delta V = 1.78\,\mathrm{cm^3\,mol^{-1}}$. Grain growth is therefore presented in Fig. 2.21 (gray line) and shows that interface reaction-controlled grain growth through the dissolution parameter does not fit the experimental grain sizes. It is generally assumed that the kinetics of dissolution is the same as that of precipitation, which has not yet been justified to our knowledge.

We have noted previously that experimental grain growth kinetics for liquid-bearing aggregates are the same, whether the liquid is a melt or a fluid phase (Fig. 2.19). Grain growth hardly seems to be constrained by liquid transport properties but rather by interface reaction-controlled processes. As a consequence, we have used the interface reaction-controlled grain growth equation to derive a thermally-activated precipitation law from the experimental grain sizes measured in this study. Therefore, the total grain growth law is assumed to be:

$$\begin{aligned} \left.\frac{dr}{dt}\right|_{total} &= \left.\frac{dr}{dt}\right|_{dry\,NGG} + \left.\frac{dr}{dt}\right|_{Int.\,react.} \\ r_f^2 - r_i^2 &= 2\,\frac{\alpha^* \cdot \Omega \cdot t}{RT}\left[\left(1-\Phi^{0.22}\right)\frac{\gamma_{gb}\cdot D_{gb}^{Si}}{\delta_{gb}\cdot\xi} + \Phi^{0.22}\,\frac{128}{81}\,K_p \cdot C_l\right] \end{aligned} \tag{2.32}$$

with K_p the precipitation constant (in $\mathrm{m\,s^{-1}}$).

The precipitation constant thus follows an Arrhenius law of the form:

$$K_p = K_{p,0} \exp\left(-\frac{\Delta H_a + P\Delta V}{RT}\right). \tag{2.33}$$

Based on our grain size measurements, we obtain $K_{p,0} = 7.74 \cdot 10^{-9}\,\mathrm{m\,s^{-1}}$, $\Delta H_a = 213.68\,\mathrm{kJ\,mol^{-1}}$ and $\Delta V = 18.99\,\mathrm{cm^3\,mol^{-1}}$.

Consequently, grain growth of olivine aggregates is indeed accomplished by liquid-free grain boundary migration, modeled by dry NGG, and precipitation reactions on the crystal surface, which are both combined through the contiguity, Ψ, and wetness, φ, parameters as defined in Eq. (2.32). We have therefore plotted the expected grain sizes as a function of absolute reciprocal temperature in Fig. 2.22 at P = 1 GPa, t = 360 h and $G_i = 1\,\mu\mathrm{m}$ for liquid contents ranging from 0 to 100 wt. %. This figure indicates that for liquid-bearing aggregates with $\Phi > 1$ wt. %, no substantial difference in the resulting grain sizes is observed whereas grain growth rates are significantly influenced by very low melt contents, i.e. $\Phi = 1$ wt. % vs. dry NGG. We therefore anticipate that grain sizes in an upper mantle containing very low liquid contents (i.e. melts or fluids) will therefore be markedly different from a liquid-free mantle.

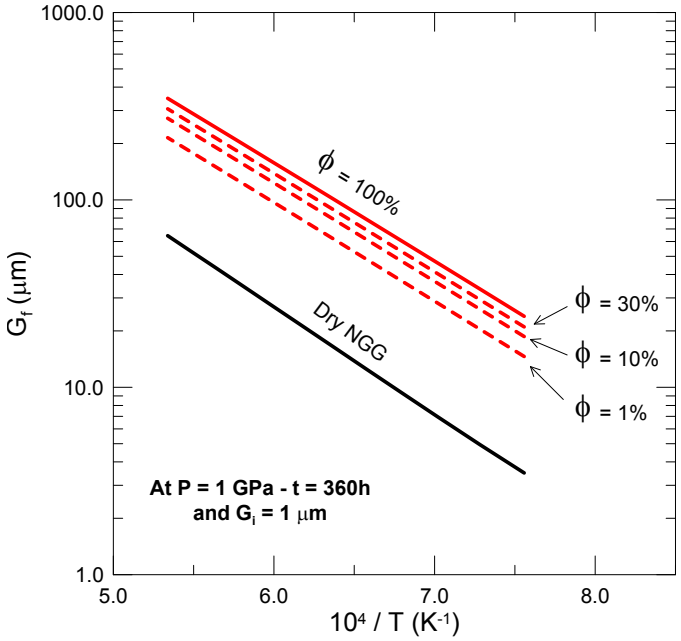

Figure 2.22 – Grain size vs. absolute reciprocal temperature with liquid contents ranging from $\Phi = 0$ to 100 wt. % at P = 1 GPa, t = 360 h and $G_i = 1\,\mu$m.

2.5 Conclusion

We have performed natural olivine grain growth experiments in a piston cylinder apparatus in order to determine the physical processes that control grain growth rates. The aggregates used in this study displayed the presence of melt, in particular the nominally melt-free samples, except for one sample which was synthetically derived. We have shown that grain growth rates for liquid-bearing aggregates are faster than for dry melt-free olivine samples, whether the samples contained a melt or fluid phase. Our experimental results are in good agreement with previously published liquid-bearing aggregates, and display similar grain growth rate scattering. We suggest that such growth rate scattering is due to a combined effect of liquid-free grain boundary migration and interstitial liquid-controlled boundary migration through the physical parameters known as contiguity, Ψ, and wetness, φ. The theory for liquid diffusion-limited controlled grain growth appears to be inconclusive, therefore setting aside the physical properties of the liquid medium as a key parameter for grain growth. Grain growth for liquid-bearing aggregates thus occurs through interface reaction processes, which is corroborated by similar grain growth rates for melt- and fluid-bearing aggregates. We have therefore used our grain size measurements to determine the rate-limiting factor for liquid-bearing aggregates, which we have defined as the precipitation rate constant, K_p. The resulting law allows grain growth to be calculated under a wide range of liquid fraction, namely from 0 to 100 wt. % liquid.

Chapitre 3

Résistivité électrique, fusion crustale et localisation de la déformation sous la chaîne Himalayo-Tibétaine

Les collisions continentales, une des conséquences directes de la tectonique des plaques, permettent de former des chaînes de montagne où de nombreux phénomènes de grande échelle se produisent, tels que l'épaississement crustal, la déformation à l'échelle régionale, du métamorphisme de haut grade... Les études de terrain sur d'anciennes chaînes orogéniques montrent que ce sont des températures élevées qui provoquent de la fusion partielle et de l'adoucissement, affectant ainsi la rhéologie de la croûte continentale en jouant principalement sur son mode de déformation, ce qui influence grandement le développement de ces longues chaînes orogéniques. Le système Himalayo-Tibétain est une chaîne de collision, encore active aujourd'hui, qui nous permet d'étudier sa structure tridimensionnelle thermo-mécanique et ainsi de mieux comprendre la formation de ces orogènes continentaux. De nombreuses études de terrain, magnétotelluriques et sismiques (les projets INDEPTH, Hi-CLIMB et HIMPROBE, entre autres) ont identifié des couches peu résistives, commençant à une profondeur de 10 à 15 km pour le Sud du Tibet (10 Ω m) et de 20 à 25 km pour le Nord-Ouest Himalaya (3 Ω m), qui coïncident avec des zones de ralentissement des vitesses sismiques. Jusqu'à présent, de telles anomalies électriques ont été interprétées comme des zones très riches de fluides interconnectés : soit des fluides aqueux (Hetényi et al., 2011, Li et al., 2003, Makovsky and Klemperer, 1999), soit des liquides silicatés (Arora et al., 2007, Brown et al., 1996, Caldwell et al., 2009, Gaillard et al., 2004, Hetényi et al., 2011, Li et al., 2003, Nábělek et al., 2009).

Malgré de nombreuses études de terrain et de modélisation numérique sur la chaîne Himalayo-Tibétaine, l'identification et la quantification de fusion hydratée de la croûte ainsi que son impact potentiel sur l'adoucissement crustal ne sont toujours pas bien établies par les études expérimentales appropriées. En effet, des mesures de résistivité électrique en laboratoire ont seulement été réalisées sur des granulites sèches à des pressions atmosphériques (Roberts and Tyburczy, 1999, Schilling and Partzsch, 2001) ; la fusion partielle ne commençant, dans ces conditions, qu'à des températures supérieures à 1000 °C, ce qui est bien plus important que les températures crustales attendues dans un contexte de collision continentale-continentale. Les liquides silicatés produits lors de la fusion crustale étant hydratés (Scaillet et al., 1995), les températures de fusion sont donc moins importantes et les résistivités électriques des roches et des liquides silicatés sont ainsi plus faibles (Gaillard et al., 2004). Par conséquent, dans notre étude expérimentale, nous avons mesuré la résistivité électrique en fonction de la température et nous avons déterminé la viscosité de métapélites partiellement fondues à 800 °C. En utilisant ce type de roche, nous avons donc pu simuler le processus géologique approprié selon des études pétrologiques précédemment publiées sur la chaîne Himalayo-Tibétaine (Law et al., 2004, Patiño Douce and Harris, 1998, Scaillet et al., 1995, Searle et al., 2006).

Ces expériences en laboratoire ont été réalisées grâce un appareil de déformation à confinement gazeux (presse Paterson), couplé à un spectromètre d'impédance, sur des échantillons métapélitiques naturels contenant de la muscovite et environ 2 poids % de H_2O. Les mesures électriques montrent qu'avec l'augmentation de la température, la résistivité électrique diminue considérablement de 1830 Ω m à 550 °C à 8 Ω m à 850 °C. Des analyses d'images et chimiques ont été réalisées sur les échantillons post-mortem et indiquent 23 vol. % de liquide silicaté hydraté produit, de composition leucogranitique. Nos mesures électriques prouvent ainsi que les données géophysiques mesurées sur le terrain révèlent environ 25 vol. % de fusion partielle à des températures de 750 à 800 °C et une profondeur entre 18 à 24 km sous le Sud du Tibet (10 Ω m) et des corps magmatiques leucogranitiques sans cristaux à 800 °C et une profondeur de 12 km sous le Nord-Ouest Himalayen (3 Ω m).

La présence de fusion partielle et de corps magmatique sans cristaux a des répercussions notables sur le comportement rhéologique de la croûte moyenne. Nos mesures de viscosité montre que 25 vol. % de fusion partielle réduit la viscosité, η, à $10^{11.5}$ Pa s tandis que des corps composés entièrement de liquide silicaté réduit η de façon plus drastique, à 10^4 Pa s. Ces valeurs de viscosité sont plusieurs ordres de grandeur inférieurs que celles précédemment estimées par les modèles thermo-mécaniques d'écoulement dans le canal de subduction et d'extrusion ductile (η = 10^{18} à 10^{19} Pa s). Grâce aux nombreuses contraintes pétrologique, géophysique et rhéologique de notre étude, ces résultats quantitatifs constituent ainsi une référence d'envergure pour les modèles conceptuels sur le développement et le maintien d'une chaîne orogénique résultant d'une collision continentale-continentale.

Earth and Planetary Science Letters 373 (2013) 20–30

Contents lists available at SciVerse ScienceDirect

Earth and Planetary Science Letters

journal homepage: www.elsevier.com/locate/epsl

Experimental assessment of the relationships between electrical resistivity, crustal melting and strain localization beneath the Himalayan–Tibetan Belt

Leïla Hashim [a,b,c,*], Fabrice Gaillard [a,b,c], Rémi Champallier [a,b,c], Nicole Le Breton [a,b,c], Laurent Arbaret [a,b,c], Bruno Scaillet [a,b,c]

[a] Université d'Orléans, ISTO, UMR 7327, 45071 Orléans, France
[b] CNRS/INSU, ISTO, UMR 7327, 45071 Orléans, France
[c] BRGM, ISTO, UMR 7327, BP 36009, 45060 Orléans, France

ARTICLE INFO

Article history:
Received 9 October 2012
Received in revised form
18 April 2013
Accepted 19 April 2013
Editor: T.M. Harrison

Keywords:
electrical resistivity
viscosity
partial melting

ABSTRACT

Seismic and magnetotelluric field campaigns carried out across the Himalaya and the Tibetan Plateau show mid-crustal low resistivity and low velocity zones. Interpretation of these anomalous observations, either saline fluids or partial melts, is still largely debated partly because experimental data simulating crustal melting under relevant pressure, temperature and water content conditions have not been provided. We report laboratory measurements constraining the resistivity as a function of temperature and the viscosity at 800 °C of natural metapelite during partial melting. Dehydration-melting of muscovite is simulated using a Paterson press at 300 MPa in the temperature range 600–850 °C. Electrical resistivity has been measured from the solid state (< 650 °C) to 25 vol% of partial melt (> 800 °C) and viscosity has been determined at 800 °C. Our results together with recent experimental constraints on seismic properties of partially molten rocks strongly suggest that the electrical and seismic anomalies measured underneath the Himalayan–Tibetan collisional orogen are best explained by partially molten rocks or local accumulation of pure melt bodies. This is also remarkably corroborated by the temperature–depth conditions of crustal partial melting and melt ponding expected from petrological surveys in the Himalayan range. However, our data suggest much higher melt fraction than previously thought and this implies regions in the middle crust having viscosities several orders of magnitude lower than previously assumed. High degree partial melting in the middle crust of the Himalayan–Tibetan orogenic system suggests revision of conceptual models on the development of mountain belts or that geophysical models addressing electrical resistivity at depth must be re-evaluated.

1. Introduction

The construction of mountain belts resulting from continental collisions involves crustal thickening, regional deformation and high-grade metamorphism. As observed in many ancient orogenic terrains, elevated temperatures locally induce melting and strain weakening, which may profoundly affect the rheology of the continental crust, its deformation regime and hence the development of these orogens (Jamieson et al., 2011; Sawyer et al., 2011).

The Himalaya–Tibetan system is an active collisional belt allowing us to probe the three-dimensional thermo-mechanical distribution of an archetypal continent–continent orogen. The Himalaya–Tibetan orogenic system was initiated 70–50 My ago by the Indo-Asian collision resulting in crustal thickening and uplifting of the Tibetan Plateau (Royden et al., 2008; Yin and Harrison, 2000). This vast plateau is separated from the Himalayan mountains by the Indus–Tsangpo suture. Two major faults are located south of this suture: the Main Central Thrust (MCT), which is a low angle high strain crustal shear zone, and the South Tibetan Detachment system (STDs), a low angle normal fault (Fig. 1). The MCT and the STDs bound the Greater Himalayan Sequence (GHS), composed of medium to high-grade metamorphic rocks, migmatites (i.e. once partially molten rocks) and kilometer-thick leucogranites pods (Law et al., 2004; Searle et al., 2006). These High Himalayan Leucogranites (HHL, Fig. 1), late Oligocene to Miocene in age (25–13 Ma), have been shown to be products of partial melting (750–800 °C) of underlying metapelites (Law et al., 2004; Patiño Douce and Harris, 1998; Scaillet et al., 1995; Searle et al., 2006). However, north of the Indus–Tsangpo suture young

* Correspondence to: Institut des Sciences de la Terre d'Orléans, UMR 7327, CNRS/Université d'Orléans, 1A, Rue de la Ferollerie, 45071 Orléans Cedex 2, France. Tel.: +33 2 38 25 53 94; fax: +33 2 38 63 64 88.
E-mail address: leila.hashim@univ-orleans.fr (L. Hashim).

0012-821X/$ - see front matter © 2013 Elsevier B.V. All rights reserved.
http://dx.doi.org/10.1016/j.epsl.2013.04.026

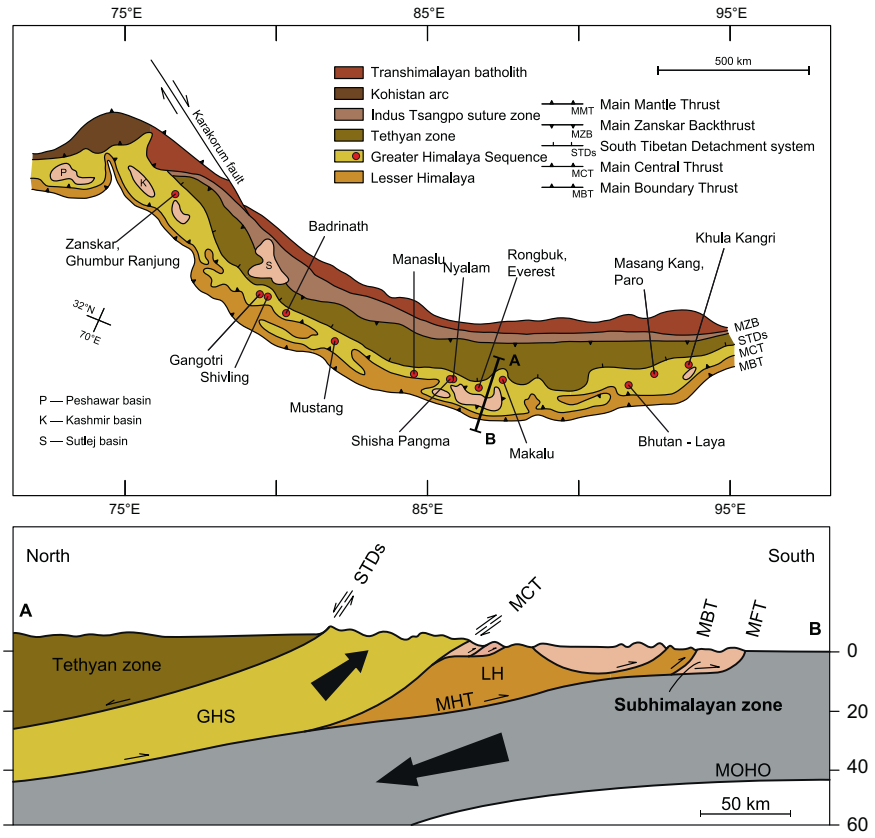

Fig. 1. Simplified geological map and cross-section of the Himalaya showing the main High Himalayan Leucogranites (red dots) along the Greater Himalaya Sequence (adapted after Law et al. (2004) and Searle et al. (2006)). Abbreviations—GHS: Greater Himalaya Sequence; LH: Lesser Himalaya; STDs: South Tibetan Detachment system; MCT: Main Central Thrust; MBT: Main Boundary Thrust; MFT: Main Frontal Thrust; MHT: Main Himalayan Thrust; MOHO: Mohorovic discontinuity. (For interpretation of the references to colour in this figure legend, the reader is referred to the web version of this article.)

granitoids (<15 Ma) are typically biotite granodiorites with ^{3}He anomalies indicating a mantle contribution (Harrison, 2006; Hoke et al., 2000; Yokoyama et al., 1999).

Several magnetotelluric (MT) and seismic field campaigns (INDEPTH, Hi-CLIMB and HIMPROBE projects) have identified low resistivity layers with well-constrained tops at a depth of 10–15 km in southern Tibet (3 Ωm) and 20–25 km in northwestern Himalaya (10 Ωm), coincident with low seismic velocity zones (Arora et al., 2007; Brown et al., 1996; Caldwell et al., 2009; Hetényi et al., 2011; Li et al., 2003; Makovsky and Klemperer, 1999; Nábělek et al., 2009; Nelson et al., 1996; Unsworth et al., 2005; Wei et al., 2001; Zhao et al., 1993). Such electrical anomalies have been interpreted as evidence of high fluid concentrations and two main hypotheses are still largely debated today: either aqueous fluids (Hetényi et al., 2011; Li et al., 2003; Makovsky and Klemperer, 1999) or melts (Arora et al., 2007; Brown et al., 1996; Caldwell et al., 2009; Gaillard et al., 2004; Li et al., 2003; Nábělek et al., 2009; Nelson et al., 1996; Unsworth et al., 2005; Wei et al., 2001). However, both hypotheses remain poorly demonstrated (Harrison, 2006; Hetényi et al., 2011), each having considerable impact on the thermal structure of the thickened crust in the Himalayas. The melt hypothesis suggests low melt percentages, between 2 and 14 vol%, from electrical constraints (Arora et al., 2007; Unsworth et al., 2005), which would be in agreement with seismic observations (Caldwell et al., 2009) (less than 10 vol% for $V_S = 2.9$–3.3 km s^{-1}). Recent experimental shear wave velocity measurements (Caricchi et al., 2008), however, indicate that such velocities better match 20–25 vol% partial melting. Experimental studies on the electrical resistivity of partially molten rocks have been carried out on dry granulite samples at atmospheric pressures (Roberts and Tyburczy, 1999; Schilling and Partzsch, 2001). Under these conditions, partial melting starts at temperatures higher than 1000 °C, which is well above expected crustal temperatures in continent-collisional settings. Melts produced by crustal melting are hydrous (Scaillet et al., 1995), which implies lower melting temperatures and lower electrical resistivity of rocks and melts (Gaillard et al., 2004). Notwithstanding, resistivity values on hydrous partially molten metapelites are still not well constrained from electrical modelling such as SIGMELTS (Pommier and Le Trong, 2011).

In this experimental study, we have performed electrical resistivity measurements as a function of temperature and determined the viscosity of metapelites undergoing partial melting at 800 °C. These experiments were conducted using a Paterson-type deformation apparatus on partially molten metapelites. By using these types of rocks in this study, we have simulated the appropriate geological processes happening at depth according to previous petrological studies in the Himalayan–Tibetan range (Law et al., 2004; Patiño Douce and Harris, 1998; Scaillet et al., 1995; Searle et al., 2006). We therefore show here that the geophysical anomalies underneath this orogenic system must pinpoint high degree crustal melting and local melt accumulation, forming low-viscous regions, which are several orders of magnitude weaker than previously assumed (Beaumont et al., 2001,

2004, 2006; Jamieson et al., 2004; Medvedev and Beaumont, 2006). These results suggest revision of conceptual models on the development of mountain belts.

2. Materials and methods

2.1. Starting material

The starting material is a natural metapelitic rock from the Sioule metamorphic series (two-micas paragneiss formation, Supplementary Fig. 1), which belongs to the central metamorphic domain of the European Hercynian Belt (Faure et al., 2002). The Hercynian chain resulted from the collision of Gondwana and Laurussia in the Late Devonian–Early Carboniferous. The Sioule metamorphic series show strong evidence of partial melting and leucogranite emplacements similar to the Himalayan systems (Faure et al., 2002).

The composition of the Sioule sample we used (Table 1) is essentially similar to the Himalayan metapelite samples used by Patiño Douce and Harris (1998). The starting material contains Na-plagioclase, muscovite, biotite, quartz and K-feldspar in order of abundances (Table 1). Its composition and texture indicate no involvement in partial melting events and did not suffer any associated chemical depletions (in alkalis and water). Small amount of graphite (<0.5 vol%) has been observed in thin sections. The bulk composition, i.e. major elements and water content, was obtained from electron microprobe (EMP) and Fourier transformed infrared (FTIR) analyses, respectively, on a glass that has been rapidly quenched after total melting of this rock at high-pressure high-temperature (4 kb, 1170 °C, 21 h). This melting experiment was conducted in an internally heated pressure vessel at Institut des Sciences de la Terre d'Orléans (ISTO) (see Iacono-Marziano et al., 2012). The total water content of the glass analysed by FTIR is 1.75 wt % and a large amount of dissolved CO_2 has been observed (1000 ppm CO_2). This CO_2 most likely derives from graphite oxidation during high temperature melting.

Oxygen fugacity of all the experiments presented in this paper was buffered by the coexistence of graphite and CO_2 in the sample (observed after the runs). This corresponds to redox conditions close to FMQ-2 and mimics natural conditions of crustal melting that also occurs at graphite saturation (Pichavant et al., 1996).

Published experiments (Patiño Douce and Harris, 1998) and our results show that the dehydration-melting of muscovite starts at 650 °C at 300 MPa. Previous experimental work established the following reaction (Patiño Douce and Harris, 1998):

$$22\ \mathrm{Ms} + 7\ \mathrm{Pl} + 8\ \mathrm{Qz} \rightarrow 25\ \mathrm{Melt} + 5\ \mathrm{Kfs} + 5\ \mathrm{Sil} + 2\ \mathrm{Bt} \qquad \text{(Reaction1)}$$

with Ms standing for muscovite, Pl for plagioclase, Qz for quartz, Kfs for K-feldspar, Sil for sillimanite and Bt for biotite.

Reaction (1) indicates that water, liberated upon muscovite breakdown, induces partial melting and incorporates into the melt, with about 1.14 volume of melt produced for 1 volume of muscovite. As our sample contains 23 vol% Ms, completion of Reaction (1) induces 26.2 vol% melt in the rock.

2.2. Electrical resistivity measurements

The conventional Paterson assembly was modified in order to measure the resistance of the samples (Fig. 2). The sample-electrode geometry is similar to the configuration used by Caricchi et al. (2011). For resistivity measurements, an inner Ni electrode was inserted in the centre of the sample (perpendicularly to the layering configuration) and an outer Pt foil was placed around the samples. The resistance of the samples was measured along their radii, between the inner Ni electrode and the outer Pt foil. The compositional difference between the two electrodes had no effect on the collected resistance values. The electrical resistivity, ρ (Ωm), was obtained from the resistance, R (Ω), using (Caricchi et al., 2011; Gaillard, 2004; Pommier et al., 2008)

$$\rho = (2\pi LR)/(\ln(d_{ext}/d_{int}) \qquad (1)$$

with L the length of the sample (m), d_{ext} the outer diameter of the sample (m) and d_{int} the diameter of the inner electrode (m).

Electrical resistivity measurements were collected solely under static conditions (i.e. without applied deformation) in the temperature range of 500–850 °C at 300 MPa and at frequencies between 1 Hz and 1 MHz. Error on the calculated resistivity values

Table 1
Chemical compositions of bulk rock and mineral phases of the Sioule metapelitic sample and chemical compositions of High Himalayan Leucogranite sample (DK, Scaillet et al., 1995) and of the produced melt in this study (Melt, sample PP214). Modal abundances were calculated by mass balance. Compositions were determined by EMP and are given in wt% (recalculated to 100 wt% volatile-free).

Starting sample							Produced melt	
Modal abundances	Bulk rock 100	Quartz 22	K-Feldspar 2	Plagioclase 30	Muscovite 23	Biotite 23	DK –	Melt –
SiO_2	62.36 (±0.26)	100.00	63.63 (±4.54)	67.25 (±1.04)	48.27 (±0.69)	36.41 (±2.02)	73.04	74.82 (±3.59)
Al_2O_3	19.27 (±0.18)	0.00	19.87 (±3.73)	20.21 (±0.57)	37.29 (±0.82)	19.73 (±1.43)	15.32	14.92 (±2.39)
Fe_2O_3	–	–	–	–	–	–	0.17	nd
FeO	4.56 (±0.22)[a]	0.00[a]	0.18 (±0.22)[a]	0.14 (±0.08)[a]	1.73 (±1.62)[a]	22.00 (±1.47)[a]	0.74	0.66 (±0.30)[a]
MnO	0.08 (±0.07)	0.00	0.01 (±0.01)	0.03 (±0.03)	0.08 (±0.02)	0.32 (±0.03)	0.01	nd
MgO	3.28 (±0.03)	0.00	0.04 (±0.15)	0.01 (±0.03)	0.74 (±0.08)	9.14 (±0.47)	0.20	0.13 (±0.05)
CaO	1.06 (±0.07)	0.00	0.03 (±0.07)	0.88 (±0.47)	0.00 (±0.00)	0.08 (±0.16)	0.85	0.70 (±0.63)
Na_2O	2.63 (±0.02)	0.00	1.21 (±1.66)	9.62 (±2.19)	0.49 (±0.05)	0.12 (±0.05)	3.85	2.65 (±1.15)
K_2O	5.33 (±0.09)	0.00	15.00 (±2.38)	1.84 (±3.66)	10.77 (±0.18)	9.92 (±0.93)	4.96	5.92 (±1.68)
TiO_2	1.23 (±0.05)	0.00	0.03 (±0.13)	0.02 (±0.02)	0.63 (±0.03)	2.28 (±0.43)	0.13	0.06 (±0.04)
P_2O_5	nd	nd	nd	nd	nd	nd	0.14	nd
CO_2	0.001[b]	nd	nd	nd	nd	nd	0.05	nd
H_2O	1.75[b]	nd	nd	nd	nd	nd	0.65[c]	nd
F	0.19 (±0.02)	nd	nd	nd	nd	nd	0.09	0.14 (±0.02)
Cl	0.01 (±0.01)	nd	nd	nd	nd	nd	nd	nd
Total	96.09 (±0.30)	100.00	97.97 (±1.75)	98.37 (±0.64)	93.52 (±1.80)	91.99 (±6.12)	100.20	92.49 (±1.39)

nd: not determined.

[a] FeO as total Fe (Fe_2O_3+FeO).
[b] H_2O and CO_2 were determined by FTIR.
[c] Water phase determined in bulk DK. Melt contains on average 6 wt% H_2O.

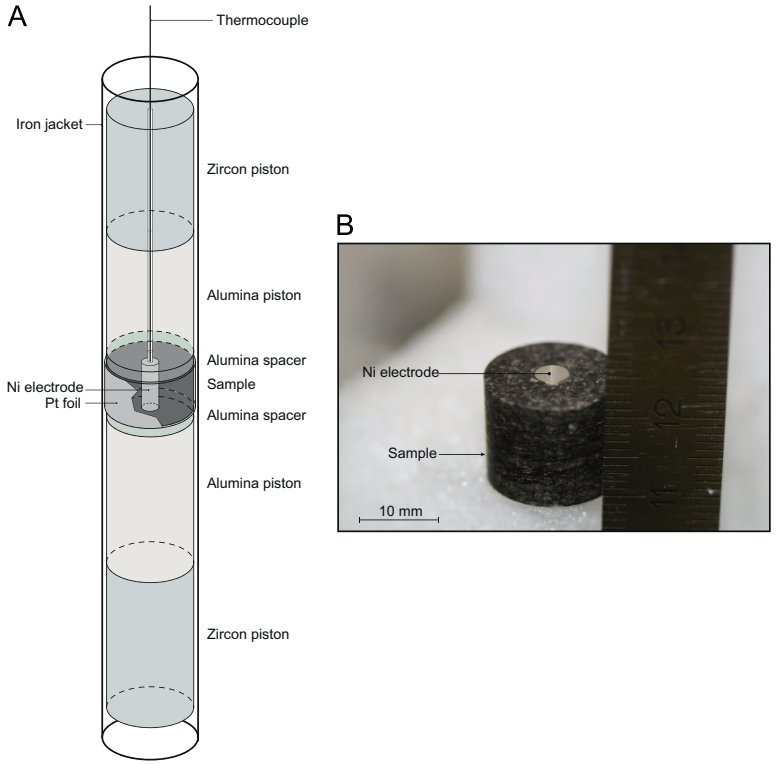

Fig. 2. (A) Modified Paterson assembly used for electrical resistivity measurements. (B) Zoom of sample showing inner Ni electrode.

is estimated to be less than 7% except for run PP216 where the maximum error is of about 28% for temperatures <690 °C (Table 2). These estimations are based on the geometrical constraints of the samples (width, length, and inner diameter) and on repeated electrical measurements at the same experimental conditions.

The electrical response of the samples is plotted at each frequency in the Nyquist plane ($-Z'$, Z'') since the complex impedance (Z) can be written as the sum of real (Z') and imaginary (Z'') components (where $Z=Z'+jZ''$ and $j^2=-1$). In this plane, the electrical response is an arc centred on the real axis where the first part of this arc (high frequencies) represents the electrical response of the sample whereas the second low-frequency arc is related to the sample/electrode interactions (Huebner and Dillenburg, 1995; Supplementary Fig. 2). The impedance arcs from this study can be fitted by a parallel circuit of a resistance and a capacitance (Huebner and Dillenburg, 1995; Roberts and Tyburczy, 1991).

2.3. Rheological measurements

Deformation experiments were performed at a pressure of 300 MPa and at a temperature of 800 °C. During dynamic experiments, strain rates, $\dot{\gamma}$, range from 1×10^{-5} to 2.5×10^{-4} s^{-1} and bulk finite strain, γ, reaches a maximum value of 0.91 (Table 2). Strain rates were controlled by applying a continuous torque during the experiments. Stepping strain rate experiments were also conducted in order to calculate the stress exponent, n, enabling us to calculate the stress τ (MPa) from the applied torque (Nm). Stepping strain rate consists of increasing strain rate in a stepwise manner once steady state stress conditions were achieved for a given strain rate (Paterson and Olgaard, 2000). Apparent viscosities, η_a (Pa.s), of our samples were calculated for a given strain rate by using the following equation (Paterson and Olgaard, 2000):

$$\eta_a=\tau/\dot{\gamma} \quad (2)$$

with τ the shear stress (Pa) and $\dot{\gamma}$, the strain rate (s^{-1}).

2.4. Analytical techniques and imaging

After the static and dynamic experiments, the samples were cut along longitudinal axial sections (Fig. 7 in Paterson and Olgaard (2000)) and then mounted in epoxy. A scanning electron microscope (SEM) was used for microscopic observations at backscattered electron mode at ISTO (see Supplementary Figs. 3–5). Melt distribution and volumetric percentages were determined by manually selecting the melt phase (consisting of glass and crystals formed from Reaction (1)) on SEM images of the radial faces of the samples (Supplementary Figs. 3 and 4). Binary images were created with solely the melt appearing in black. Volumetric percentages were then calculated using a ratio of pixels of melt over the total pixels of the studied binary image (Table 2).

Chemical compositions of bulk rock and mineral phases as well as the melt produced by dehydration-melting of muscovite crystals were obtained by EMP analyses. The water content (in the glass) of the bulk rock was analysed by FTIR following Iacono-Marziano et al. (2012).

3. Experimental strategy

To better constrain electrical resistivity values during our Paterson experiments, we have conducted partial melting experiments in internally heated pressure vessels at ISTO (PM experiments, Supplementary materials). These partial melting experiments have

Table 2
Experimental conditions and results. Multiple values of $\dot{\gamma}$ indicate the strain rate applied during stepping strain rate experiments. Apparent viscosities, η_A, were calculated as indicated in the text. Melt percentages were evaluated by image analysis of the SEM images after each run, within 5% error margin. Maximum error on the resistivity measurements is estimated as indicated in the text. Runs PP187 and PP202 have significantly higher melt fraction than run PP205 due to enhancement of muscovite melting rates with deformation. This was also observed in Misra et al. (2009). For all experiments $P=300$ MPa.

Run	Length (mm)	Diameter (mm)	Type	T_{peak} (°C)	$\dot{\gamma}$ (s^{-1})	γ	τ_{peak} (MPa)	η_A (log Pa.s)	Φ_M (vol%)	Phases	Total run duration (h)	Maximum error on resistivity measurements (%)
PP187	12.40	14.93	Torsion	825	1×10^{-5}	0.57	22.0	12.32	23	Qz+Pl+Kfs+Bt+Ms+Sil+Melt	24.2	7.0
PP202	16.93	14.91	Torsion	825	2.5×10^{-5}	0.35	22.0	11.93	24	Qz+Pl+Kfs+Bt+Ms+Sil+Melt	17.0	0.1
					5×10^{-5}	0.77	24.6	11.67				
					1×10^{-4}	0.91	24.6	11.38				
PP205	8.33	14.86	Static	825	–	–	–	–	10	Qz+Pl+Kfs+Bt+Ms+Sil+Melt	30.0	2.2
PP213	14.71	14.91	Torsion	850	1×10^{-5}	0.02	4.9	11.69	30	Qz+Pl+Kfs+Bt+Ms+Sil+Melt	29.6	1.3
					5×10^{-5}	0.03	6.5	11.11				
					2.5×10^{-4}	0.20	8.9	10.55				
PP214	13.23	14.99	Static	850	–	–	–	–	23	Qz+Pl+Kfs+Bt+Ms+Sil+Melt	23.6	0.1
PP216	19.65	14.98	Torsion	850	2.5×10^{-4}	0.23	9.2	10.56	30	Qz+Pl+Kfs+Bt+Ms+Sil+Melt	7.6	28.2

Abbreviations—T_{peak}: peak temperature undergone by the sample; $\dot{\gamma}$: shear strain rate; γ: finite shear strain; τ_{peak}: peak stress; η_A: apparent viscosity; Φ_m: melt percentage; Qz: quartz; Pl: plagioclase; Kfs: K-feldspar; Bt: biotite; Ms: muscovite; Sil: aluminous phase (sillimanite after Patiño Douce and Harris (1998)).

enabled us to constrain the onset of partial melting in the temperature range 650–700 °C (Supplementary Table 1; Supplementary Fig. 5), which is in agreement with published phase equilibria experiments on similar mineralogical assemblages (Patiño Douce and Harris, 1998). In the latter study, the associated melt production, via Reaction (1), is completed at $T=820$ °C.

Partial melting of metapelites has also been shown to be an extremely slow process. Previous studies reveal that run durations of 1 week are not sufficient to achieve equilibrium melt percentages at temperatures lower than 800 °C (Rubie and Brearly, 1990). Indeed, Rubie and Brearly (1990) have shown that the melting kinetics of a reaction involving muscovite, quartz and H_2O is controlled by diffusion of Si, Al and K through the melt for temperatures <760 °C. The width of the reaction zone between muscovite and quartz is a square root function of time and is modelled by a parabolic law, which indicates that at least two weeks are required to fully dissolve small muscovite grains. Textural and crystal-melt chemical equilibrations at $T<800$ °C thus operate at rates that are not compatible with the duration of experiments in Paterson apparatus.

Our time-series resistivity measurements performed at temperatures ranging from 650 to 825 °C (PP187, PP202, PP205; Table 2) did not show any clear electrical stabilization. We have interpreted this behaviour as a record of slow chemical and textural evolution of the samples during partial melting (Supplementary Fig. 6). To counteract this effect and obtain chemical and textural equilibrium, the temperature was increased to 850 °C (PP213, PP214, PP216; Table 2), enhancing reaction kinetics and leading to nearly electrical steady state within ~300 min (Supplementary Fig. 7). Such high temperature ensured the rapid and total melting of muscovite. For the reason explained below (see Section 5.1), the results used in this study for interpreting MT anomalies beneath the Tibetan–Himalayan range are essentially based on those from experiments with peak temperatures of 850 °C (PP213, PP214 and PP216; Table 2). During these experiments, we linearly increased the temperature to 500 °C and then increased by 50 °C steps up to 850 °C, enabling us to perform resistivity measurements at different constant temperatures. After annealing the samples at 850 °C, the temperature was decreased to 800 °C, which corresponds to established temperatures of melt extraction as suggested by geochemical, experimental and field observations in the Himalayas (Patiño Douce and Harris, 1998; Searle et al., 1997). Long static resistivity measurements or viscosity experiments were thus conducted separately at 800 °C after the annealing stage. Electrical resistivities were then measured during cooling cycles (Fig. 4 and Supplementary Fig. 8).

4. Results

4.1. Chemical composition of the produced melt

EMP analyses show that the melt produced during our partial melting experiments is granitic in composition and analogous to the HHL (Scaillet et al., 1995; Table 1). It has typical high SiO_2 contents (>70 wt%) and high water contents (>6 wt% based on the difference to 100%, see Table 1). This composition was analysed in run PP214 after equilibration at a peak temperature of 850 °C. Liquid compositions analysed in other experiments were relatively similar, but the low melt fraction did not allow us to obtain precise chemical analyses.

4.2. Electrical resistivity

Replicated experiments showed a good reproducibility during heating stages (Fig. 3) in spite of the variable sample geometries (length, layering configuration). As temperature increases from 550 to 825 °C, the electrical resistivity of the metapelites decreases dramatically from ~2000 to 20 Ωm. The onset of partial melting, optically identified from the PM - experiments presented in Section 3, is also indicated by a slope shift (i.e. a change in electrical properties) between 650 and 700 °C in Fig. 3.

Fig. 4 presents the resistivity measurements from experiment PP216 during both heating and cooling cycles (after a peak T at 850 °C). As illustrated in this figure, the resistivity/temperature path is shifted toward less resistive values during cooling cycles. The difference between heating and cooling cycles is significant but remains reasonably low except for temperatures <650 °C, where this discrepancy reaches at least one order of magnitude. Furthermore, between 850 and 550 °C during the cooling cycle, melt percentage remains constant at 23 vol%.

4.3. Viscosity

Image analyses (Supplementary Figs. 3 and 4) revealed no migration and accumulation of melt throughout the deformed samples. The samples deformed homogeneously since no strain localization was observed.

We have determined the stress exponent, n, of our material, corresponding to the slope of a logarithmic plot of shear strain rate versus maximum measured torque (Supplementary Fig. 9). Despite our small strain rate/torque data set, the calculated n ($n=5.44$) is in good agreement with a previous study on the rheology of

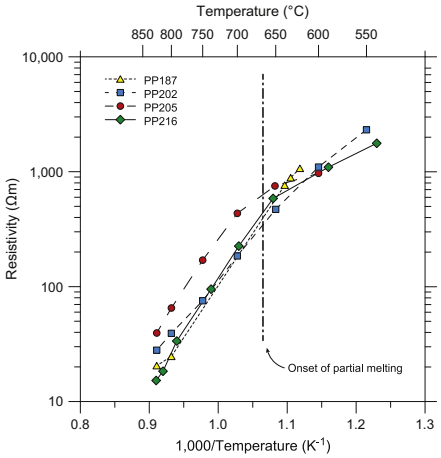

Fig. 3. Measured electrical resistivities of runs PP187, PP202, PP205 and PP216 during heating cycles at 300 MPa. The plotted values represent electrical measurements after $t > 60$ min. Error on the plotted electrical resistivity values is within the size of the data points.

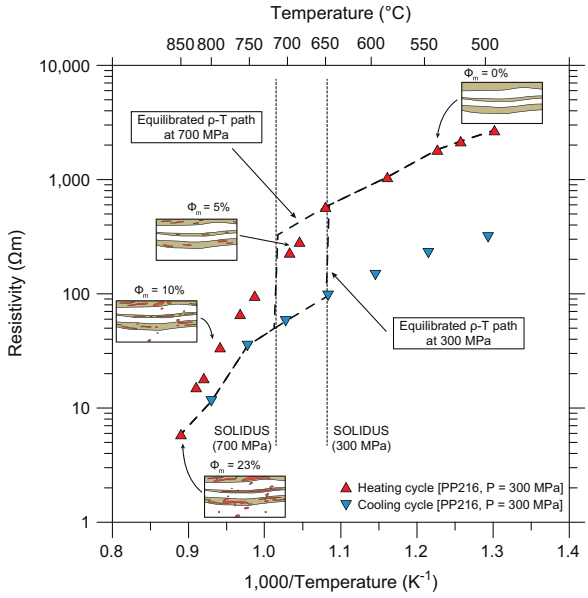

Fig. 4. Electrical resistivity versus temperature of experiment PP216 at 300 MPa confining pressure. During the heating cycle (red top-pointing triangles), melt percentage increases moderately from 0 to 23 vol%. During the cooling cycle (blue down-pointing triangles), the sample remains partially molten (23 vol% melt), even at the lowest temperature (500 °C). This hysteresis cycle shows that the sample is in electrical disequilibrium. The equilibrated resistivity/temperature path (bold dashed lines) should follow the solid-state sample until the solidus temperature (e.g. solidi at 300 and 700 MPa), where the resistivity is shifted within a few degrees Celsius to lower values corresponding to 23 vol% partial melting. See text for more details. Error on the plotted electrical resistivity values is within the size of the data points. Abbreviation—Φ_m: melt percentage; *P*: pressure. (For interpretation of the references to colour in this figure legend, the reader is referred to the web version of this article.)

synthetic metapelitic samples undergoing partial melting ($n = 5.15$; Misra et al., 2009).

The mechanical behaviour of our metapelitic samples is summarized in a shear stress versus shear strain plot (Fig. 5). These rheological measurements show a rapid linear increase, corresponding to the elastic response of the stressed sample, followed by either steady state flow or moderate weakening during plastic deformation (Fig. 5). Peak stress values vary with peak temperature: as temperature increases, melt percentage increases, thus weakening the metapelitic sample. The significant peak stress value difference between runs PP187–PP202 and runs PP213–PP216 is therefore directly related to their corresponding peak temperatures (825 °C and 850 °C, respectively). Fig. 5 and Table 2 also indicate good reproducibility for equivalent strain rates and peak temperatures (experiments PP213 and PP216 for $T_{peak} = 850$ °C and $\dot{\gamma} = 2.5 \times 10^{-4}$ s^{-1}).

Experiments PP187 and PP202 ($T_{peak} = 825$ °C and $\dot{\gamma} = 1 \times 10^{-5}$–$1 \times 10^{-4}$ s^{-1}) present calculated apparent viscosities, η_A, ranging from $10^{12.32}$ to $10^{11.38}$ Pa.s, whereas experiments PP213 and PP216 ($T_{peak} = 850$ °C and $\dot{\gamma} = 1 \times 10^{-5}$–$2.5 \times 10^{-4}$ s^{-1}) present η_A ranging from $10^{11.69}$ to $10^{10.56}$ Pa.s (Table 2).

5. Discussion

5.1. Equilibrated melt percentage/temperature/resistivity paths

At 300 MPa during heating cycles, melt percentage increases continuously from 0 vol% at 550 °C to 23 vol% at 850 °C (Fig. 4; Supplementary Table 1), indicating slow melting kinetics because melt fraction is expected to abruptly increase once muscovite breakdown temperature is exceeded. Likewise, during cooling cycles, the low resistivity/temperature paths were interpreted as slow kinetics of crystallization, as melt percentage remains at 23 vol% even at the lowest temperature (500 °C, Fig. 4). We have thus calculated the variations of equilibrium melt percentage as a function of *P* and *T* by creating a *P*–*T* pseudosection (Supplementary Fig. 10), using the collection of thermodynamic modelling programs Perple_X 6.6.6. (Connolly, 1990, 2005; Connolly and Kerrick, 1987; Connolly and Petrini, 2002). The bulk composition of the system used for calculations is that of our metapelitic sample together with 1.75 wt% water. Melt percentage is modelled by using the program PyWerami (http://petrol.natur.cuni.cz/~ondro/pywerami:home, Fig. 6). At 300 MPa, the calculated equilibrium melt percentage increases from 0 to more than 15 vol% within a few degrees as a consequence of the dehydration-melting of muscovite in fluid absent conditions. This strong and abrupt increase in melt mode is not observed during heating cycles of the present study due to a sluggish melting rate. The *P*–*T* pseudosection (Supplementary Fig. 10) indicates that above the solidus temperature ($T_S = 650$ °C at 300 MPa), the partially molten samples in our experiments are in disequilibrium, thus overestimating the electrical resistivity values. Measurements collected during the cooling cycles therefore represent a very close assessment of the resistivity of equilibrated partially molten metapelites at temperatures just above the temperature of muscovite dehydration-melting (650 °C < *T* < 700 °C at 300 MPa).

Therefore, in our experiments ($P = 300$ MPa), we considered that the equilibrated resistivity/temperature path should follow the solid-state path during the heating cycle until the solidus temperature is reached (650 °C < T_S < 700 °C). Above T_S, resistivity should be shifted within a few degrees Celsius to values corresponding to 23 vol% partial melting during the cooling cycle (bold dashed line at 300 MPa for $T > 650$ °C in Fig. 4). The equilibrated resistivity/temperature path varies with pressure, as T_S increases with increasing pressure (from 675 °C at 500 MPa to 745 °C at 900 MPa; Fig. 6). This T_S/pressure-dependence therefore shifts the abrupt decrease in electrical resistivity to higher temperatures. As an example, the equilibrated resistivity/temperature path at 700 MPa is shown to abruptly decrease by 1-log unit at $T_S = 720$ °C (Fig. 4).

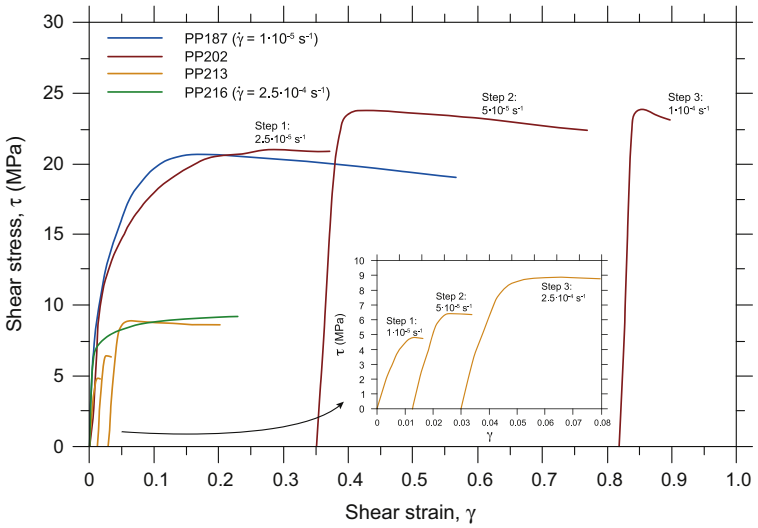

Fig. 5. Mechanical behaviour of the metapelitic samples during runs PP187, PP202, PP213 and PP216. Experiments PP187 and PP216 were deformed at constant strain rate. Stepping strain rate experiments were undertaken during runs PP202 and PP213.

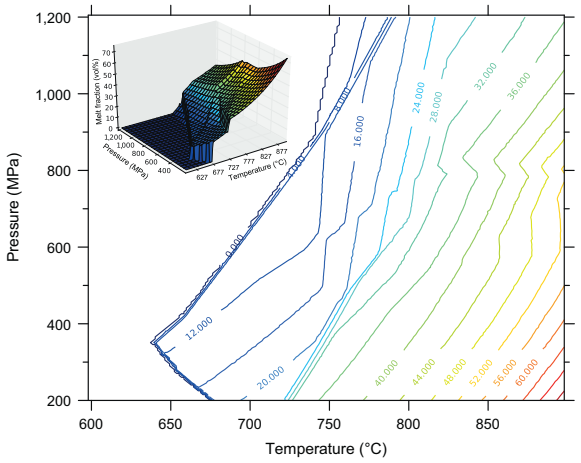

Fig. 6. Melt percentages (vol%) calculated with Perple_X 6.6.6. for the chemical composition of the Sioule sample used as starting material in the present study. The water content of the system was fixed at 1.75 wt%. The results are plotted in *P–T* diagrams (2D contours and 3D surface) with the program PyWerami.

5.2. Electrical resistivity of solid and liquid end-members

Since HHL pods are presently outcropping in the GHS (Fig. 1), we have calculated the electrical resistivity of crystal-free leucogranite magma bodies as extrapolated from our partial melting experiments. Electrical resistivity is commonly estimated by using mixing models where the bulk resistivity of the sample depends on the electrical resistivities of the present phases (in this study, melt and solid), as well as their relative volumes and geometrical distributions in the sample.

We were able to extrapolate the electrical resistivity of the produced melt by using our experimental and previously published data and mixing models (Table 3; Gaillard and Marziano, 2005; Yoshino et al., 2012). For brevity, only a few mixing models were used in this section: Archie's law, which is an empirically derived relation (Archie, 1942); the modified Archie's law, which is derived from Archie's law using geometrical constraints (Glover et al., 2000); Hashin–Shtrikman upper bound (Hashin and Shtrikman, 1962); the cubes model (Waff, 1974) and the tubes model (Grant and West, 1965; Schmeling, 1986).

Table 3
Melt resistivity extrapolated using mixing models. Parameters used in the mixing models—resistivity of the solid: $\rho_S = 163.24\ \Omega$m; bulk resistivity: $\rho_B = 11.97\ \Omega$m; melt fraction: $\chi_M = 0.23$; Archie's constant: $C = 0.73$ (Roberts and Tyburczy, 1999); Archie's cementation exponent: $m = 1.05$ (Gaillard and Marziano, 2005).

Electrical mixing law	Melt resistivity (Ωm)
Archie's law	1.87
Modified Archie's law	2.71
Hashin–Shtrikman upper bound	2.13
Cubes model	1.91
Tubes model	0.97

The electrical resistivity of the solid was adjusted from the low temperature data ($< 650\ ^\circ$C) collected during our experiments as follows:

$$\ln\rho_s = -\ln\rho_0 + (-E_a/(RT))$$

with

$$\rho_0 = 2.90 \pm 0.20 \text{ and } E_a/R = -8581.80 \pm 600.73 \quad (3)$$

where ρ_S is the resistivity of the solid rock in Ωm; ρ_0, the pre-exponential term in Ωm; E_a, the activation energy in J; R, the gas constant; and T, the temperature in K.

The graphite in our sample shows no noticeable effect on the electrical resistivity of our solid-state samples during heating stages (Fig. 4). Indeed, measured resistivities are typical of solid-state crustal rocks (Ferri et al., 2013; Schilling and Partzsch, 2001), whereas interconnected graphite in our sample should decrease resistivities by several orders of magnitude (Shankland et al., 1993; Yoshino and Noritake, 2011). This experimental observation on natural metapelite is in agreement with previous experimental studies performed on graphite-rich xenoliths (Ferri et al., 2013) and C-rich synthetic quartz aggregates (Yoshino and Noritake, 2011).

We used the bulk resistivity value collected at 800 °C during the cooling cycle, once the samples presented an electrical steady state

(ρ_B = 11.97 Ωm) to calculate the resistivity of the melt. Image analyses showed that this sample contained 23 vol % partial melting.

Calculations show that melt resistivities are essentially similar for Archie's law, the Hashin–Shtrikman upper bound and the cubes model (between 1.87 and 2.13 Ωm, Table 3). Melt resistivity values calculated using the tube model and the modified Archie's law are however slightly lower and higher, respectively (0.97 and 2.71 Ωm, Table 3). Electrical resistivity of hydrated granitic melts was also calculated following equations by Gaillard (2004):

$$\rho = (\sigma_0 \exp(-E_a/(RT))^{-1} \quad (4)$$

with

$$\sigma_0 = -78.9\ln(H_2O) + 754 \text{ and } E_a = -2925\ln(H_2O) + 70,132$$

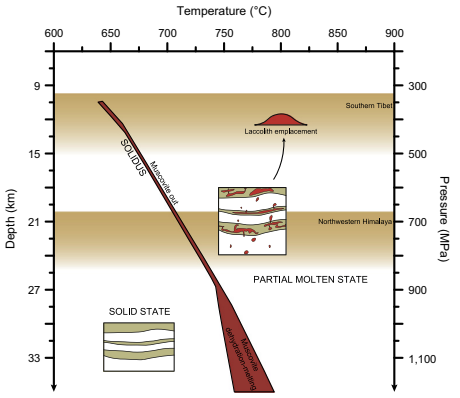

Fig. 7. Pressure/depth versus temperature plot for partial melting of Himalayan metapelites. The red zone represents the dehydration-melting of muscovite in fluid absent conditions and isolates solid-state rocks (on the left-hand side of the red zone) from partially molten rocks (on the right-hand side of the red zone). In the Himalayan geological context, metapelites produce granitic melts in the temperature range 750–800 °C and pressures between 600 and 800 MPa (Patiño Douce and Harris, 1998). HHL emplace as near-liquidus magma at 800 °C and 400 MPa (Scaillet et al., 1995). Resistivity–depth–temperature conditions for Himalayan partial melting and leucogranite emplacement remarkably match the MT anomalies beneath this orogen. (For interpretation of the references to colour in this figure legend, the reader is referred to the web version of this article.)

where T is the temperature in K and H_2O the water content in wt% (natural logarithm). For granitic liquids containing 6 wt% of dissolved H_2O at 800 °C, Eq. (4) yields 2.35 Ωm, which is in remarkable agreement with the liquid resistivity independently estimated from partial melting experiments and mixing models.

5.3. Cross-checking petrological, geophysical and laboratory constraints

Laboratory work and thermobarometric studies (Patiño Douce and Harris, 1998) indicate that melting of the Himalayan metapelites occurred at a pressure equivalent to 18–24 km depth and a temperature of 750–800 °C (Fig. 7), which according to our experimental data correspond to a resistivity of 10 Ωm (Fig. 8). As shown in Fig. 7, such resistivity–depth–temperature conditions are fully compatible with the northwestern Himalayan electrical anomaly. Furthermore, the high melt percentage deduced from our study yields the appropriate shear wave velocities observed in this region (Caldwell et al., 2009; Caricchi et al., 2008).

Electrical resistivity was calculated during cooling and crystallization of leucogranites (Fig. 8; Scaillet et al., 1995). Due to the near-eutectic composition of such magmas, the resistivity moderately increases to ~15 Ωm as temperature decreases to 650 °C (i.e. 30 vol% crystals), whereas in the temperature range 650–645 °C, where the bulk crystallization occurs, the resistivity increases by several orders of magnitude (Fig. 8). Experimental studies show that HHL were emplaced as near-liquidus magma with a depth of ~12 km and a temperature of about 800 °C (Fig. 7; Scaillet et al., 1995), which yields a resistivity of 3 Ωm (Fig. 8). Such resistivity–depth–temperature conditions remarkably match the electrical anomaly detected beneath Southern Tibet (Fig. 7). Since shear waves do not propagate through liquid states, we suggest that spatial resolution of seismic analyses may not allow identification of fully molten bodies of limited vertical extents, such as sill-shaped or laccolith bodies.

Magnetotelluric profiles enable us to constrain the depth of the top of the electrical anomaly but can hardly constrain their thicknesses. We have based our experimental modelling exclusively on peak resistivity values from MT data of northwestern Himalaya and southern Tibet (10 and 3 Ωm, respectively; Arora

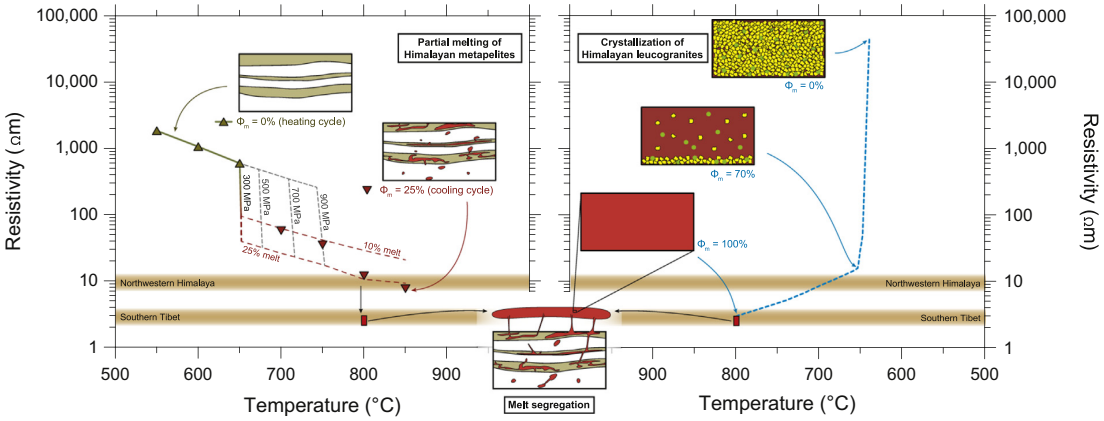

Fig. 8. Electrical resistivity versus temperature for partial melting of Himalayan metapelites and crystallization of Himalayan leucogranites. Our experimental data are represented by the triangles in the left panel. At 650 °C and 300 MPa, melt percentage increases from 0 to 10 vol% within 5 °C, sharply decreasing the electrical resistivity. With increasing pressure, melting temperature increases, therefore shifting the sharp decrease in resistivity to higher temperatures. Resistivity mixing models are shown in red dashed lines, considering fully connected melt (10 and 25 vol% melt) in a solid matrix (HS^+). Extrapolation of fully molten bodies at 800 °C from our partial melting experiments and mixing models is represented by red rectangles in both panels (lower and upper boundaries calculated using HS^+ and Eq. (5) by Gaillard (2004), respectively). The blue dotted line in the right panel corresponds to cooling and crystallization of leucogranitic bodies (experimental data from Scaillet et al. (1995) using HS^+). MT anomalies can be explained by either 25 vol% partial melting of the middle crust at 800 °C or leucogranites containing 20 vol% crystals at 680 °C for northwestern Himalaya and by emplacement of leucogranitic bodies at 800 °C for southern Tibet. Abbreviation—Φ_m: melt percentage. (For interpretation of the references to colour in this figure legend, the reader is referred to the web version of this article.)

et al., 2007; Unsworth et al., 2005). The resistivity values implied in this study yield anomaly thicknesses of about 23 km for northwestern Himalaya and 12 km for southern Tibet (Supplementary Fig. 11). There is however a tradeoff between the thickness of a low resistivity layer and the value of resistivity of that layer. We decided to adopt the values given in Arora et al. (2007) and Unsworth et al. (2005) therefore knowingly ignoring this tradeoff. We suggest that a more realistic MT-modelling should be carried out by using our experimental electrical results, complemented by seismic data, but such considerations go beyond the scope of the present work.

5.4. Viscosity implications

Presence of partial melting and fully molten bodies has serious impact on the rheological behaviour of the middle crust. Indeed, our results show that crustal rocks with 20–25 vol% partial melting (corresponding to the electrical anomaly of northwestern Himalaya) imply a viscosity, η, of 10^{11} Pa.s (Table 2). Our data seem in good agreement with the experimental study of Misra et al. (2009), where the apparent viscosity of their synthetic sample yielded a value of $10^{11.62}$ Pa.s at a strain rate of 3×10^{-4} s^{-1}, at a temperature of 750 °C and for comparable melt percentages.

Pure melts, corresponding to the electrical anomaly beneath southern Tibet, have been shown to present lower viscosities, i.e. 10^4 Pa.s (Scaillet et al., 1996; Whittington et al., 2004). These two values (i.e. 10^{11} Pa.s and 10^4 Pa.s) are several orders of magnitude lower than previous estimations used in thermo-mechanical models of channel flow and crustal extrusion ($\eta=10^{18}$–10^{19} Pa.s) (Beaumont et al., 2001, 2004, 2006; Jamieson et al., 2004; Medvedev and Beaumont, 2006). Such low-viscosity regions provide a natural mechanism for localizing strain into the weakest parts of the deforming layers, as shown by previous field observations and demonstrated by experimental deformation studies (Brown, 2007; Kohlstedt and Holtzman, 2009; Marchildon and Brown, 2003; Rosenberg and Handy, 2005; Vanderhaeghe, 2009). Crustal melting in the Himalayan middle crust must therefore be an essential process in forming low-viscosity regions and thus crustal-scale thrusts and/or high strain shear zones, such as the STDs and the MCT (Fig. 1).

5.5. The aqueous fluid hypothesis in conflict with geochemical and geophysical observations

We have found that the aqueous fluids hypothesis cannot completely satisfy combined constraints from metamorphic fluid salinity, electrical resistivities and seismic velocities. Firstly, the question of the geochemical origin of brines is raised since the presence of Cl-rich sources in the Himalayan–Tibetan crust remains unproved. Secondly, fluid inclusions within rocks from the GHS show high salinity content (25 wt% NaCl; Spencer et al., 2011), which implies a resistivity value of $\sim75\times10^{-4}$ Ωm (Nesbitt, 1993). By using electrical mixing models (as in Section 5.2), we have found that the electrical anomalies beneath the Himalayan–Tibetan orogenic system (10–3 Ωm in Northwestern Himalaya and Southern Tibet, respectively) are best explained by ~0.8 vol% of connected brines for the aqueous fluid hypothesis (Supplementary Table 2). Such a low brine percentage cannot explain the corresponding low seismic velocity zone, which requires at least 10 vol % fluids (Makovsky and Klemperer, 1999).

Furthermore, by using the electrical mixing models we have determined that 10 vol% interconnected aqueous fluids would yield a resistivity value of ~0.11 Ωm. This calculated value is two orders of magnitude lower than the values assessed by MT-field campaigns (10–3 Ωm in Northwestern Himalaya and Southern Tibet, respectively; Arora et al., 2007; Li et al., 2003; Unsworth et al., 2005; Wei et al., 2001). The aqueous fluids hypothesis therefore yields a substantial discrepancy between seismic and electrical constraints.

6. Conclusion

New electrical resistivity measurements on partially molten metapelites have shown that the electrical anomalies detected by geophysical surveys beneath southern Tibet (3 Ωm) and northwestern Himalaya (10 Ωm) remarkably match fully molten leucogranite bodies and 25 vol% partially molten metapelites, respectively. Our study therefore corroborates that the processes (i.e. partial melting of metapelites and subsequent melt segregation) that generated the 25–13 Ma HHL must still be operating at depth beneath the Himalayan–Tibetan belt. Whether these processes are local or regional phenomena remains to be ascertained (Harrison, 2006; Hetényi et al., 2011).

The high melt percentages and corresponding viscosity values acquired during our experiments represent a benchmark for thermo-mechanical models, which must be calibrated against this inescapable constraint. The implementation of the electrical–seismic–petrological–thermal–rheology relationships made possible with our study constitutes a requirement for understanding which factors in such thermo-mechanical models are most likely to influence orogenic processes and therefore in improving our knowledge of the development and sustainment of large-scale orogens.

We finally suggest that forward modelling based on our laboratory electrical measurements and petrological–thermobarometric models of the Himalayan–Tibetan range should be confronted to field data from MT studies. Such an integrated methodology might lead to a revision of the minimum resistivity, translating into revised melt fractions, viscosity and strain localisations in the mid-crustal range.

Acknowledgements

This paper is part of L.H.'s Ph.D. supported by the French Ministère de l'Enseignement Supérieur et de la Recherche. This research is funded by the European Research Council, ERC, (Grant no. 279097) and by the ANR (Grant no. ANR-10-BLAN-62101). The authors would like to thank Mark Harrison for careful and efficient editorial handling as well as four anonymous reviewers for constructive comments that significantly improved this paper. We would also like to acknowledge Ida Di Carlo for analytical support, Mickael Laumonier for constructive discussions, and Esteban Le Moing and Philippe Teulat for technical assistance.

Appendix A. Supplementary material

Supplementary data associated with this article can be found in the online version at http://dx.doi.org/10.1016/j.epsl.2013.04.026.

References

Archie, G.E., 1942. The electrical resistivity log as an aid in determining some reservoir characteristics. Trans. Am. Inst. Min. Metall. Pet. Eng. 146, 54–62.

Arora, B.R., Unsworth, M.J., Rawat, G., 2007. Deep resistivity structure of the northwest Indian Himalaya and its tectonic implications. Geophys. Res. Lett. 34, L04307, http://dx.doi.org/10.1029/2006GL029165.

Beaumont, C., Jamieson, R.A., Nguyen, M.H., Lee, B., 2001. Himalayan tectonics explained by extrusion of a low-viscosity crustal channel coupled to focussed surface denudation. Nature 414, 738–742.

Beaumont, C., Jamieson, R.A., Nguyen, M.H., Medvedev, M., 2004. Crustal channel flows 1: numerical models with application to the tectonics of the Himalayan-Tibetan orogeny. J. Geophys. Res. 109, B06406, http://dx.doi.org/10.1029/2003JB002809.

Beaumont, C., Nguyen, M.H., Jamieson, R.A., Ellis, S., 2006. Crustal flow modes in large hot orogens. In: Law, R.D., Searle, M.P., Godin, L. (Eds.), Channel Flow, Ductile Extrusion and Exhumation in Continental Collision Zones. Geological Society London Special Publication, London, pp. 91–145.

Brown, M., 2007. Crustal melting and melt extraction, ascent and emplacement in orogens: mechanisms and consequences. J. Geol. Soc. London 164, 709–730.

Brown, L.D., Zhao, W., Nelson, K.D., Hauck, M., Alsdorf, D., Ross, A., Cogan, M., Clark, M., Liu, X., Che, J., 1996. Bright spots, structure and magmatism in southern Tibet from INDEPTH seismic reflection profiling. Science 274, 1688–1690.

Caldwell, W.B., Klemperer, S.L., Rai, S.S., Lawrence, J.F., 2009. Partial melt in the upper-middle crust of northwest Himalaya revealed by Rayleigh wave dispersion. Tectonophysics 477, 58–65.

Caricchi, L., Burlini, L., Ulmer, P., 2008. Propagation of P and S-waves in magmas with different crystal contents: insights into the crystallinity of magmatic reservoirs. J. Volcanol. Geotherm. Res. 178, 740–750.

Caricchi, L., Gaillard, F., Mecklenburgh, J., Le Trong, E., 2011. Determination of electrical conductivity during deformation of melt-bearing olivine aggregates: implications for electrical anisotropy in the oceanic low velocity zone. Earth Planet. Sci. Lett. 302, 81–94.

Connolly, J.A.D., 1990. Multivariable phase-diagrams: an algorithm based on generalized thermodynamics. Am. J. Sci. 290, 666–718.

Connolly, J.A.D., 2005. Computation of phase equilibria by linear programming: a tool for geodynamic modeling and its application to subduction zone decarbonation. Earth Planet. Sci. Lett. 236, 524–554.

Connolly, J.A.D., Kerrick, D.M., 1987. An algorithm based on generalized thermodynamics. CALPHAD 11, 1–55.

Connolly, J.A.D., Petrini, K., 2002. An automated strategy for calculation of phase diagram sections and retrieval of rock properties as a function of physical conditions. J. Metamorph. Petrol. 20, 697–708.

Faure, M., Monié, P., Pin, C., Maluski, H., Leloix, C., 2002. Late Visean thermal event in the northern part of the French Massif Central: new $^{40}Ar/^{39}Ar$ and Rb–Sr isotopic constraints on the Hercynian syn-orogenic extension. Int. J. Earth Sci. 91, 53–75, http://dx.doi.org/10.1007/s005310100202.

Ferri, F., Gibert, B., Violay, M., Cesare, B., 2013. Electrical conductivity in partially molten crust from measurements on metasedimentary enclaves. Tectonophysics 586, 84–94.

Gaillard, F., 2004. Laboratory measurements of electrical conductivity of hydrous and dry silicic melts under pressure. Earth Planet. Sci. Lett. 218, 215–228.

Gaillard, F., Marziano, G.I., 2005. Electrical conductivity of magma in the course of crystallization controlled by their residual liquid composition. J. Geophys. Res. 110, B06204, http://dx.doi.org/10.1029/2004JB003282.

Gaillard, F., Scaillet, B., Pichavant, M., 2004. Evidence for present-day leucogranite pluton growth in Tibet. Geology 32, 801–804.

Glover, P.W.J., Hole, M.J., Pous, J., 2000. A modified Archie's law for two conducting phases. Earth Planet. Sci. Lett. 180, 369–383.

Grant, F.S., West, G.F., 1965. Introduction to electrical methods. In: Schrock, R.R. (Ed.), Interpretation Theory in Applied Geophysics. McGraw-Hill, New York, pp. 385–401.

Harrison, T.M., 2006. Did the Himalayan Crystallines extrude partially molten from beneath the Tibetan Plateau. In: Law, R.D., Searle, M.P., Godin, L. (Eds.), Channel Flow, Ductile Extrusion and Exhumation in Continental Collision Zones. Geological Society London Special Publication, London, pp. 237–254.

Hashin, Z., Shtrikman, S., 1962. A variational approach to the theory of effective magnetic permeability of multiphase materials. J. Appl. Phys. 33, 3125–3131.

Hetényi, G., Vergne, J., Bollinger, L., Cattin, R., 2011. Discontinuous low-velocity zones in southern Tibet question the viability of the channel flow model. In: Gloaguen, R., Ratschbacher, L. (Eds.), Growth and Collapse of the Tibetan Plateau. Geological Society London Special Publication, London, pp. 99–108.

Hoke, L., Lamb, S., Hilton, D.R., Poreda, R., 2000. Southern limit of mantle-derived geothermal helium emissions in Tibet: implications for lithospheric structure. Earth Planet. Sci. Lett. 180, 297–308.

Huebner, J.S., Dillenburg, R.G., 1995. Impedance spectra of hot, dry silicate minerals and rock: qualitative interpretation of spectra. Am. Mineral. 80, 46–64.

Iacono-Marziano, G., Morizet, Y., Le Trong, E., Gaillard, F., 2012. New experimental data and semi-empirical parameterization of CO_2–H_2O solubility in mafic melts. Geochem. Cosmochim. Acta 97, 1–23.

Jamieson, R.A., Beaumont, C., Medvedev, S., Nguyen, M.H., 2004. Crustal channel flows: 2. Numerical models with implications for metamorphism in the Himalayan–Tibetan orogeny. Geophys. Res. Lett. 109, B06407, http://dx.doi.org/10.1029/2003JB002811.

Jamieson, R.A., Unsworth, M., Harris, N., Rosenberg, C.L., Schulmann, K., 2011. Crustal melting and the flow of mountains. Elements 7, 253–260, http://dx.doi.org/10.2113/gselements.7.4.253.

Kohlstedt, D.L., Holtzman, B.K., 2009. Shearing melt out of the Earth: an experimentalist's perspective on the influence of deformation on melt extraction. Annu. Rev. Earth Planet. Sci. 37, 561–593.

Law, R.D., Searle, M.P., Simpson, R.L., 2004. Strain, deformation temperatures and vorticity of flow at the top of the Greater Himalayan Slab, Everest Massif, Tibet. J. Geol. Soc. London 161, 305–320.

Li, S., Unsworth, M., Booker, J., Wei, W., Tan, H., Jones, A.G., 2003. Partial melt or aqueous fluid in the mid-crust of Southern Tibet? Constraints from INDEPTH magnetotelluric data. Geophys. J. Int. 153, 289–304.

Makovsky, Y., Klemperer, S.L., 1999. Measuring the seismic properties of Tibetan bright spots: evidence for free aqueous fluids in the Tibetan middle crust. J. Geophys. Res. 104, 10795–10825, http://dx.doi.org/10.1029/1998JB900074.

Marchildon, N., Brown, M., 2003. Spatial distribution of melt-bearing structures in anatectic rocks from Southern Brittany, France: implications for melt transfer at grain- to orogen-scale. Tectonophysics 364, 215–235.

Medvedev, S., Beaumont, C., 2006. Growth of continental plateaus by channel injection: models designed to address constraints and thermomechanical consistency. In: Law, R.D., Searle, M.P., Godin, L. (Eds.), Channel Flow, Ductile Extrusion and Exhumation in Continental Collision Zones. Geological Society London Special Publication, London, pp. 147–164.

Misra, S., Burlini, L., Burg, J.P., 2009. Strain localization and melt segregation in deforming metapelites. Phys. Earth Planet. Int. 177, 173–179.

Nábělek, J., Hetényi, G., Vergne, J., Sapkota, S., Kafle, B., Jiang, M., Su, H., Chen, J., Huang, B.-S., the Hi-CLIMB Team, 2009. Underplating in the Himalaya–Tibet collision zone revealed by the Hi-CLIMB experiment. Science 325, 1371–1374.

Nelson, K.D., Zhao, W., Brown, L.D., Kuo, J., Che, J., Liu, X., Klemperer, S.L., Makovsky, Y., Meissner, R., Mechie, J., Kind, R., Wenzel, F., Ni, J., Nábělek, J., Leshou, C., Tan, H., Wei, W., Jones, A.G., Booker, J., Unsworth, M., Kidd, W.S.F., Hauck, M., Alsdorf, D., Ross, A., Cogan, M., Wu, C., Sandvol, E., Edwards, M., 1996. Partially molten middle crust beneath southern Tibet: synthesis of Project INDEPTH results. Science 274, 1684–1688.

Nesbitt, B.E., 1993. Electrical resistivities of crustal fluids. J. Geophys. Res. 98, 4301–4310.

Paterson, M.S., Olgaard, D.L., 2000. Rock deformation tests to large shear strains in torsion. J. Struct. Geol. 22, 1341–1358.

Patiño Douce, A., Harris, N., 1998. Experimental constraints on Himalayan anatexis. J. Petrol. 39, 689–710.

Pichavant, M., Hammouda, T., Scaillet, B., 1996. Control of redox state and Sr isotopic composition of granitic magmas: a critical evaluation of the role of source rocks. Trans. R. Soc. Edinburgh Earth Sci. 87, 321–329.

Pommier, A., Gaillard, F., Pichavant, M., Scaillet, B., 2008. Laboratory measurements of electrical conductivities of hydrous and dry Mount Vesuvius melts under pressure. J. Geophys. Res.113, B05205, http://dx.doi.org/10.1029/2007JB005269.

Pommier, A., Le Trong, E., 2011. SIGMELTS: a web portal for electrical conductivity calculations in geosciences. Comput. Geosci. 37, 1450–1459.

Roberts, J.J., Tyburczy, J.A., 1991. Frequency dependent electrical properties of polycrystalline olivine compacts. J. Geophys. Res. 96, 16205–16222.

Roberts, J.J., Tyburczy, J.A., 1999. Partial-melt electrical conductivity: influence of melt composition. J. Geol. Res. 104, 7055–7065.

Rosenberg, C.L., Handy, M.R., 2005. Experimental deformation of partially melted granite revisited: implications for the continental crust. J. Metamorph. Geol. 23, 19–28.

Royden, L.H., Burchfield, B.C., van der Hilst, R.D., 2008. The geological evolution of the Tibetan Plateau. Science 321, 1054–1058.

Rubie, D.C., Brearly, A.J., 1990. A model for rates of disequilibrium melting during metamorphism. In: Ashworth, J.R., Brown, M. (Eds.), High-temperature Metamorphism and Crustal Anatexis. Unwin Hyman, London, pp. 57–86.

Sawyer, E.D., Cesare, B., Brown, M., 2011. When the continental crust melts. Elements 7, 229–234.

Scaillet, B., Holtz, F., Pichavant, M., Schmidt, M., 1996. Viscosity of Himalayan leucogranites: implications for mechanisms of granitic magma ascent. J. Geophys. Res. 101, 27691–27699.

Scaillet, B., Pichavant, M., Roux, J., 1995. Experimental crystallization of leucogranite magmas. J. Petrol. 36, 663–705.

Schilling, F.R., Partzsch, G.M., 2001. Quantifying partial melt fraction in the crust beneath the central Andes and the Tibetan Plateau. Phys. Chem. Earth 26, 239–246.

Schmeling, H., 1986. Numerical models on the influence of partial melt on elastic, anelastic and electrical properties of rocks. Part II: electrical conductivity. Phys. Earth Planet. Inter. 43, 123–136.

Searle, M.P., Law, R.D., Jessup, M., 2006. Crustal structure, restoration and evolution of the Greater Himalaya in Nepal–South Tibet: implications for channel flow and ductile extrusion of the middle crust. In: Law, R.D., Searle, M.P., Godin, L. (Eds.), Channel Flow, Ductile Extrusion and Exhumation in Continental Collision Zones. Geological Society London Special Publication, London, pp. 355–378.

Searle, M.P., Parrish, R.R., Hodges, K.V., Hurford, A., Ayres, M.W., Whitehouse, M.J., 1997. Shisha Pangmaleucogranite, south Tibetan Himalaya: field relations, geochemistry, age, origin, and emplacement. J. Geol. 105, 295–318.

Shankland, T.J., Peyronneau, J., Poirier, J.P., 1993. Electrical conductivity of the Earth's lower mantle. Nature 366, 453–455.

Spencer, C.J., Harris, R.A., Sachan, H.K., Saxena, A., 2011. Depositional provenance of the Greater Himalayan Sequence, Garhwal Himalaya: implications for tectonic setting. J. Asian Earth Sci. 41, 344–354.

Unsworth, M.J., Jones, A.G., Wei, W., Marquis, G., Gokarn, S.G., Spratt, J.E., Project INDEPTH Team, 2005. Crustal rheology of the Himalaya and southern Tibet inferred from magnetotelluric data. Nature 438, 78–81.

Vanderhaeghe, O., 2009. Migmatites, granites and orogeny: flow modes of partially-molten rocks and magmas associated with melt/solid segregation in orogenic belts. Tectonophysics 477, 119–134.

Waff, H.S., 1974. Theoretical consideration of electrical conductivity in a partially molten mantle and implications for geothermometry. J. Geophys. Res. 79, 4003–4010.

Wei, W., Unsworth, M., Jones, A.G., Booker, J., Tan, H., Nelson, K.D., Chen, L., Li, S., Solon, K., Bedrosian, P., 2001. Detection of widespread fluids in the Tibetan crust by magnetotelluric studies. Science 292, 716–718.

Whittington, A.G., Richet, P., Behrens, H., Holtz, F., Scaillet, B., 2004. Experimental temperature–X(H_2O)–viscosity relationship for leucogranites and comparison with synthetic silicic liquids. Trans. R. Soc. Edinburgh Earth Sci. 95, 59–71.

Yin, A., Harrison, T.M., 2000. Geologic evolution of the Himalayan–Tibetan orogen. Annu. Rev. Earth Planet. Sci. 28, 211–280.

Yokoyama, T., Nakai, S., Waikita, H., 1999. Helium and carbon isotopic compositions of hot spring gases in the Tibetan Plateau. J. Volcanol. Geotherm. Res. 88, 99–107.

Yoshino, T., McIsaac, E., Laumonier, M., Katsura, T., 2012. Electrical conductivity of partial molten carbonate peridotite. Phys. Earth Planet. Int. 194–195, 1–9.

Yoshino, T., Noritake, F., 2011. Unstable graphite films on grain boundaries in crustal rocks. Earth Planet. Sci. Lett. 306, 186–192.

Zhao, W., Nelson, K.D., Project INDEPTH Team, 1993. Deep seismic reflection evidence for continental underthrusting beneath southern Tibet. Nature 366, 557–559.

Conclusion

The aim of this thesis was to establish a consistent olivine grain growth law, which takes into account dry, melt-free grain boundary migration (slow grain growth rate regime) as well as the influence of a melt or a fluid phase on the boundary kinetics (fast grain growth rate regime). In order to achieve this goal, I have used the experimental atmospheric database on olivine grain growth aggregates for the dry end-member (Chapter 1), whereas for the liquid-bearing end-member, I report new high pressure/high temperature static grain growth of liquid-bearing aggregates, which was confronted to previously published analogous experimental samples (Chapter 2).

The following conclusions for olivine grain growth have been reached:

- Confrontation of the appropriate grain growth theoretical equations for liquid-free and liquid-bearing aggregates to the experimental grain sizes indicate that lattice diffusion and liquid diffusion cannot predict the measured grain sizes from laboratory experiments.
- Dry olivine grain growth is however very well constrained through diffusion of silicon at grain boundaries, implying a grain size exponent of $n = 2$, whereas growth of liquid-bearing olivine aggregates has shown to be limited by reactions at the crystal/liquid interface through precipitation at the crystal surfaces. In this case, the grain size exponent also has a value of $n = 2$.
- The fact that grain boundaries of liquid-bearing aggregates depict different wetting properties for each grain, meaning that a certain amount of grain boundaries are liquid-free, leads to the implementation of two complementary parameters in the unified grain growth equation, namely contiguity, Ψ, and wetness, $\varphi = 1 - \Psi$ (introduced in Earth sciences by Takei, 1998). These fundamental parameters were therefore reformulated from the study of Yoshino et al. (2005) and incorporated within the unified grain growth law (Chapter 2).
- The effective dry, melt-free grain boundary width was determined from the atmospheric database by least squares fit to the grain growth data, indicating a value of $\delta = 29.21^{+37}_{-16}$nm. The effective grain boundary width is a factor 30 superior to the structural grain boundary width established by the study of Hiraga and Kohlstedt (2007) and is in very good agreement with a transmission electron microscopy study from Marquardt et al. (2011), establishing an effective grain boundary width of $\sim$18 nm.

Some limitations and suggestions for future work

- In this manuscript, I have used the Burke and Turnbull analysis to describe grain growth rates through the migration of grain boundaries (Burke and Turnbull, 1952). The theoretical grain size exponent value, n_{theo}, shows considerable discrepancy with the empirically determined grain size exponent, n_{emp} (up to almost a factor 5, e.g. $n_{theo} = 2 - 3$ vs. $n_{emp} = 9.2$). Similar differences have been observed in material sciences on sintering and grain growth of ceramics and metals, which is mainly explained by the impurity content

of the polycrystalline sample (e.g. chapter 11 in Humphreys and Hatherly, 2004). It has indeed been shown that a few parts per million of impurity levels within the aggregates (ceramics and metals) generally lead to empirical grain size exponents ranging from >2 to <4.

- The Burke and Turnbull analysis (Burke and Turnbull, 1952) does not consider topological aspects for grain growth, in other words, space-filling requirements ruled by surface tension equilibrium (i.e. "Normal grain growth results from the interaction between the topological requirements of space-filling and the geometrical needs of surface tension equilibrium", Smith, 1952). In this manuscript, we have modeled grain growth by using a *statistical* theory, which considers that the behavior of a single grain within the assembly is on average a good representation of that of the polycrystalline aggregate. Numerous studies have theorized grain growth in a *deterministic* manner, where the growth and shrinkage of every grain within the polycrystalline assemblage are considered, therefore taking into account the space-filling requirements as suggested by Smith (1952). The unified grain growth law determined in this manuscript should therefore be confronted to such deterministic grain growth models, such as the one computed in Bercovici and Ricard (2012).

- The dry, melt-free grain growth equation (Chapter 1) considers diffusion of silicon at grain boundaries, by using the grain boundary diffusion coefficient determined in the study of Fei et al. (2016), which was measured along the grain boundary (i.e. parallel to the grain boundary, $D_{gb}^{\parallel}$). Grain growth is a process by which atoms from one side of the grain boundary move perpendicularly to the grain boundary to reattach on the other side. One key question would be whether diffusion occurring perpendicularly ($D_{gb}^{\perp}$) to the grain boundary is of the same order as parallel diffusion and how this affects grain growth rates.

- The melt distribution assumptions used in the model for liquid-bearing grain growth (Chapter 2) are simple geometrical configurations (e.g. Hashin-Shtrikman geometrical assumptions of dispersed spheres in a liquid matrix). More complex geometrical assumptions should be taken into account to completely rule out liquid diffusion-controlled grain growth, such as quadruple junctions or triple junctions with partially wetted grain boundaries.

Conclusion

L'objectif de cette thèse était d'établir une loi de croissance d'olivine, combinant à la fois la croissance en condition anhydre (régime de croissance lent) et la croissance influencée par la présence de liquide silicaté ou acqueux (régime de croissance rapide). Afin d'atteindre cet objectif, j'ai utilisé les données de la littérature obtenues à partir d'expériences réalisées à pression atmosphérique dans le but de caractériser le pôle de croissance anhydre (Chapter 1). Le pôle de croissance influencée par la présence de liquide silicaté ou acqueux a pu être déterminé grâce à de nouvelles expériences haute température, haute pression réalisées sur des agrégats d'olivine contenant des quantités de liquide silicaté ou acqueux variables. Les résultats expérimentaux de cette thèse ont été comparés avec les données expérimentales de la littérature (Chapter 2).

Les conclusions sur la croissance de grains d'olivine sont les suivantes :

- La comparaison des lois de croissance d'olivine anhydre et en présence de liquide silicaté ou acqueux avec les tailles de grains expérimentales montre que la diffusion dans le volume du grain ou la diffusion dans le liquide ne sont pas les paramètres clés régissant la croissance d'olivine.

- La croissance d'olivine anhydre est très bien contrainte avec le coefficient de diffusion du silicium aux joints de grains, ce qui implique un exposant à la taille de grains à $n = 2$. La croissance d'olivine en présence de liquide silicaté ou acqueux est, quant à elle, limitée par les réactions aux interfaces cristal/liquide, qui prend en compte un coefficient de précipitation. Dans ce cas, l'exposant à la taille de grains est également fixé à $n = 2$.

- Les agrégats d'olivine contenant du liquide silicaté ou acqueux ont montré des propriétés de mouillage du liquide différentes en fonction du grain étudié. Ceci implique qu'un certain nombre de joints de grains sont exempts de liquide et qu'il est donc nécessaire d'utiliser les paramètres de contiguité, Ψ, et son complémentaire, la mouillabilité, $\varphi = 1 - \Psi$ dans la loi de croissance unifiée d'olivine. Ces paramètres fondamentaux, introduits dans les sciences de la Terre par Takei (1998), ont été reformulés d'après l'étude de Yoshino et al. (2005) et ainsi incorporé dans la loi de croissance unifiée (Chapter 2).

- L'épaisseur effective de joint de grains anhydre a été déterminée à partir de la base de données atmosphérique et établie à $\delta = 29.21|^{+37}_{-16}$nm. L'épaisse effective de joint de grains est 30 fois supérieure à l'épaisseur structurale de joint de grains (Hiraga and Kohlstedt, 2007) et est en accord avec une étude de microscopie électronique à transmission par Marquardt et al. (2011), qui établit une épaisseur effective de $\sim$18 nm.

Quelques limitations et suggestions pour de futurs travaux de recherche

- Dans ce manuscrit, j'ai utilisé l'analyse de Burke et Turnbull pour décrire la croissance de grains, qui considère que c'est la migration des joints de grains qui permet aux cristaux de croître (Burke and Turnbull, 1952). L'exposant à la taille de grains théorique,

n_{theo}, montre une différence significative avec les exposants de grains déterminés empiriquement, n_{emp} (allant dans certains cas jusqu'à un facteur 5, e.g. $n_{theo} = 2 - -3$ vs. $n_{emp} = 9.2$). Des différences similaires ont été observées dans les sciences des matériaux lors du frittage et de la croissance de grains des céramiques et métaux. Ceci serait justifié par la présence d'impuretés dans l'échantillon polycristallin étudié (e.g. chapitre 11 dans Humphreys and Hatherly, 2004). En effet, il a été montré que seulement quelques parties par million d'impuretés dans l'agrégat (de céramique ou métal) impliquait une valeur empirique d'exposant à la taille de grains comprise entre >2 et <4.

- L'analyse de Burke et Turnbull (Burke and Turnbull, 1952) ne considère pas les aspects topologiques pour la croissance de grains, c'est-à-dire qu'à l'équilibre, tous les espaces doivent être remplis sous l'emprise des tensions de surface (i.e. "Normal grain growth results from the interaction between the topological requirements of space-filling and the geometrical needs of surface tension equilibrium", Smith, 1952). Dans ce manuscrit, nous avons décrit la croissance de grains grâce à une théorie *statistique*, qui considère que le comportement d'un grain au sein de l'agrégat est en moyenne une bonne représentation de l'agrégat polycristallin. De nombreuses études ont décrit la croissance de grains d'une manière *déterministe*, où la croissance et la décroissance de chaque grain au sein de l'agrégat sont considérés. Ceci tient donc compte du remplissage d'espace suggéré par Smith (1952). Il serait donc intéressant de comparer la croissance de grains unifiée déterminée dans ce manuscrit avec des modèles de croissance déterministes, comme celui de Bercovici and Ricard (2012).

- La croissance de grains anhydres (Chapter 1) tient compte de la diffusion du silicium aux joints de grains et utilise ainsi le coefficient de diffusion aux joints de grains déterminés dans l'étude de Fei et al. (2016). Ce coefficient a été mesuré le long des joints de grains, c'est-à-dire parallèle au joint de grains ($D^{\parallel}_{gb}$). La croissance de grains est un processus où chaque atome se déplace perpendiculairement d'un bord à l'autre du joint de grains. Nous pourrions nous demander si la diffusion perpendiculaire ($D^{\perp}_{gb}$) aux joints de grains est du même ordre de grandeur que la diffusion parallèle et comment ceci pourrait affecter la croissance de grains.

- Nous avons émis des hypothèses quant à la distribution du liquide silicaté au sein des agrégats d'olivine du Chapter 2 qui sont seulement des cas géométriques assez simples (e.g. l'hypothèse de Hashin-Shtrikman considérant des sphères de solides dispersées dans une matrice liquide). Les cas géométriques simples proposés dans le Chapter 2 ont ainsi permet d'éliminer la diffusion dans le liquide comme processus régissant la croissance de grains en présence de liquide. Seulement, il serait intéressant de considérer des cas géométriques plus complexes afin de réellement éliminer la diffusion dans le liquide comme processus limitant. Il serait possible, qu'en présence de joints triple ou quadruples mouillés par du liquide, la croissance de grains puisse être régie par la diffusion dans le liquide.

Bibliographie

Ardia, P., Hirschmann, M., Withers, A., Tenner, T., 2012. H_2O storage capacity of olivine at 5–8 GPa and consequences for dehydration partial melting of the upper mantle. Earth and Planetary Science Letters 345, 104–116.

Arora, B., Unsworth, M. J., Rawat, G., 2007. Deep resistivity structure of the northwest indian himalaya and its tectonic implications. Geophysical Research Letters 34 (4).

Atkinson, H., 1988. Overview no. 65 : theories of normal grain growth in pure single phase systems. Acta Metallurgica 36 (3), 469–491.

Austin, N. J., Evans, B., 2007. Paleowattmeters : A scaling relation for dynamically recrystallized grain size. Geology 35 (4), 343–346.

Baba, K., Chave, A. D., Evans, R. L., Hirth, G., Mackie, R. L., 2006. Mantle dynamics beneath the east pacific rise at 17 S : Insights from the mantle electromagnetic and tomography (MELT) experiment. Journal of Geophysical Research 111 (B2).

Behn, M. D., Hirth, G., Elsenbeck II, J. R., 2009. Implications of grain size evolution on the seismic structure of the oceanic upper mantle. Earth and Planetary Science Letters 282 (1), 178–189.

Bercovici, D., 2003. The generation of plate tectonics from mantle convection. Earth and Planetary Science Letters 205 (3), 107–121.

Bercovici, D., Ricard, Y., 2012. Mechanisms for the generation of plate tectonics by two-phase grain-damage and pinning. Physics of the Earth and Planetary Interiors 202, 27–55.

Bercovici, D., Ricard, Y., Richards, M. A., 2000. The Relation Between Mantle Dynamics and Plate Tectonics : A Primer. American Geophysical Union, pp. 5–46.

Brearly, M., Scarfe, C. M., 1986. Dissolution rates of upper mantle minerals in an alkali basalt melt at high pressure : an experimental study and implications for ultramafic xenolith survival. Journal of Petrology 27 (5), 1157–1182.

Brown, L., Zhao, W., Nelson, K., Hauck, M., Alsdorf, D., Ross, A., Cogan, M., Clark, M., Liu, X., Che, J., 1996. Bright spots, structure, and magmatism in southern tibet from indepth seismic reflection profiling. Science 274 (5293), 1688–1690.

Burke, J., Turnbull, D., 1952. Recrystallization and grain growth. Progress in metal physics 3, 220–292.

Bystricky, M., Heidelbach, F., Mackwell, S., 2006. Large-strain deformation and strain partitioning in polyphase rocks : Dislocation creep of olivine–magnesiowüstite aggregates. Tectonophysics 427 (1), 115–132.

Bystricky, M., Kunze, K., Burlini, L., Burg, J.-P., 2000. High shear strain of olivine aggregates : Rheological and seismic consequences. Science 290 (5496), 1564–1567.

Cabane, H., Laporte, D., Provost, A., 2005. An experimental study of ostwald ripening of olivine and plagioclase in silicate melts : implications for the growth and size of crystals in magmas. Contributions to Mineralogy and Petrology 150 (1), 37–53.

Caldwell, W. B., Klemperer, S. L., Rai, S. S., Lawrence, J. F., 2009. Partial melt in the upper-middle crust of the northwest himalaya revealed by rayleigh wave dispersion. Tectonophysics 477 (1), 58–65.

Chakraborty, S., Farver, J. R., Yund, R. A., Rubie, D. C., 1994. Mg tracer diffusion in synthetic forsterite and san carlos olivine as a function of P, T and f_{O_2}. Physics and Chemistry of Minerals 21 (8), 489–500.

Cooper, R., Kohlstedt, D., 1982. Interfacial energies in the olivine-basalt system. Adv. Earth Planet. Sci 12, 217–228.

Cordier, P., Demouchy, S., Beausir, B., Taupin, V., Barou, F., Fressengeas, C., et al., 2014. Disclinations provide the missing mechanism for deforming olivine-rich rocks in the mantle. Nature 507 (7490), 51–56.

Davies, G. F., Richards, M. A., 1992. Mantle convection. The Journal of Geology, 151–206.

Detert, K., 1978. Secondary recrystallization (grain growth in metals during annealing). In : Recrystallization of Metallic Materials. F. Haessner, Dr. Riederer-Verlag GmbH, Stuttgart, pp. 97–109.

Dohmen, R., Chakraborty, S., Becker, H.-W., 2002. Si and O diffusion in olivine and implications for characterizing plastic flow in the mantle. Geophysical research letters 29 (21).

Donaldson, C., 1990. Forsterite dissolution in superheated basaltic, andesitic and rhyolitic melts. Mineral. Mag 54, 67–74.

Donaldson, C. H., 1985. The rates of dissolution of olivine, plagioclase, and quartz in a basalt melt. Mineralogical Magazine 49 (354), 683–693.

Edwards, B., Russell, J., 1996. A review and analysis of silicate mineral dissolution experiments in natural silicate melts. Chemical Geology 130 (3), 233–245.

Evans, B., Renner, J., Hirth, G., 2001. A few remarks on the kinetics of static grain growth in rocks. International Journal of Earth Sciences 90 (1), 88–103.

Farver, J. R., Yund, R. A., 2000. Silicon diffusion in forsterite aggregates : Implications for diffusion accommodated creep. Geophysical Research Letters 27 (15), 2337–2340.

Farver, J. R., Yund, R. A., Rubie, D. C., 1994. Magnesium grain boundary diffusion in forsterite aggregates at 1000–1300°Cand 0.1 MPa to 10 GPa. Journal of Geophysical Research : Solid Earth 99 (B10), 19809–19819.

Faul, U. H., Scott, D., 2006. Grain growth in partially molten olivine aggregates. Contributions to Mineralogy and Petrology 151 (1), 101–111.

Fei, H., Hegoda, C., Yamazaki, D., Wiedenbeck, M., Yurimoto, H., Shcheka, S., Katsura, T., 2012. High silicon self-diffusion coefficient in dry forsterite. Earth and Planetary Science Letters 345, 95–103.

Fei, H., Koizumi, S., Sakamoto, N., Hashiguchi, M., Yurimoto, H., Marquardt, K., Miyajima, N., Yamazaki, D., Katsura, T., 2016. New constraints on upper mantle creep mechanism inferred from silicon grain-boundary diffusion rates. Earth and Planetary Science Letters 433, 350 – 359.

Fei, H., Wiedenbeck, M., Yamazaki, D., Katsura, T., 2013. Small effect of water on upper-mantle rheology based on silicon self-diffusion coefficients. Nature 498 (7453), 213–215.

Gaillard, F., Pichavant, M., Scaillet, B., 2003. Experimental determination of activities of FeO and Fe_2O_3 components in hydrous silicic melts under oxidizing conditions. Geochimica et Cosmochimica Acta 67 (22), 4389–4409.

Gaillard, F., Scaillet, B., Pichavant, M., 2004. Evidence for present-day leucogranite pluton growth in tibet. Geology 32 (9), 801–804.

Garapić, G., Faul, U., Brisson, E., 2013. High-resolution imaging of the melt distribution in partially molten upper mantle rocks : evidence for wetted two-grain boundaries. Geochemistry, Geophysics, Geosystems 14 (3), 556–566.

Gardés, E., Heinrich, W., 2011. Growth of multilayered polycrystalline reaction rims in the MgO–SiO_2 system, part II : modelling. Contributions to Mineralogy and Petrology 162 (1), 37–49.

German, R. M., Griffo, A., Liu, Y., 1997. Gravitational effects on grain coarsening during liquid-phase sintering. Metallurgical and Materials Transactions A 28 (1), 215–221.

German, R. M., Olevsky, E. A., 1998. Modeling grain growth dependence on the liquid content in liquid-phase-sintered materials. Metallurgical and Materials Transactions A 29 (12), 3057–3067.

Gottschalk, M., 1997. Internally consistent thermodynamic data for rock-forming minerals in the system SiO_2–TiO_2–Al_2O_3–CaO–MgO–FeO–K_2O–Na_2O–H_2O–CO_2. European Journal of Mineralogy 9 (1), 175–223.

Greenwood, G., 1956. The growth of dispersed precipitates in solutions. Acta Metallurgica 4 (3), 243–248.

Greenwood, G., 1969. Particle coarsening. In : The mechanism of phase transformations in crsytalline solids. Vol. 33. Inst. Metals Monogr., pp. 103–110.

Gueydan, F., Précigout, J., Montési, L. G., 2014. Strain weakening enables continental plate tectonics. Tectonophysics 631, 189 – 196.

Hall, C. E., Parmentier, E., 2003. Influence of grain size evolution on convective instability. Geochemistry, Geophysics, Geosystems 4 (3).

Hashim, L., Gaillard, F., Champallier, R., Le Breton, N., Arbaret, L., Scaillet, B., 2013. Experimental assessment of the relationships between electrical resistivity, crustal melting and strain localization beneath the himalayan–tibetan belt. Earth and Planetary Science Letters 373, 20–30.

Hetényi, G., Vergne, J., Bollinger, L., Cattin, R., 2011. Discontinuous low-velocity zones in southern tibet question the viability of the channel flow model. Geological Society, London, Special Publications 353 (1), 99–108.

Hiraga, T., Kohlstedt, D. L., 2007. Equilibrium interface segregation in the diopside–forsterite system I : Analytical techniques, thermodynamics, and segregation characteristics. Geochimica et cosmochimica acta 71 (5), 1266–1280.

Hiraga, T., Tachibana, C., Ohashi, N., Sano, S., 2010. Grain growth systematics for forsterite ± enstatite aggregates : Effect of lithology on grain size in the upper mantle. Earth and Planetary Science Letters 291 (1), 10–20.

Hirschmann, M. M., Tenner, T., Aubaud, C., Withers, A., 2009. Dehydration melting of nominally anhydrous mantle : the primacy of partitioning. Physics of the Earth and Planetary Interiors 176 (1), 54–68.

Hirth, G., Kohlstedt, D., 1995a. Experimental constraints on the dynamics of the partially molten upper mantle : Deformation in the diffusion creep regime. Journal of Geophysical Research 100 (B2), 1981–2001.

Hirth, G., Kohlstedt, D., 1995b. Experimental constraints on the dynamics of the partially molten upper mantle : 2. deformation in the dislocation creep regime. Journal of Geophysical Research 100 (B8), 15441–15449.

Hirth, G., Kohlstedt, D., 2003. Rheology of the upper mantle and the mantle wedge : A view from the experimentalists. Geophysical Monograph Series 138, 83–105.

Höink, T., Jellinek, A. M., Lenardic, A., 2011. Viscous coupling at the lithosphere-asthenosphere boundary. Geochemistry, Geophysics, Geosystems 12 (10).

Humphreys, F., Hatherly, M., 2004. Recrystallization and related annealing phenomena. Elsevier.

Iacono-Marziano, G., Morizet, Y., Le Trong, E., Gaillard, F., 2012. New experimental data and semi-empirical parameterization of H_2O–CO_2 solubility in mafic melts. Geochimica et Cosmochimica Acta 97, 1–23.

Javoy, M., Pineau, F., 1991. The volatiles record of a "popping" rock from the mid-atlantic ridge at 14 N : chemical and isotopic composition of gas trapped in the vesicles. Earth and Planetary Science Letters 107 (3), 598–611.

Joesten, R. L., 1991. Kinetics of coarsening and diffusion-controlled mineral growth. Reviews in Mineralogy and Geochemistry 26 (1), 507–582.

Kang, S.-J. L., 2005. Sintering : densification, grain growth and microstructure. Butterworth-Heinemann.

Karato, S.-I., 1989. Grain growth kinetics in olivine aggregates. Tectonophysics 168 (4), 255–273.

Karato, S.-I., 2008. Deformation of earth materials. An Introduction to the Rheology of Solid Earth 463.

Karato, S.-i., Toriumi, M., Fujii, T., 1980. Dynamic recrystallization of olivine single crystals during high-temperature creep. Geophysical Research Letters 7 (9), 649–652.

Keeping, E., 1995. Introduction to Statistical Inference. Dover Publications, New York.

Law, R., Searle, M., Simpson, R., 2004. Strain, deformation temperatures and vorticity of flow at the top of the greater himalayan slab, everest massif, tibet. Journal of the Geological Society 161 (2), 305–320.

Lesher, C., Hervig, R., Tinker, D., 1996. Self diffusion of network formers (silicon and oxygen) in naturally occurring basaltic liquid. Geochimica et Cosmochimica Acta 60 (3), 405–413.

Lesne, P., Scaillet, B., Pichavant, M., Iacono-Marziano, G., Beny, J.-M., 2011. The H_2O solubility of alkali basaltic melts : an experimental study. Contributions to Mineralogy and Petrology 162 (1), 133–151.

Li, S., Unsworth, M. J., Booker, J. R., Wei, W., Tan, H., Jones, A. G., 2003. Partial melt or aqueous fluid in the mid-crust of southern tibet ? constraints from indepth magnetotelluric data. Geophysical Journal International 153 (2), 289–304.

Lifshitz, I. M., Slyozov, V. V., 1961. The kinetics of precipitation from supersaturated solid solutions. Journal of physics and chemistry of solids 19 (1-2), 35–50.

Lu, P., German, R., 2001. Multiple grain growth events in liquid phase sintering. Journal of materials science 36 (14), 3385–3394.

Makovsky, Y., Klemperer, S. L., 1999. Measuring the seismic properties of tibetan bright spots-evidence for free aqueous fluids in the tibetan middle crust. Journal of Geophysical Research 104 (B5), 10795–10825.

Marquardt, K., Ramasse, Q. M., Kisielowski, C., Wirth, R., 2011. Diffusion in yttrium aluminium garnet at the nanometer-scale : Insight into the effective grain boundary width. American Mineralogist 96 (10), 1521–1529.

Martin, J., Doherty, R., 1976. Doherty, Stability of Microstructure in Metallic Systems. Cambridge University Press, Cambridge.

Nábělek, J., Hetényi, G., Vergne, J., Sapkota, S., Kafle, B., Jiang, M., Su, H., Chen, J., Huang, B.-S., et al., 2009. Underplating in the himalaya-tibet collision zone revealed by the hi-climb experiment. Science 325 (5946), 1371–1374.

Naif, S., Key, K., Constable, S., Evans, R., 2013. Melt-rich channel observed at the lithosphere-asthenosphere boundary. Nature 495 (7441), 356–359.

Nichols, S. J., Mackwell, S. J., 1991. Grain growth in porous olivine aggregates. Physics and Chemistry of Minerals 18 (4), 269–278.

Ohuchi, T., Nakamura, M., 2007a. Grain growth in the forsterite–diopside system. Physics of the Earth and Planetary Interiors 160 (1), 1–21.

Ohuchi, T., Nakamura, M., 2007b. Grain growth in the system forsterite–diopside–water. Physics of the Earth and Planetary Interiors 161 (3), 281–304.

Ohuchi, T., Nakamura, M., Michibayashi, K., 2010. Effect of grain growth on cation exchange between dunite and fluid : implications for chemical homogenization in the upper mantle. Contributions to Mineralogy and Petrology 160 (3), 339–357.

Patiño Douce, A. E., Harris, N., 1998. Experimental constraints on himalayan anatexis. Journal of Petrology 39 (4), 689–710.

Pearce, M. A., Wheeler, J., 2011. Grain growth and the lifetime of diffusion creep deformation. Geological Society, London, Special Publications 360 (1), 257–272.

Pommier, A., Leinenweber, K., Kohlstedt, D. L., Qi, C., Garnero, E. J., Mackwell, S. J., Tyburczy, J. A., 2015. Experimental constraints on the electrical anisotropy of the lithosphere-asthenosphere system. Nature 522 (7555), 202–206.

Précigout, J., Gueydan, F., 2009. Mantle weakening and strain localization : Implications for the long-term strength of the continental lithosphere. Geology 37 (2), 147–150.

Richard, G. C., Kanjilal, S., Schmeling, H., 2012. Solitary-waves in geophysical two-phase viscous media : a semi-analytical solution. Physics of the Earth and Planetary Interiors 198, 61–66.

Roberts, J. J., Tyburczy, J. A., 1999. Partial-melt electrical conductivity : Influence of melt composition. Journal of Geophysical Research 104 (B4), 7055–7065.

Royet, J.-P., 1991. Stereology : a method for analyzing images. Progress in neurobiology 37 (5), 433–474.

Rychert, C. A., Schmerr, N., Harmon, N., 2012. The pacific lithosphere-asthenosphere boundary : Seismic imaging and anisotropic constraints from ss waveforms. Geochemistry, Geophysics, Geosystems 13 (9).

Sarafian, E., Evans, R., Collins, J. A., Elsenbeck, J., Gaetani, G. A., Gaherty, J. B., Hirth, G., Lizarralde, D., et al., 2015. The electrical structure of the central pacific upper mantle constrained by the nomelt experiment. Geochemistry, Geophysics, Geosystems 16 (4), 1115–1132.

Scaillet, B., Pichavant, M., Roux, J., 1995. Experimental crystallization of leucogranite magmas. Journal of Petrology 36 (3), 663–705.

Schilling, F., Partzsch, G., 2001. Quantifying partial melt fraction in the crust beneath the central andes and the tibetan plateau. Physics and Chemistry of the Earth, Part A : Solid Earth and Geodesy 26 (4), 239–246.

Schmerr, N., 2012. The gutenberg discontinuity : Melt at the lithosphere-asthenosphere boundary. Science 335 (6075), 1480–1483.

Searle, M. P., Law, R. D., Jessup, M. J., 2006. Crustal structure, restoration and evolution of the greater himalaya in nepal-south tibet : implications for channel flow and ductile extrusion of the middle crust. Geological Society, London, Special Publications 268 (1), 355–378.
URL `http://sp.lyellcollection.org/content/268/1/355.abstract`

Selway, K., 2015. Negligible effect of hydrogen content on plate strength in east africa. Nature Geoscience 8 (7), 543–546.

Seyhan, I., Ratke, L., Bender, W., Voorhees, P., 1996. Ostwald ripening of solid-liquid Pb-Sn dispersions. Metallurgical and Materials Transactions A 27 (9), 2470–2478.

Sifré, D., Gardés, E., Massuyeau, M., Hashim, L., Hier-Majumder, S., Gaillard, F., 2014. Electrical conductivity during incipient melting in the oceanic low-velocity zone. Nature 509 (7498), 81–85.

Skemer, P., Warren, J. M., Hansen, L. N., Hirth, G., Kelemen, P. B., 2013. The influence of water and lpo on the initiation and evolution of mantle shear zones. Earth and Planetary Science Letters 375, 222–233.

Smith, C., 1952. Metal interfaces. ASM, Cleveland, OH.

Smith, C. S., 1948. Grains, phases, and interphases : an interpretation of microstructure. Trans. Metall. Soc. 175, 15–51.

Stixrude, L., Lithgow-Bertelloni, C., 2005. Mineralogy and elasticity of the oceanic upper mantle : Origin of the low-velocity zone. Journal of Geophysical Research : Solid Earth 110 (B3), B03204.

Stolper, E., 1982. Water in silicate glasses : an infrared spectroscopic study. Contributions to Mineralogy and Petrology 81 (1), 1–17.

Tackley, P. J., 2000. The Quest for Self-Consistent Generation of Plate Tectonics in Mantle Convection Models. American Geophysical Union, pp. 47–72.

Takei, Y., 1998. Constitutive mechanical relations of solid-liquid composites in terms of grain-boundary contiguity. Journal of Geophysical Research 103 (B8), 18183–18203.

Takei, Y., 2002. Effect of pore geometry on vp/vs : From equilibrium geometry to crack. Journal of Geophysical Research : Solid Earth 107 (B2).

Takei, Y., Hier-Majumder, S., 2009. A generalized formulation of interfacial tension driven fluid migration with dissolution/precipitation. Earth and Planetary Science Letters 288 (1), 138–148.

Takei, Y., Holtzman, B. K., 2009a. Viscous constitutive relations of solid-liquid composites in terms of grain boundary contiguity : 1. grain boundary diffusion control model. Journal of Geophysical Research 114 (B6).

Takei, Y., Holtzman, B. K., 2009b. Viscous constitutive relations of solid-liquid composites in terms of grain boundary contiguity : 2. compositional model for small melt fractions. Journal of Geophysical Research : Solid Earth 114 (B6).

Takei, Y., Holtzman, B. K., 2009c. Viscous constitutive relations of solid-liquid composites in terms of grain boundary contiguity : 3. causes and consequences of viscous anisotropy. Journal of Geophysical Research : Solid Earth 114 (B6).

Tasaka, M., Hiraga, T., 2013. Influence of mineral fraction on the rheological properties of forsterite + enstatite during grain-size-sensitive creep : 1. grain size and grain growth laws. Journal of Geophysical Research 118 (8), 3970–3990.

Tasaka, M., Hiraga, T., Zimmerman, M. E., 2013. Influence of mineral fraction on the rheological properties of forsterite+ enstatite during grain-size-sensitive creep : 2. deformation experiments. Journal of Geophysical Research 118 (8), 3991–4012.

Thornber, C. R., Huebner, J. S., 1985. Dissolution of olivine in basaltic liquids : experimental observations and applications. American Mineralogist 70 (9-10), 934–945.

Truckenbrodt, J., Johannes, W., 1999. H_2O loss during piston-cylinder experiments. American Mineralogist 84, 1333–1335.

Underwood, E. E., 1970. Quantitative stereology. Addison-Wesley, Reading, MA.

Underwood, E. E., 1972. The stereology of projected images. Journal of microscopy 95 (1), 25–44.

Urai, J., Means, W., Lister, G., 1986. Dynamic recrystallization of minerals. Mineral and Rock Deformation : Laboratory Studies : The Paterson Volume, 161–199.

Wagner, C., 1961. Theorie der Alterung von Niederschlägen durch Umlösen (Ostwald-Reifung). Zeitschrift für Elektrochemie, Berichte der Bunsengesellschaft für physikalische Chemie 65 (7-8), 581–591.

Walte, N. P., Bons, P. D., Passchier, C. W., Koehn, D., 2003. Disequilibrium melt distribution during static recrystallization. Geology 31 (11), 1009–1012.

Warren, J. M., Hirth, G., 2006. Grain size sensitive deformation mechanisms in naturally deformed peridotites. Earth and Planetary Science Letters 248 (1), 438–450.

Yang, S.-C., Mani, S., German, R., 1990. The effect of contiguity on growth kinetics in liquid-phase sintering. JOM 42 (4), 16–19.

Yoshino, T., Takei, Y., Wark, D. A., Watson, E. B., 2005. Grain boundary wetness of texturally equilibrated rocks, with implications for seismic properties of the upper mantle. Journal of Geophysical Research : Solid Earth 110 (B8).

Yoshino, T., Yamazaki, D., Mibe, K., 2009. Well-wetted olivine grain boundaries in partially molten peridotite in the asthenosphere. Earth and Planetary Science Letters 283 (1), 167–173.

Zhang, Y., Walker, D., Lesher, C. E., 1989. Diffusive crystal dissolution. Contributions to Mineralogy and Petrology 102 (4), 492–513.

Annexe A

Grain size exponent determination from experimental results

The grain size exponent, n, can be fitted by a wide range of values, independently of the grain growth mechanism acting within the studied sample (German et al., 1997). Yet, to check this statement, I have plotted in this appendix the difference in grain sizes ($d_f^n - d_i^n$, with n ranging from 1 and 10) from my database as a function of time and indicated the coefficient of determination for each n-value. I have separated the data into three categories, i.e. (i) dry experiments (Section A.1), (ii) hydrated experiments (Section A.2) and (iii) melt-bearing experiments (Section A.3). This appendix therefore demonstrates that there is no coherent experimental n-value, whether the sample is dry, hydrated or contains variable melt fractions (Fig. C.2).

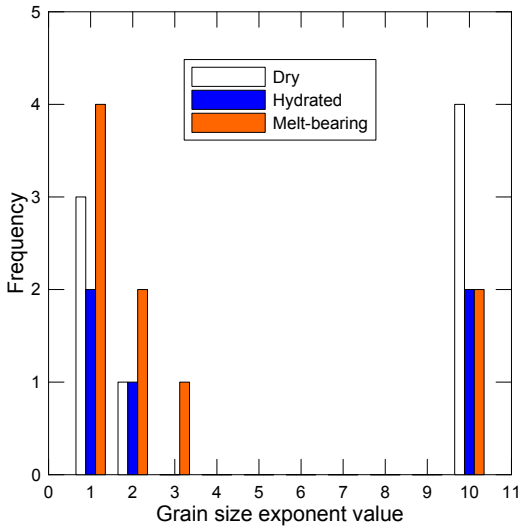

Figure A.1 – Histogram indicating the best fitted n-values from Fig. A.2 to Section A.3.

A.1 Dry atmospheric experiments

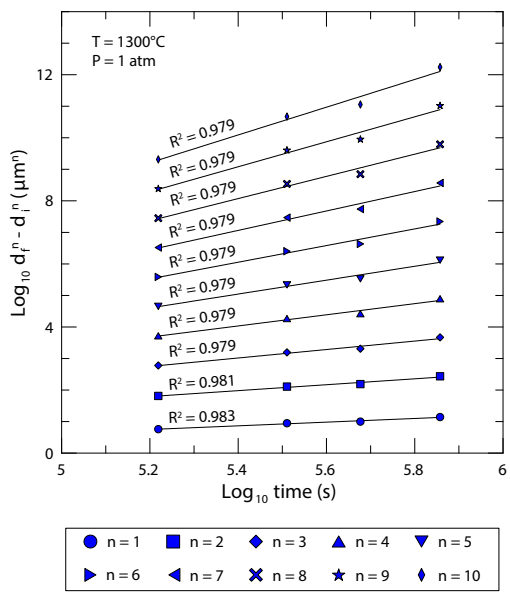

(a) Static grain growth experiments at atmospheric pressure under controlled f_{O_2} and 1300 °C. Data indicate that n = 1.

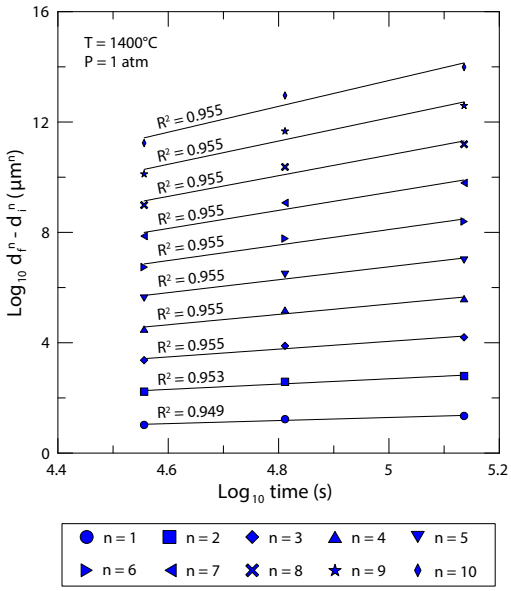

(b) Static grain growth experiments at atmospheric pressure under controlled f_{O_2} and 1400 °C. Data indicate that n = 10.

Figure A.2 – Dataset from (Karato, 1989) showing different grain size exponent values (n = 1 to 10) as a function of time. Although the same starting material was used at 1300 and 1400 °C, n = 1 at 1300 °C and n = 10 at 1400 °C.

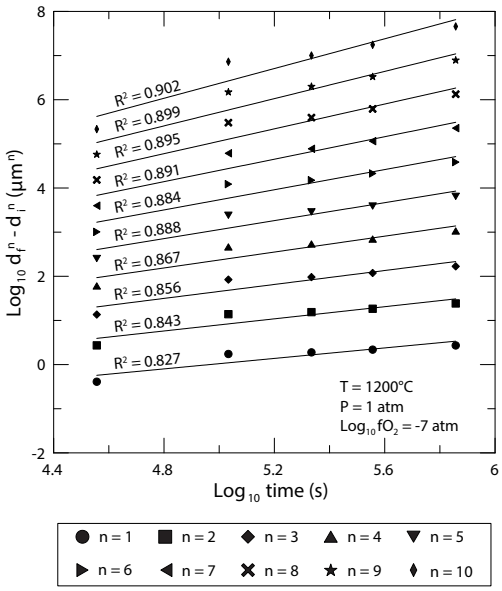

(a) Static grain growth experiments at atmospheric pressure under controlled f_{O_2} and 1200 °C. Data indicate that n = 10.

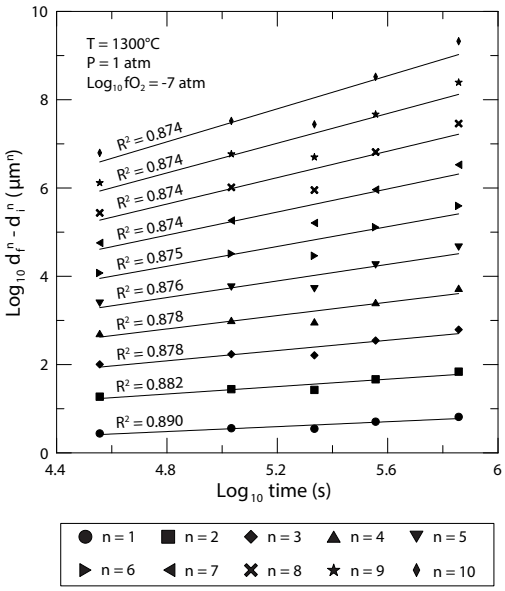

(b) Static grain growth experiments at atmospheric pressure under controlled f_{O_2} and 1300 °C. Data indicate that n = 1.

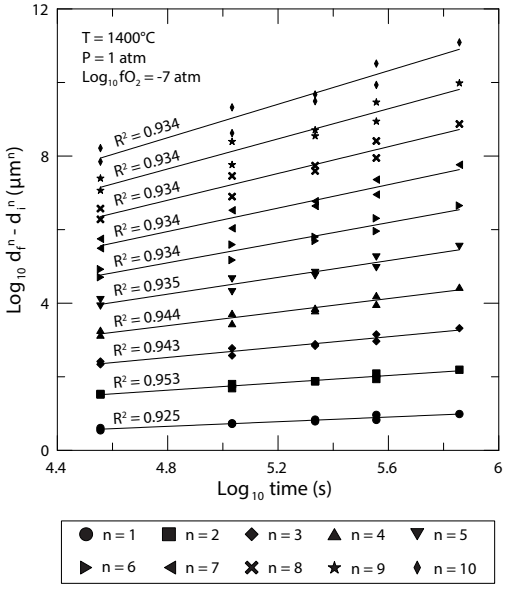

(c) Static grain growth experiments at atmospheric pressure under controlled f_{O_2} and 1400 °C. Data indicate that n = 2.

Figure A.3 – Dataset from (Nichols and Mackwell, 1991) showing different grain size exponent values (n = 1 to 10) as a function of time. Although the same starting material was used at 1200 to 1400 °C, n = 10 at 1200 °C, n = 10 at 1300 °C and n = 2 at 1400 °C.

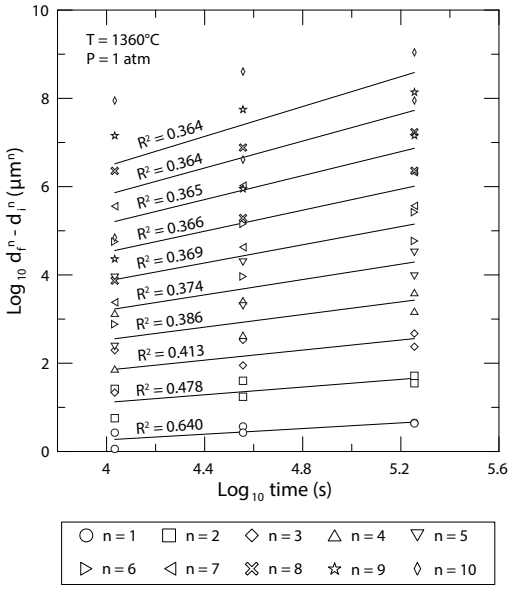

Figure A.4 – Dataset from (Hiraga et al., 2010) showing different grain size exponent values (n = 1 to 10) as a function of time. The static grain growth experiment was conducted at atmospheric pressure and 1360 °C, yielding n = 1.

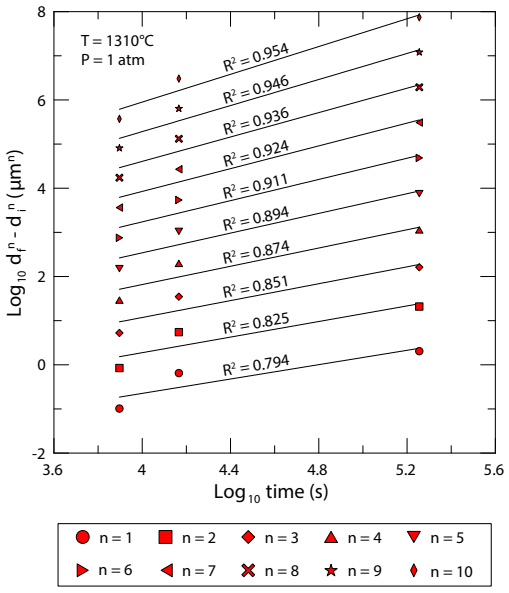

(a) Static grain growth experiments at atmospheric pressure and 1310 °C. Data indicate that n = 10.

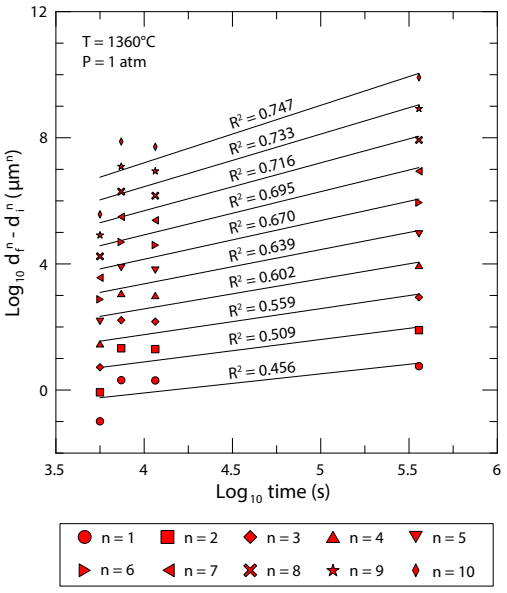

(b) Static grain growth experiments at atmospheric pressure and 1360 °C. Data indicate that n = 10.

Figure A.5 – Dataset from (Tasaka and Hiraga, 2013) showing different grain size exponent values (n = 1 to 10) as a function of time. The grain size exponent indicates a value of n = 10 at 1310 and 1360 °C.

A.2 Hydrated experiments

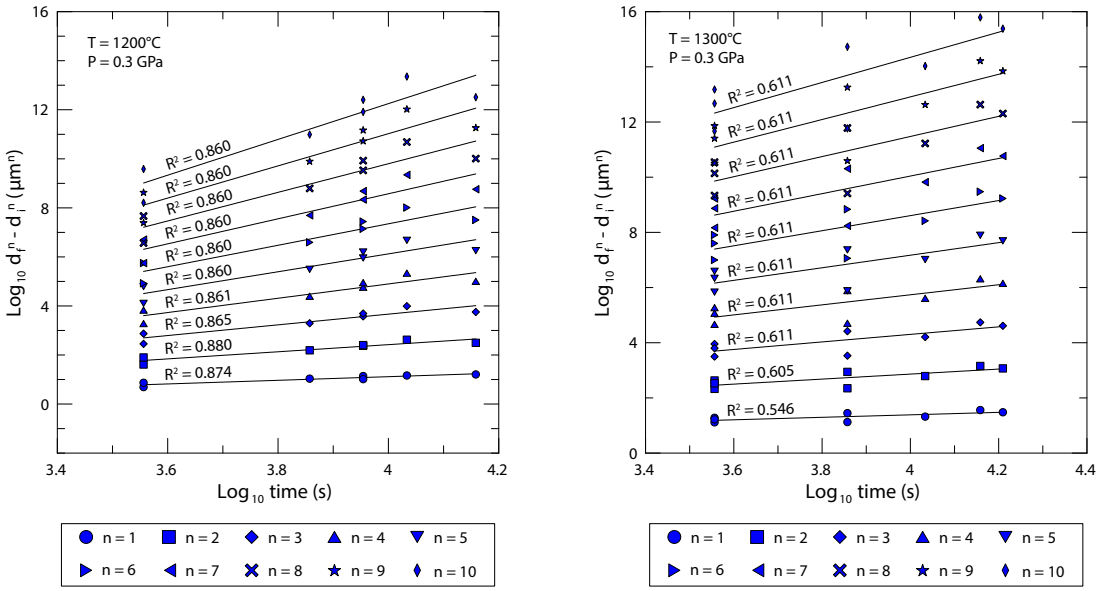

(a) Static grain growth experiments at 0.3 GPa and 1200 °C. Data indicate that n = 2.

(b) Static grain growth experiments at 0.3 GPa and 1400 °C. Data indicate that n = 10.

Figure A.6 – Dataset from (Karato, 1989) showing different grain size exponent values (n = 1 to 10) as a function of time. Although the same starting material was used at 1200 and 1300 °C, n = 2 at 1200 °C and n = 10 at 1300 °C.

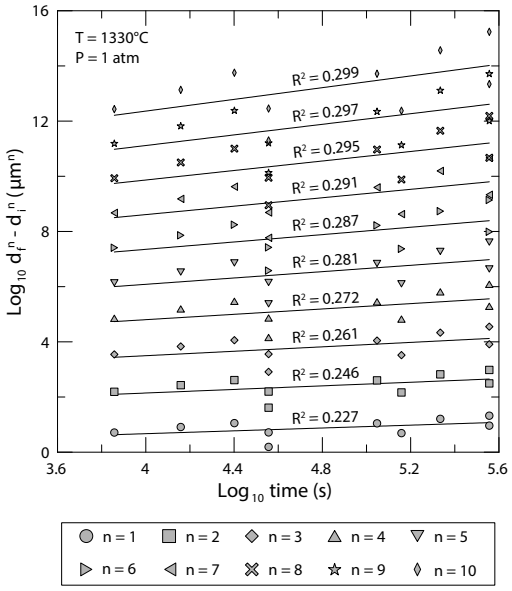

Figure A.7 – Dataset from (Nermond, 1994) showing different grain size exponent values (n = 1 to 10) as a function of time. The static grain growth experiment was conducted at atmospheric pressure (H_2-CO-Ar vessel) and 1330 °C, yielding n = 10.

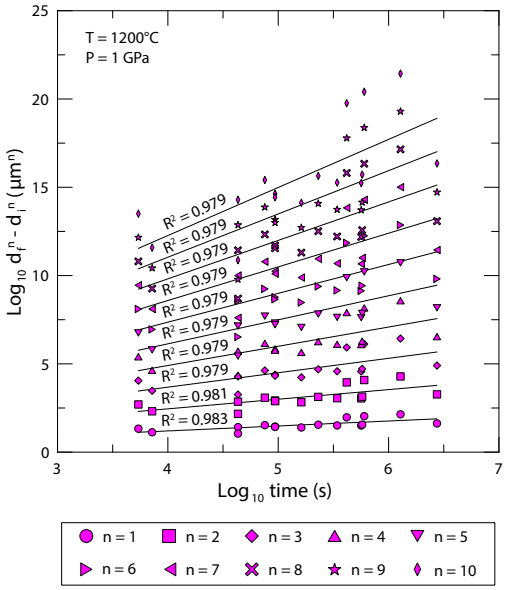

Figure A.8 – Dataset from (Ohuchi and Nakamura, 2007a,b) showing different grain size exponent values (n = 1 to 10) as a function of time. The static grain growth experiment was conducted at 1 GPa and 1200 °C, yielding n = 1.

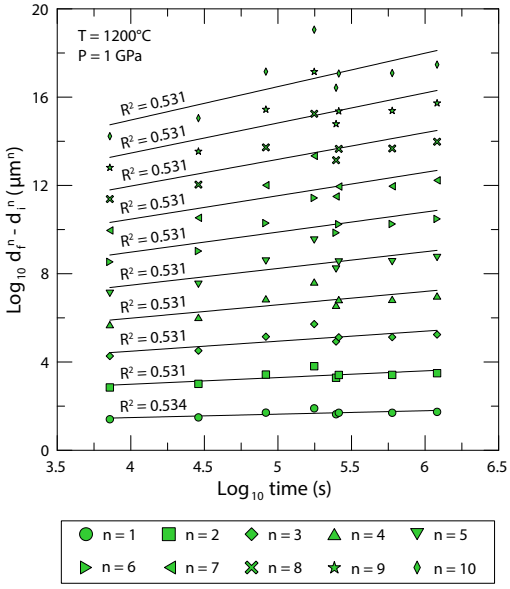

Figure A.9 – Dataset from (Ohuchi et al., 2010) showing different grain size exponent values (n = 1 to 10) as a function of time. The static grain growth experiment was conducted at 1 GPa and 1200 °C, yielding n = 1.

A.3 Melt-bearing experiments

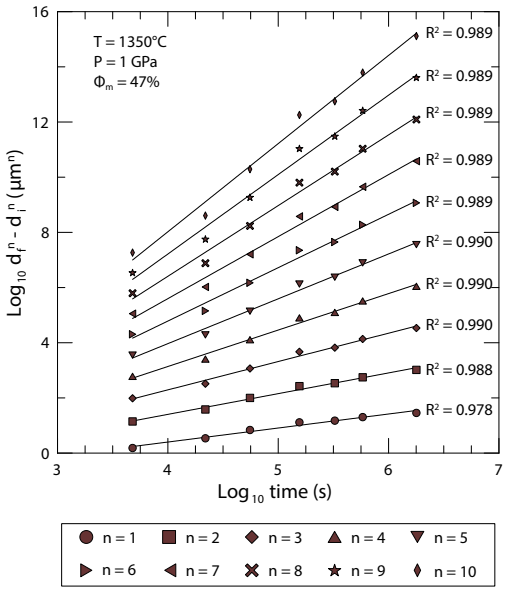

Figure A.10 – Dataset from (Cabane et al., 2005) showing different grain size exponent values (n = 1 to 10) as a function of time. The static grain growth experiment was conducted at atmospheric pressure and 1300 °C, yielding n = 3.

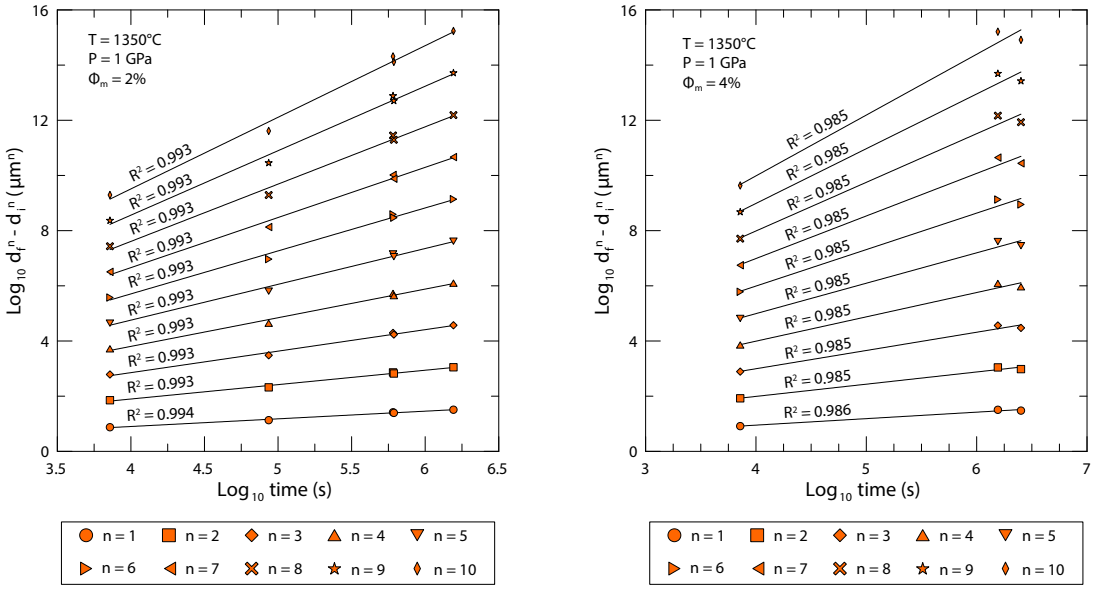

(a) Static grain growth experiments containing 2 wt melt at 1 GPa and 1350 °C. Data indicate that n = 1.

(b) Static grain growth experiments containing 4 wt. % melt at 0.5 GPa and 1250 °C. Data indicate that n = 1.

Figure A.11 – Dataset from (Faul and Scott, 2006) showing different grain size exponent values (n = 1 to 10) as a function of time. For the two melt contents investigated in this study, the grain size exponent, n, is of 1.

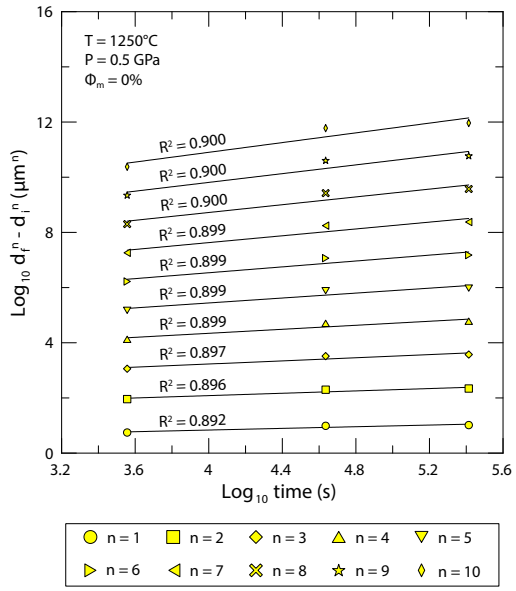

(a) Nominally melt-free static grain growth experiments at 0.5 GPa and 1250 °C. Data indicate that n = 10.

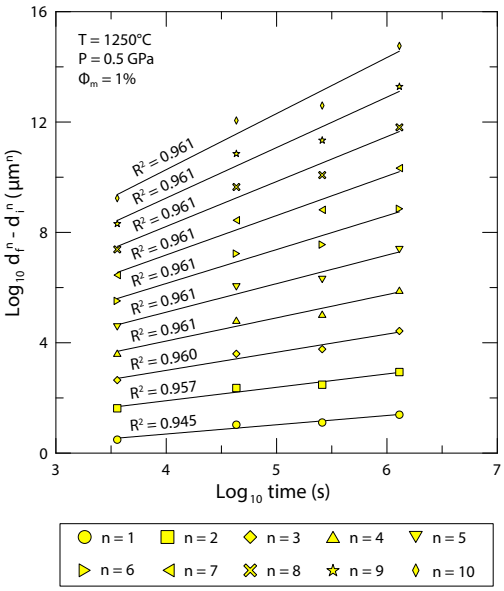

(b) Static grain growth experiments containing 1 wt. % melt at 0.5 GPa and 1250 °C. Data indicate that n = 10.

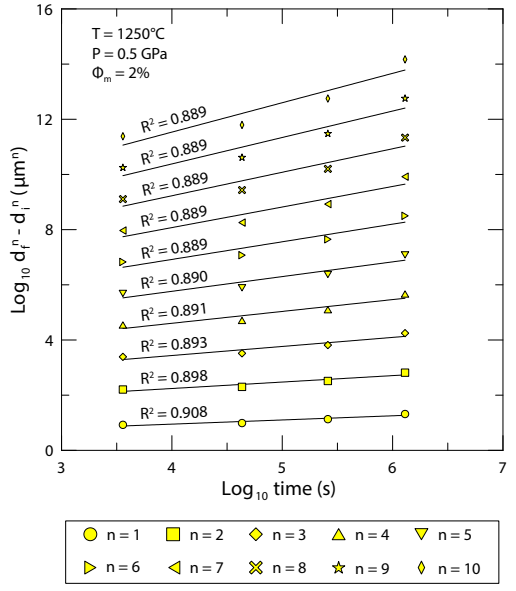

(c) Static grain growth experiments containing 2 wt. % melt at 0.5 GPa and 1250 °C. Data indicate that n = 1.

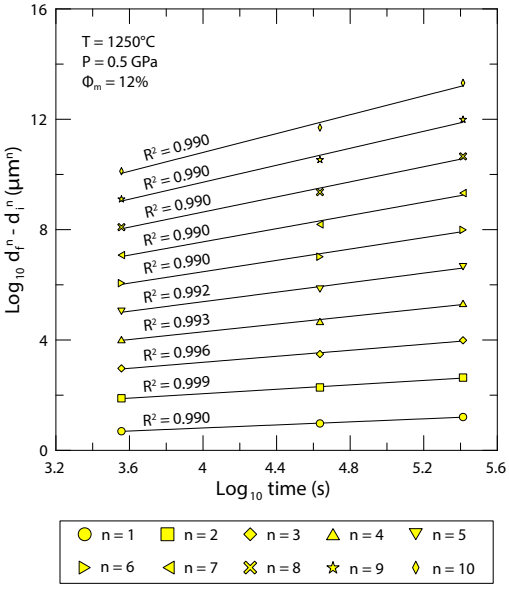

(d) Static grain growth experiments containing 12 wt. % melt at 0.5 GPa and 1250 °C. Data indicate that n = 2.

Figure A.12 – Dataset from my experimental study showing different grain size exponent values (n = 1 to 10) as a function of time. The grain size exponent, n, varies from 1 to 10 for the four melt contents investigated in this study (for both hematite or AlSiMag experiments).

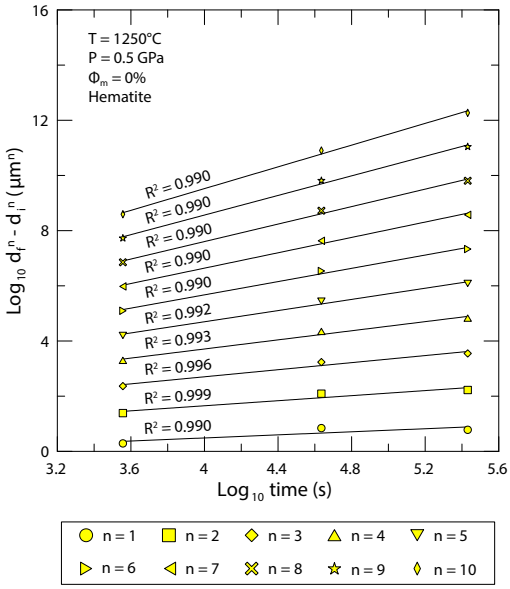

(e) Static grain growth experiments containing 0 wt. % melt at 0.5 GPa and 1250 °C (hematite experiment). Data indicate that n = 2.

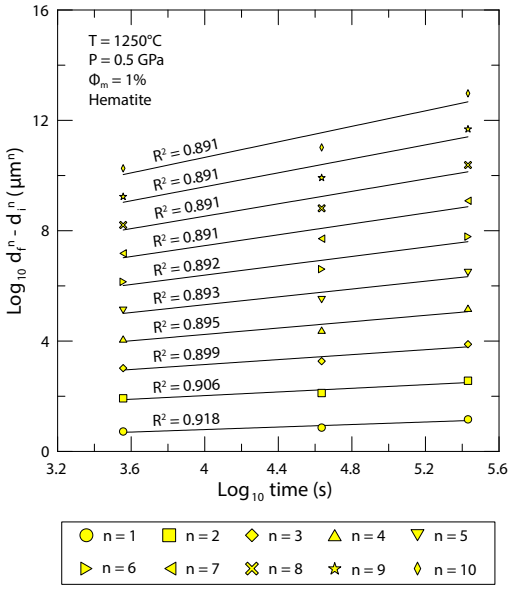

(f) Static grain growth experiments containing 1 wt. % melt at 0.5 GPa and 1250 °C (hematite experiment). Data indicate that n = 1.

(Continued).

Bibliography A

Cabane, H., Laporte, D., Provost, A., 2005. An experimental study of ostwald ripening of olivine and plagioclase in silicate melts: implications for the growth and size of crystals in magmas. Contributions to Mineralogy and Petrology 150 (1), 37–53.

Faul, U. H., Scott, D., 2006. Grain growth in partially molten olivine aggregates. Contributions to Mineralogy and Petrology 151 (1), 101–111.

German, R. M., Griffo, A., Liu, Y., 1997. Gravitational effects on grain coarsening during liquid-phase sintering. Metallurgical and Materials Transactions A 28 (1), 215–221.

Hiraga, T., Tachibana, C., Ohashi, N., Sano, S., 2010. Grain growth systematics for forsterite ± enstatite aggregates: Effect of lithology on grain size in the upper mantle. Earth and Planetary Science Letters 291 (1), 10–20.

Karato, S.-I., 1989. Grain growth kinetics in olivine aggregates. Tectonophysics 168 (4), 255–273.

Nermond, S., 1994. Étude expérimentale de la recristallisation statique et de la cinétique de croissance de l'olivine. Ph.D. thesis, Université de Montpellier.

Nichols, S. J., Mackwell, S. J., 1991. Grain growth in porous olivine aggregates. Physics and Chemistry of Minerals 18 (4), 269–278.

Ohuchi, T., Nakamura, M., 2007a. Grain growth in the forsterite–diopside system. Physics of the Earth and Planetary Interiors 160 (1), 1–21.

Ohuchi, T., Nakamura, M., 2007b. Grain growth in the system forsterite–diopside–water. Physics of the Earth and Planetary Interiors 161 (3), 281–304.

Ohuchi, T., Nakamura, M., Michibayashi, K., 2010. Effect of grain growth on cation exchange between dunite and fluid: implications for chemical homogenization in the upper mantle. Contributions to Mineralogy and Petrology 160 (3), 339–357.

Tasaka, M., Hiraga, T., 2013. Influence of mineral fraction on the rheological properties of forsterite + enstatite during grain-size-sensitive creep: 1. grain size and grain growth laws. Journal of Geophysical Research 118 (8), 3970–3990.

Appendix B

Determination of grain sizes

In order to determine the grain sizes, a wide number of analytical techniques have been applied, such as the line intercept method or grain area caluclations. In this section, I will briefly describe these methods before indicating the correctional factors and error estimates that I will be applying on the grain sizes determined in published experimental studies of olivine grain growth.

B.1 Methods

B.1.1 Mean linear intercept method

Grain size has traditionally been measured through optical and scanning (SEM) microscopes and by using the mean linear intercept method. Basically, lines of known lengths are randomly drawn on the optical or the SEM image and the grains intersecting the lines are counted. An apparent average grain size, $\bar{D}_{app}$, is therefore determined by dividing the line length, L, by the number of grains. However, as shown in Fig. B.1, the intercept lines do not systematically cross the grains at their maximum length (i.e. their center). To take into account this effect and retrieve the actual average grain size, $\bar{D}_{real}$, published studies have applied a correctional factor to the apparent average grain size, such that $\bar{D}_{real} = c \cdot \bar{D}_{app}$, with c >1.5.

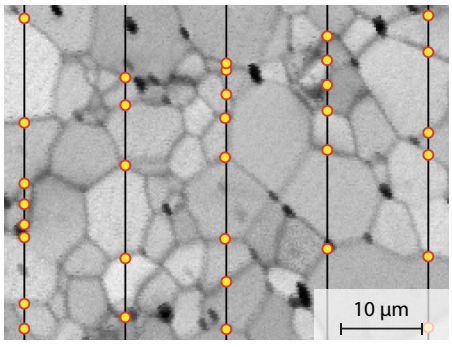

Figure B.1 – Example of grain size measurement by the linear intercept method (image quality map from EBSD measurements on sample 0PR-PC5 from my study). Black lines are randomly drawn on the studied section and grain boundaries are highlighted (yellow symbols) for grain counting. The average grain size is determined by dividing the line length by the number of intersected grains.

B.1.2 Area method

To date, the most used method is the area method where outlines of grains are traced from SEM images and areas retrieved from these outlines using image-processing softwares (e.g. ImageJ, Scion Image, Fig. B.2). This method assumes that the grains are essentially equiaxed. The grain sizes are then calculated from the conventional derivation of $2\sqrt{S/\pi}$ by assuming that each grain is a perfect sphere. The grain size values are averaged to obtain a representative apparent grain size, $\bar{d}$.

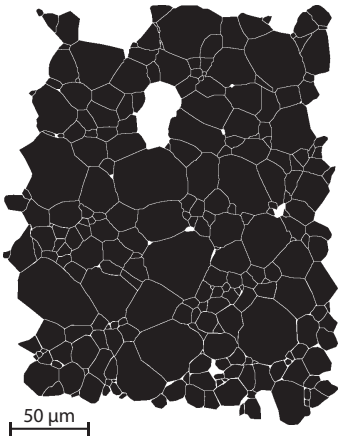

Figure B.2 – Example of grain size measurement by the area method (sample 0PR-PC5 from my study). Grains are outlined to obtain the area of each grain, which is then converted into grain sizes from the conventional derivation of $2\sqrt{S/\pi}$ by assuming each grain to be a perfect sphere.

B.2 Cut-section effect in the case of a spherical model in a monodispersed system

Grain sizes are usually determined from two-dimensional polished sections of samples that are either mounted in epoxy or from thin sections. The actual diameter of each particle is however not known because of cut-section effects but the probability to intercept these spheres is known. Royet (1991) showed that the actual diameter, d_{real}, is related to the apparent diameter, d_{app}, by a factor of $4/\pi$.

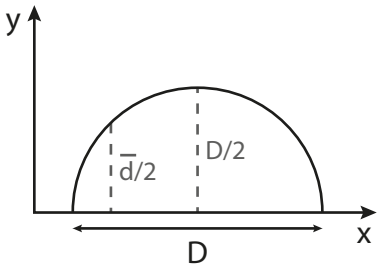

Figure B.3 – Illustration of the cut-section effect where $\bar{d}$ is the mean diameter of sphere profiles (equivalent to $\bar{d}_{app}$) when the system is monodispersed and D ($= d_{real}$) is the sphere diameter (after Royet (1991)).

In his demonstration (Fig. B.3), the mean height, $\bar{d}_{app}/2$ is obtained by dividing the integral function describing the semi-circle by the diameter. Since the surface of the semi-circle is equal to:

$$S = \pi d_{real}^2/8, \tag{B.1}$$

the mean height of the semi-chord parallel to the y-axis is:

$$\bar{d}_{app}/2 = \frac{\pi d_{real}^2/8}{d_{real}}, \tag{B.2}$$

which leads to:

$$d_{real} = \frac{4}{\pi} \cdot \bar{d}_{app}. \tag{B.3}$$

Therefore, whether it is the linear intercept method or the area method that is used, a correctional factor of $4/\pi$ should be applied to take into account the cut-section effect. In my manuscript, I discuss published experimental studies on olivine grain growth where the authors have not always taken this effect into account. As a result, all the grain sizes from published studies that are mentioned in this manuscript correspond to corrected grain size values following these successives steps:

- in case of grain size determination by the linear intercept method:
  1. the applied correction factor, c, was canceled,
  2. a correction factor of $4/\pi$ for the intercept bias was applied (Underwood, 1972, Greenman, 1951),
  3. a second correctional factor of $4/\pi$ for cut-section effects was applied;
- in case of grain size determination by the area method:
  1. a correctional factor of $4/\pi$ for cut-section effects was applied, when such a correction was not already employed.

B.3 Error estimation of determined grain sizes in previously published studies

The aforementioned methods for characterizing grain size have usually been used on SEM images or optical microphotographs. Therefore, if the grain boundaries are not clear on these images, defining a grain boundary becomes a subjective process, which is obviously dependent on the user's point of view. Determination of the average grain size in previously published experimental studies of olivine grain growth has without doubt been carried out in the most rigorous manner by the authors. Nonetheless, since grain boundary determination depends on the image quality and on the user, the uncertainties on grain sizes should be estimated accordingly. As a precaution, when using published data on olivine grain growth in this manuscript, an error estimate of 20% was therefore applied to the average grain size values whenever authors have used the linear intercept method, whereas an error estimate of 10% was assigned if the area method was employed.

Automated electron backscatter diffraction (EBSD) is nowadays increasingly used to measure and characterize grain structure. This technique relies on the crystallographic orientation of the grains in a polycrystalline sample and can therefore objectively map grain boundaries. However, the recent studies on olivine grain growth have seldom used this technique and continue to rely on SEM images of previously chemically or thermally etched samples (Faul and Scott, 2006, Hiraga et al., 2010, Ohuchi and Nakamura, 2007a,b, Ohuchi et al., 2010, Tasaka and Hiraga, 2013). To better define the uncertainties on grain sizes determined by the area method, Faul and Scott (2006) have compared the average grain sizes measured by EBSD mapping and by manually

outlining the grains from an SEM image of two samples. They concluded that the resulting average grain sizes determined by using the EBSD technique is within 4% of the manually obtained ones. Based on this comparison, when using published data on olivine grain growth in this manuscript, grain size uncertainties in the case of the area method have therefore been fixed to 14%.

B.4 Corrected measured grain sizes from previously published olivine grain growth experiments

Table B.1 indicates the experimental database used to define olivine grain growth under dry and melt-bearing conditions. The grain sizes and corresponding errors indicated in this table are already corrected as described above.

Table B.1 – Experimental database – Abbreviations — LH: this study; NM91: Nichols and Mackwell (1991); K89: Karato (1989); H10: Hiraga et al. (2010); FS06: Faul and Scott (2006); O10: Ohuchi et al. (2010); ON07: Ohuchi and Nakamura (2007a,b); CLP05: Cabane et al. (2005); TH13: Tasaka and Hiraga (2013); .

Reference	Exp. Name	T (°C)	P (GPa)	t (h)	Melt content (wt. %)	Opx content (wt. %)	log f_{O_2} (atm)	d_i (µm)	Error (µm)	d_f (µm)	Error (µm)
LH	IHPV2	1200.00	0.30	1.00	1.00	0.00	—	5.33	0.20	10.31	0.90
LH	IHPV2	1200.00	0.30	1.67	0.00	0.00	—	10.84	1.06	10.87	0.97
LH	IHPV1	1200.00	0.30	12.00	1.00	0.00	—	5.33	0.20	7.27	0.60
LH	IHPV1	1200.00	0.30	12.00	0.00	0.00	—	10.84	1.06	13.50	1.06
LH	PC12	1200.00	0.50	1.00	0.00	0.00	—	5.33	0.20	6.34	0.31
LH	PC12	1200.00	0.50	1.00	1.00	0.00	—	5.33	0.20	5.74	0.29
LH	PC8	1200.00	0.50	12.00	0.00	0.00	—	5.33	0.20	9.93	0.42
LH	PC8	1200.00	0.50	12.00	1.00	0.00	—	5.33	0.20	15.11	0.54
LH	PC8	1200.00	0.50	12.00	2.00	0.00	—	5.33	0.20	12.18	0.70
LH	PC8	1200.00	0.50	12.00	12.00	0.00	—	5.33	0.20	18.45	1.12
LH	PC2	1250.00	0.50	1.00	0.00	0.00	—	5.33	0.20	10.91	0.30
LH	PC2	1250.00	0.50	1.00	1.00	0.00	—	5.33	0.20	8.40	0.17
LH	PC2	1250.00	0.50	1.00	2.00	0.00	—	5.33	0.20	13.75	0.67
LH	PC2	1250.00	0.50	1.00	12.00	0.00	—	5.33	0.20	10.28	0.41
LH	PC4	1250.00	0.50	12.00	0.00	0.00	—	5.33	0.20	15.06	0.43
LH	PC4	1250.00	0.50	12.00	1.00	0.00	—	5.33	0.20	16.06	0.54
LH	PC4	1250.00	0.50	12.00	2.00	0.00	—	5.33	0.20	15.11	0.65
LH	PC4	1250.00	0.50	12.00	12.00	0.00	—	5.33	0.20	14.80	0.61
LH	PC23	1250.00	0.50	12.00	80.00	0.00	—	10.84	1.06	29.99	8.99
LH	PC5	1250.00	0.50	72.00	0.00	0.00	—	5.33	0.20	15.72	1.07
LH	PC5	1250.00	0.50	72.00	1.00	0.00	—	5.33	0.20	18.18	1.13
LH	PC5	1250.00	0.50	72.00	2.00	0.00	—	5.33	0.20	18.84	1.19
LH	PC5	1250.00	0.50	72.00	12.00	0.00	—	5.33	0.20	21.48	0.91
LH	PC6	1250.00	0.50	360.00	2.09	0.00	—	5.33	0.20	22.73	1.55
LH	PC6	1250.00	0.50	360.00	1.00	0.00	—	5.33	0.20	29.92	1.32
LH	PC6	1250.00	0.50	360.00	2.00	0.00	—	5.33	0.20	26.13	1.03
LH	PC6	1250.00	0.50	360.00	23.02	0.00	—	5.33	0.20	26.80	1.08
LH	PC15	1250.00	0.50	1.00	0.00	0.00	—	5.33	0.20	7.27	0.29
LH	PC15	1250.00	0.50	1.00	1.00	0.00	—	5.33	0.20	10.62	0.54
LH	PC14	1250.00	0.50	12.00	0.00	0.00	—	5.33	0.20	12.31	0.56
LH	PC14	1250.00	0.50	12.00	1.00	0.00	—	5.33	0.20	12.64	0.71
LH	PC20	1250.00	0.50	75.00	0.00	0.00	—	10.84	1.06	16.88	1.65

Experimental database (Continued).

Reference	Exp. Name	T (°C)	P (GPa)	t (h)	Melt content (wt. %)	Opx content (wt. %)	log f_{O_2} (atm)	d_i (µm)	Error (µm)	d_f (µm)	Error (µm)
LH	PC20	1250.00	0.50	75.00	1.00	0.00	—	5.33	0.20	19.85	2.04
LH	PC20	1250.00	0.50	75.00	84.14	0.00	—	10.84	1.06	34.43	8.94
LH	PC20	1250.00	0.50	75.00	0.00	0.00	—	10.84	1.06	23.17	1.71
LH	PC16	1250.00	1.50	1.00	0.00	0.00	—	5.33	0.20	7.38	0.44
LH	PC16	1250.00	1.50	1.00	1.00	0.00	—	5.33	0.20	11.55	0.87
LH	PC13	1250.00	1.50	12.00	0.00	0.00	—	5.33	0.20	32.21	2.40
LH	PC13	1250.00	1.50	12.00	1.00	0.00	—	5.33	0.20	30.94	2.03
LH	PC19	1250.00	1.50	12.00	0.00	0.00	—	10.84	1.06	13.84	0.92
LH	PC19	1250.00	1.50	12.00	1.00	0.00	—	5.33	0.20	22.01	2.09
LH	PC19	1250.00	1.50	12.00	0.00	0.00	—	10.84	1.06	17.33	1.89
LH	PC17	1350.00	1.50	1.00	0.00	0.00	—	5.33	0.20	18.72	1.52
LH	PC17	1350.00	1.50	1.00	1.00	0.00	—	5.33	0.20	19.02	2.04
LH	PC18	1350.00	1.50	12.00	0.00	0.00	—	5.33	0.20	22.07	2.36
LH	PC18	1350.00	1.50	12.00	1.00	0.00	—	5.33	0.20	40.39	2.65
LH	PC27	1350.00	3.00	12.00	1.00	0.00	—	5.33	0.20	84.68	6.72
LH	PC25	1350.00	1.00	2.00	0.00	0.00	—	1.00	0.10	2.69	0.14
NM91	HP2.4-	1200.00	$1.00 \cdot 10^{-4}$	10.00	0.00	0.00	−7.00	3.13	0.63	3.53	0.71
NM91	HP2.4-	1200.00	$1.00 \cdot 10^{-4}$	30.00	0.00	0.00	−7.00	3.13	0.63	4.86	0.97
NM91	HP2.4-	1200.00	$1.00 \cdot 10^{-4}$	60.00	0.00	0.00	−7.00	3.13	0.63	5.02	1.00
NM91	HP2.4-	1200.00	$1.00 \cdot 10^{-4}$	100.00	0.00	0.00	−7.00	3.13	0.63	5.31	1.06
NM91	HP2.4-	1200.00	$1.00 \cdot 10^{-4}$	200.00	0.00	0.00	−7.00	3.13	0.63	5.84	1.17
NM91	HP1.4-	1300.00	$1.00 \cdot 10^{-4}$	200.00	0.00	0.00	−7.00	2.03	0.41	8.56	1.71
NM91	HP1.4-	1300.00	$1.00 \cdot 10^{-4}$	10.00	0.00	0.00	−7.00	2.03	0.41	4.78	0.96
NM91	HP1.4-	1300.00	$1.00 \cdot 10^{-4}$	60.00	0.00	0.00	−7.00	2.03	0.41	5.55	1.11
NM91	HP1.4-	1300.00	$1.00 \cdot 10^{-4}$	30.00	0.00	0.00	−7.00	2.03	0.41	5.65	1.13
NM91	HP1.4-	1300.00	$1.00 \cdot 10^{-4}$	100.00	0.00	0.00	−7.00	2.03	0.41	7.11	1.42
NM91	HP1.3+	1400.00	$1.00 \cdot 10^{-4}$	10.00	0.00	0.00	−3.70	2.03	0.41	7.72	1.54
NM91	HP1.3+	1400.00	$1.00 \cdot 10^{-4}$	30.00	0.00	0.00	−3.70	2.03	0.41	9.41	1.88
NM91	HP1.3+	1400.00	$1.00 \cdot 10^{-4}$	60.00	0.00	0.00	−3.70	2.03	0.41	11.70	2.34
NM91	HP1.3+	1400.00	$1.00 \cdot 10^{-4}$	100.00	0.00	0.00	−3.70	2.03	0.41	16.12	3.22
NM91	HP1.3-	1400.00	$1.00 \cdot 10^{-4}$	60.00	0.00	0.00	−9.00	2.03	0.41	8.17	1.63
NM91	HP1.3-	1400.00	$1.00 \cdot 10^{-4}$	100.00	0.00	0.00	−9.00	2.03	0.41	9.86	1.97
NM91	HP1.3-	1400.00	$1.00 \cdot 10^{-4}$	10.00	0.00	0.00	−9.00	2.03	0.41	5.48	1.10
NM91	HP1.3-	1400.00	$1.00 \cdot 10^{-4}$	30.00	0.00	0.00	−9.00	2.03	0.41	7.10	1.42

Experimental database (Continued).

Reference	Exp. Name	T (°C)	P (GPa)	t (h)	Melt content (wt. %)	Opx content (wt. %)	log f_{O_2} (atm)	d_i (µm)	Error (µm)	d_f (µm)	Error (µm)
NM91	HP1.4+	1400.00	$1.00 \cdot 10^{-4}$	30.00	0.00	0.00	−5.00	2.03	0.41	8.17	1.63
NM91	HP1.4+	1400.00	$1.00 \cdot 10^{-4}$	60.00	0.00	0.00	−5.00	2.03	0.41	9.14	1.83
NM91	HP1.4+	1400.00	$1.00 \cdot 10^{-4}$	100.00	0.00	0.00	−5.00	2.03	0.41	13.21	2.64
NM91	HP1.4+	1400.00	$1.00 \cdot 10^{-4}$	10.00	0.00	0.00	−5.00	2.03	0.41	7.00	1.40
NM91	HP1.5+	1400.00	$1.00 \cdot 10^{-4}$	30.00	0.00	0.00	−7.00	2.03	0.41	7.28	1.46
NM91	HP1.5+	1400.00	$1.00 \cdot 10^{-4}$	60.00	0.00	0.00	−7.00	2.03	0.41	8.90	1.78
NM91	HP1.5+	1400.00	$1.00 \cdot 10^{-4}$	100.00	0.00	0.00	−7.00	2.03	0.41	11.26	2.25
NM91	HP1.5+	1400.00	$1.00 \cdot 10^{-4}$	10.00	0.00	0.00	−7.00	2.03	0.41	6.09	1.22
NM91	HP2.2+	1400.00	$1.00 \cdot 10^{-4}$	30.00	0.00	0.00	−11.00	3.13	0.63	6.98	1.40
NM91	HP2.2-	1400.00	$1.00 \cdot 10^{-4}$	10.00	0.00	0.00	−5.00	3.13	0.63	8.08	1.62
NM91	HP2.2-	1400.00	$1.00 \cdot 10^{-4}$	30.00	0.00	0.00	−5.00	3.13	0.63	8.33	1.67
NM91	HP2.2-	1400.00	$1.00 \cdot 10^{-4}$	60.00	0.00	0.00	−5.00	3.13	0.63	11.05	2.21
NM91	HP2.2-	1400.00	$1.00 \cdot 10^{-4}$	100.00	0.00	0.00	−5.00	3.13	0.63	12.56	2.51
NM91	HP2.5+	1400.00	$1.00 \cdot 10^{-4}$	30.00	0.00	0.00	−9.00	3.13	0.63	7.52	1.50
NM91	HP2.5+	1400.00	$1.00 \cdot 10^{-4}$	60.00	0.00	0.00	−9.00	3.13	0.63	8.40	1.68
NM91	HP2.5+	1400.00	$1.00 \cdot 10^{-4}$	100.00	0.00	0.00	−9.00	3.13	0.63	9.35	1.87
NM91	HP2.5+	1400.00	$1.00 \cdot 10^{-4}$	10.00	0.00	0.00	−9.00	3.13	0.63	6.42	1.28
NM91	HP2.5-	1400.00	$1.00 \cdot 10^{-4}$	30.00	0.00	0.00	−7.00	3.13	0.63	8.56	1.71
NM91	HP2.5-	1400.00	$1.00 \cdot 10^{-4}$	60.00	0.00	0.00	−7.00	3.13	0.63	9.28	1.86
NM91	HP2.5-	1400.00	$1.00 \cdot 10^{-4}$	100.00	0.00	0.00	−7.00	3.13	0.63	9.85	1.97
NM91	HP2.5-	1400.00	$1.00 \cdot 10^{-4}$	200.00	0.00	0.00	−7.00	3.13	0.63	12.85	2.57
NM91	HP2.5-	1400.00	$1.00 \cdot 10^{-4}$	10.00	0.00	0.00	−7.00	3.13	0.63	6.63	1.33
K89	4756	1300.00	0.30	8.00	1.00	0.00	—	1.87	0.37	18.67	3.73
K89	10kb	1300.00	1.00	20.00	1.00	0.00	—	1.70	0.34	26.48	5.30
K89	4914	1200.00	0.30	1.00	1.00	0.00	—	1.70	0.34	6.62	1.32
K89	4922	1200.00	0.30	1.00	1.00	0.00	—	1.70	0.34	9.08	1.82
K89	4924	1200.00	0.30	2.00	1.00	0.00	—	1.70	0.34	12.56	2.51
K89	4928	1200.00	0.30	4.00	1.00	0.00	—	1.70	0.34	17.83	3.57
K89	4918	1300.00	0.30	1.00	1.00	0.00	—	1.70	0.34	14.68	2.94
K89	4923	1300.00	0.30	1.00	1.00	0.00	—	1.70	0.34	20.80	4.16
K89	4925	1300.00	0.30	2.00	1.00	0.00	—	1.70	0.34	29.71	5.94
K89	4931	1300.00	0.30	4.00	1.00	0.00	—	1.70	0.34	37.94	7.59
K89	4674	1300.00	0.30	4.50	1.00	0.00	—	4.33	0.87	34.55	6.91

Experimental database (Continued).

Reference	Exp. Name	T (°C)	P (GPa)	t (h)	Melt content (wt. %)	Opx content (wt. %)	log f_{O_2} (atm)	d_i (µm)	Error (µm)	d_f (µm)	Error (µm)
K89	4743	1200.00	0.30	3.00	1.00	0.00	—	7.05	1.41	21.65	4.33
K89	4760	1300.00	0.30	1.00	1.00	0.00	—	1.87	0.37	18.50	3.70
K89	4883	1200.00	0.30	2.50	1.00	0.00	—	1.70	0.34	15.53	3.11
K89	4900	1300.00	0.30	2.00	1.00	0.00	—	1.70	0.34	15.02	3.00
K89	4883bis	1200.00	0.30	2.50	1.00	0.00	—	7.05	1.41	17.40	3.48
K89	4927	1300.00	0.30	3.00	1.00	0.00	—	4.33	0.87	25.30	5.06
K89	12-45	1200.00	$1.00 \cdot 10^{-4}$	45.00	0.00	0.00	−10.01	2.81	0.56	3.89	0.78
K89	12-187	1200.00	$1.00 \cdot 10^{-4}$	187.00	0.00	0.00	−10.01	2.81	0.56	5.73	1.15
K89	13-46	1300.00	$1.00 \cdot 10^{-4}$	46.00	0.00	0.00	−10.01	2.81	0.56	8.54	1.71
K89	13-90	1300.00	$1.00 \cdot 10^{-4}$	90.00	0.00	0.00	−10.01	2.81	0.56	11.67	2.33
K89	13-132	1300.00	$1.00 \cdot 10^{-4}$	132.00	0.00	0.00	−10.01	2.81	0.56	12.75	2.55
K89	13-200	1300.00	$1.00 \cdot 10^{-4}$	200.00	0.00	0.00	−10.01	2.81	0.56	16.75	3.35
K89	14-10	1400.00	$1.00 \cdot 10^{-4}$	10.00	0.00	0.00	−10.01	2.81	0.56	13.29	2.66
K89	14-18	1400.00	$1.00 \cdot 10^{-4}$	18.00	0.00	0.00	−10.01	2.81	0.56	19.78	3.96
K89	14-38	1400.00	$1.00 \cdot 10^{-4}$	38.00	0.00	0.00	−10.01	2.81	0.56	25.07	5.01
H10	—	1360.00	$1.00 \cdot 10^{-4}$	0.50	0.00	0.00	—	3.57	0.50	4.71	0.66
H10	—	1360.00	$1.00 \cdot 10^{-4}$	1.00	0.00	0.00	—	3.57	0.50	5.60	0.78
H10	—	1360.00	$1.00 \cdot 10^{-4}$	3.00	0.00	0.00	—	3.57	0.50	6.24	0.87
H10	—	1360.00	$1.00 \cdot 10^{-4}$	10.00	0.00	0.00	—	3.57	0.50	7.26	1.02
H10	—	1360.00	$1.00 \cdot 10^{-4}$	50.00	0.00	0.00	—	3.57	0.50	8.02	1.12
H10	—	1360.00	$1.00 \cdot 10^{-4}$	0.50	0.00	3.00	—	1.91	0.27	2.04	0.29
H10	—	1360.00	$1.00 \cdot 10^{-4}$	3.00	0.00	3.00	—	1.91	0.27	3.06	0.43
H10	—	1360.00	$1.00 \cdot 10^{-4}$	10.00	0.00	3.00	—	1.91	0.27	4.58	0.64
H10	—	1360.00	$1.00 \cdot 10^{-4}$	50.00	0.00	3.00	—	1.91	0.27	6.24	0.87
FS06	sgob9	1250.00	1.00	168.00	2.00	2.60	—	1.00	0.14	17.30	11.76
FS06	sgob12	1250.00	1.00	168.00	4.00	2.60	—	1.00	0.14	16.30	10.43
FS06	sgob4	1300.00	1.00	168.00	2.00	2.60	—	1.00	0.14	17.90	13.42
FS06	sgob1	1350.00	1.00	24.00	2.00	1.00	—	1.00	0.14	14.50	10.88
FS06	sgob10	1350.00	1.00	168.00	4.00	1.00	—	1.00	0.14	27.00	14.58
FS06	sgob11	1350.00	1.00	432.00	4.00	1.00	—	1.00	0.14	33.40	17.70
FS06	sgob13	1350.00	1.00	2.00	4.00	1.00	—	1.00	0.14	8.50	5.36
FS06	sgob2	1350.00	1.00	170.00	2.00	1.00	—	1.00	0.14	25.80	16.51
FS06	sgob3	1350.00	1.00	700.00	2.00	1.00	—	1.00	0.14	31.00	21.39
FS06	sgob7	1350.00	1.00	2.00	2.00	1.00	—	1.00	0.14	9.20	6.07

Experimental database (Continued).

Reference	Exp. Name	T (°C)	P (GPa)	t (h)	Melt content (wt. %)	Opx content (wt. %)	log f_{O_2} (atm)	d_i (µm)	Error (µm)	d_f (µm)	Error (µm)
FS06	sgob8	1350.00	1.00	432.00	2.00	1.00	—	1.00	0.14	33.20	19.26
FS06	sgob5	1400.00	1.00	168.00	2.00	0.50	—	1.00	0.14	28.20	18.89
FS06	sgob6	1450.00	1.00	168.00	2.00	0.00	—	1.00	0.14	38.40	24.19
O10	Per82-1	1200.00	1.20	69.00	0.00	0.00	—	1.00	0.14	43.93	6.15
O10	Per83-1	1200.00	1.20	72.00	0.00	0.00	—	1.00	0.14	50.93	7.13
O10	Per84-1	1200.00	1.20	8.00	0.00	0.00	—	1.00	0.14	31.96	4.47
O10	Per85-1	1200.00	1.20	335.00	0.00	0.00	—	1.00	0.14	55.90	7.83
O10	Per86-1	1200.00	1.20	2.00	0.00	0.00	—	1.00	0.14	26.48	3.71
O10	Per87-1	1200.00	1.20	166.00	0.00	0.00	—	1.00	0.14	51.18	7.17
O10	Per78-1	1200.00	1.20	23.00	0.00	0.00	—	1.00	0.14	51.95	7.27
O10	Per88-1	1200.00	1.20	49.00	0.00	0.00	—	1.00	0.14	80.47	11.27
O10	Per90-1	1200.00	1.20	4.00	0.00	0.00	—	1.00	0.14	32.98	4.62
ON07	per45-7	1200.00	1.20	2.00	0.00	0.00	—	1.00	0.14	22.15	3.10
ON07	per44-7	1200.00	1.20	12.00	0.00	0.00	—	1.00	0.14	33.49	4.69
ON07	per66-4	1200.00	1.20	21.00	0.00	0.00	—	1.00	0.14	29.92	4.19
ON07	per43-1	1200.00	1.20	69.00	0.00	0.00	—	1.00	0.14	48.13	6.74
ON07	per33-1	1200.00	1.20	116.00	0.00	0.00	—	1.00	0.14	54.75	7.66
ON07	per67-4	1200.00	1.20	167.00	0.00	0.00	—	1.00	0.14	47.62	6.67
ON07	per42-7	1200.00	1.20	431.00	0.00	0.00	—	1.00	0.14	61.62	8.63
ON07	per32-5	1200.00	1.20	1.50	0.00	0.00	—	1.00	0.14	22.41	3.14
ON07	per31-5	1200.00	1.20	12.00	0.00	0.00	—	1.00	0.14	26.87	3.76
ON07	per30-4	1200.00	1.20	26.00	0.00	0.00	—	1.00	0.14	29.03	4.06
ON07	per28-7	1200.00	1.20	26.00	0.00	0.00	—	1.00	0.14	27.76	3.89
ON07	per46-7	1200.00	1.20	64.00	0.00	0.00	—	1.00	0.14	36.67	5.13
ON07	per27-5	1200.00	1.20	95.00	0.00	0.00	—	1.00	0.14	33.61	4.71
ON07	per16-7	1200.00	1.20	157.00	0.00	0.00	—	1.00	0.14	33.36	4.67
ON07	per29-5	1200.00	1.20	160.00	0.00	0.00	—	1.00	0.14	37.31	5.22
ON07	per40-7	1200.00	1.20	763.00	0.00	0.00	—	1.00	0.14	43.16	6.04
ON07	per50-1	1200.00	1.20	2.00	0.00	0.00	—	1.00	0.14	14.39	2.01
ON07	per51-1	1200.00	1.20	12.00	0.00	0.00	—	1.00	0.14	12.22	1.71
ON07	per66-3	1200.00	1.20	21.00	0.00	0.00	—	1.00	0.14	34.76	4.87
ON07	per48-7	1200.00	1.20	45.00	0.00	0.00	—	1.00	0.14	25.85	3.62
ON07	per49-1	1200.00	1.20	116.00	0.00	0.00	—	1.00	0.14	94.60	13.24
ON07	per67-3	1200.00	1.20	167.00	0.00	0.00	—	1.00	0.14	110.01	15.40

Experimental database (Continued).

Reference	Exp. Name	T (°C)	P (GPa)	t (h)	Melt content (wt. %)	Opx content (wt. %)	log f_{O_2} (atm)	d_i (µm)	Error (µm)	d_f (µm)	Error (µm)
ON07	per52-1	1200.00	1.20	356.00	0.00	0.00	—	1.00	0.14	139.29	19.50
CLP05	Ol8	1300.00	$1.00 \cdot 10^{-4}$	1.33	47.00	0.00	—	3.82	0.53	5.35	0.75
CLP05	Ol11	1300.00	$1.00 \cdot 10^{-4}$	6.08	47.00	0.00	—	3.82	0.53	7.26	1.02
CLP05	Ol9	1300.00	$1.00 \cdot 10^{-4}$	15.40	47.00	0.00	—	3.82	0.53	10.70	1.50
CLP05	Ol5	1300.00	$1.00 \cdot 10^{-4}$	43.20	47.00	0.00	—	3.82	0.53	16.81	2.35
CLP05	Ol6	1300.00	$1.00 \cdot 10^{-4}$	90.43	47.00	0.00	—	3.82	0.53	18.84	2.64
CLP05	Ol7	1300.00	$1.00 \cdot 10^{-4}$	161.80	47.00	0.00	—	3.82	0.53	23.94	3.35
CLP05	Ol10	1300.00	$1.00 \cdot 10^{-4}$	496.38	47.00	0.00	—	3.82	0.53	32.47	4.55
TH13	KF-28	1360.00	$1.00 \cdot 10^{-4}$	2.40	0.00	0.00	—	4.66	0.65	9.56	1.34
TH13	KF-76	1260.00	$1.00 \cdot 10^{-4}$	5.55	0.00	3.00	—	3.91	0.55	4.42	0.62
TH13	—	1260.00	$1.00 \cdot 10^{-4}$	100.00	0.00	3.00	—	3.58	0.50	4.70	0.66
TH13	KF-42	1310.00	$1.00 \cdot 10^{-4}$	2.19	0.00	3.00	—	4.10	0.57	4.20	0.59
TH13	KF-75	1310.00	$1.00 \cdot 10^{-4}$	4.07	0.00	3.00	—	3.91	0.55	4.56	0.64
TH13	KF-68	1310.00	$1.00 \cdot 10^{-4}$	0.12	0.00	3.00	—	3.58	0.50	3.97	0.56
TH13	KF-67	1310.00	$1.00 \cdot 10^{-4}$	0.23	0.00	3.00	—	3.58	0.50	3.92	0.55
TH13	—	1310.00	$1.00 \cdot 10^{-4}$	50.00	0.00	3.00	—	4.10	0.57	6.14	0.86
TH13	KF-38	1360.00	$1.00 \cdot 10^{-4}$	1.56	0.00	3.00	—	4.10	0.57	4.20	0.59
TH13	KF-71	1360.00	$1.00 \cdot 10^{-4}$	3.21	0.00	3.00	—	3.91	0.55	5.92	0.83
TH13	KF-30	1360.00	$1.00 \cdot 10^{-4}$	2.06	0.00	3.00	—	4.10	0.57	6.15	0.86
TH13	KF-66	1360.00	$1.00 \cdot 10^{-4}$	0.12	0.00	3.00	—	3.58	0.50	3.99	0.56
TH13	KF-65	1360.00	$1.00 \cdot 10^{-4}$	0.22	0.00	3.00	—	3.58	0.50	4.77	0.67
TH13	—	1360.00	$1.00 \cdot 10^{-4}$	100.00	0.00	3.00	—	4.10	0.57	9.80	1.37

Bibliography B

Faul, U. H., Scott, D., 2006. Grain growth in partially molten olivine aggregates. Contributions to Mineralogy and Petrology 151 (1), 101–111.

Garapić, G., Faul, U., Brisson, E., 2013. High-resolution imaging of the melt distribution in partially molten upper mantle rocks: evidence for wetted two-grain boundaries. Geochemistry, Geophysics, Geosystems 14 (3), 556–566.

Greenman, N. N., 1951. On the bias of grain-size measurements made in thin-section: A discussion. The Journal of Geology, 268–274.

Hiraga, T., Tachibana, C., Ohashi, N., Sano, S., 2010. Grain growth systematics for forsterite ± enstatite aggregates: Effect of lithology on grain size in the upper mantle. Earth and Planetary Science Letters 291 (1), 10–20.

Ohuchi, T., Nakamura, M., 2007a. Grain growth in the forsterite–diopside system. Physics of the Earth and Planetary Interiors 160 (1), 1–21.

Ohuchi, T., Nakamura, M., 2007b. Grain growth in the system forsterite–diopside–water. Physics of the Earth and Planetary Interiors 161 (3), 281–304.

Ohuchi, T., Nakamura, M., Michibayashi, K., 2010. Effect of grain growth on cation exchange between dunite and fluid: implications for chemical homogenization in the upper mantle. Contributions to Mineralogy and Petrology 160 (3), 339–357.

Royet, J.-P., 1991. Stereology: a method for analyzing images. Progress in neurobiology 37 (5), 433–474.

Tasaka, M., Hiraga, T., 2013. Influence of mineral fraction on the rheological properties of forsterite + enstatite during grain-size-sensitive creep: 1. grain size and grain growth laws. Journal of Geophysical Research 118 (8), 3970–3990.

Underwood, E. E., 1972. The stereology of projected images. Journal of microscopy 95 (1), 25–44.

Zhu, W., Gaetani, G. A., Fusseis, F., Montési, L. G., De Carlo, F., 2011. Microtomography of partially molten rocks: three-dimensional melt distribution in mantle peridotite. Science 332 (6025), 88–91.

Appendix C

FTIR spectra and grain size distribution for melt-bearing olivine grain growth experiments

This appendix presents supplementary figures for the FTIR analyses performed in the study of melt-bearing olivine grain growths as well as the grain size distributions (Chapter 2).

C.1 FTIR spectra

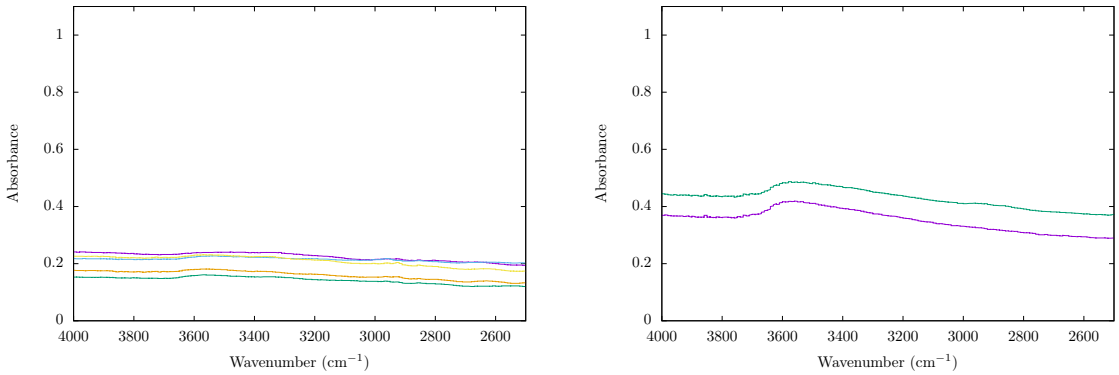

(a) 10PR-PC2 – Sample thickness is 29 µm.

(b) 10PR-PC4 – Sample thickness is 57 µm.

Figure C.1 – FTIR spectra.

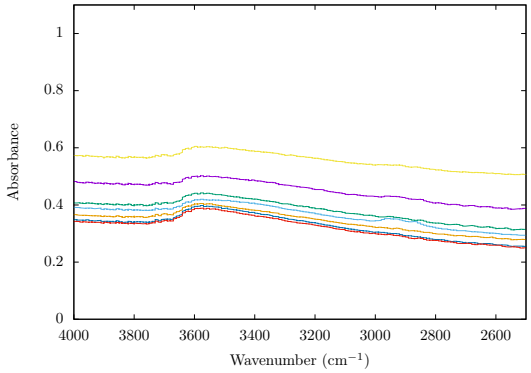

(a) 10PR-PC8 – Sample thickness is 62 µm.

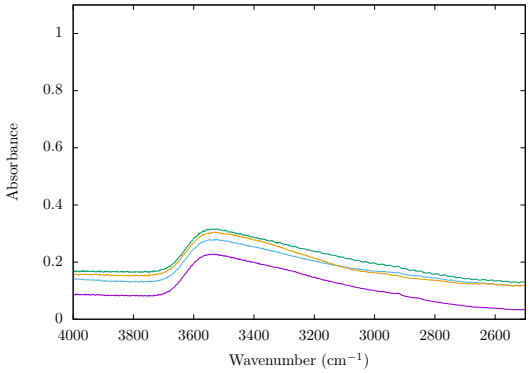

(b) 80PR-PC20 – Sample thickness ranges from 104 to 119 µm depending on the location of the spot.

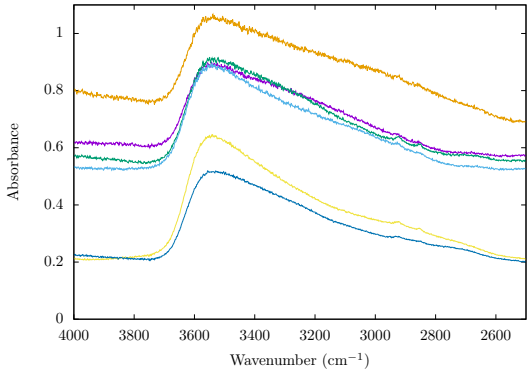

(c) 80PR-PC21 – Sample thickness is 99 µm.

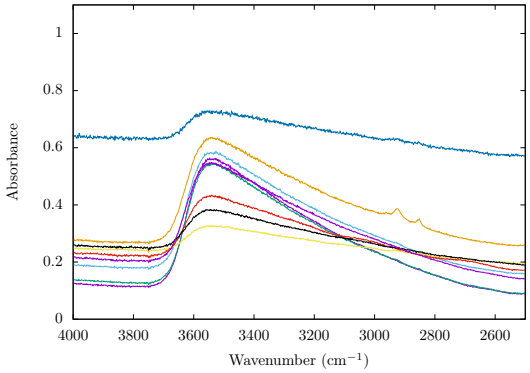

(d) 80PR-PC23 – Sample thickness ranges from 30 to 106 µm depending on the location of the spot.

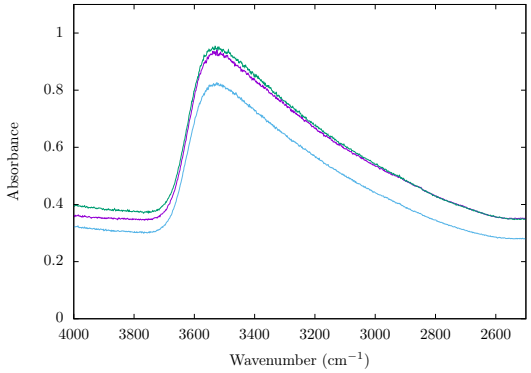

(e) 80PR-PC26 – Sample thickness ranges from 30 to 106 µm depending on the location of the spot.

FTIR spectra (continued).

C.2 Grain size distributions

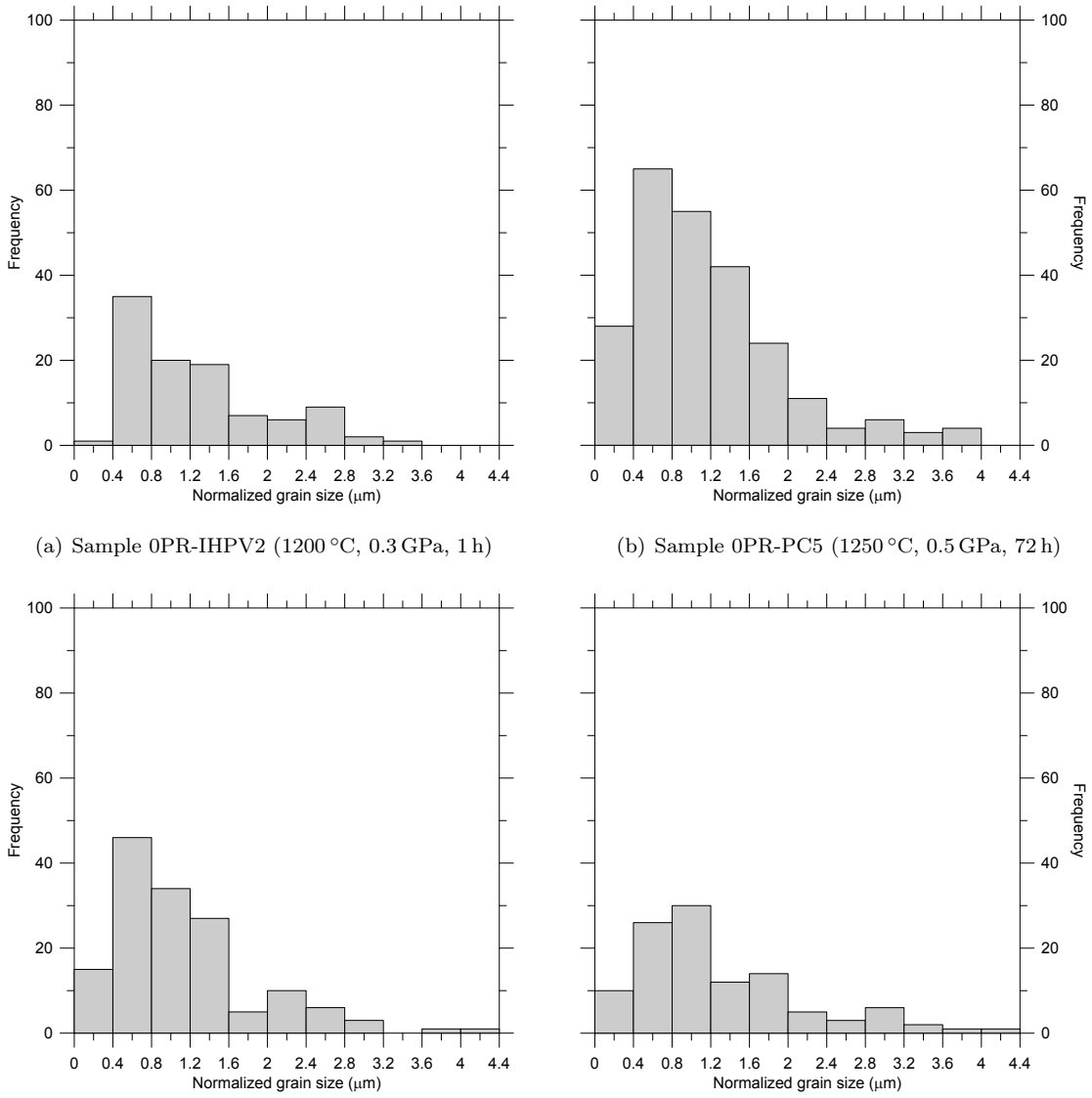

(a) Sample 0PR-IHPV2 (1200 °C, 0.3 GPa, 1 h)

(b) Sample 0PR-PC5 (1250 °C, 0.5 GPa, 72 h)

(c) Sample 0PR-PC18 (1350 °C, 1.5 GPa, 12 h)

(d) Sample 1PR-PC17 (1350 °C, 1.5 GPa, 1 h)

Figure C.2 – Typical grain size distributions. Normalized grain size correspond to the measured grain size divided by the median size.

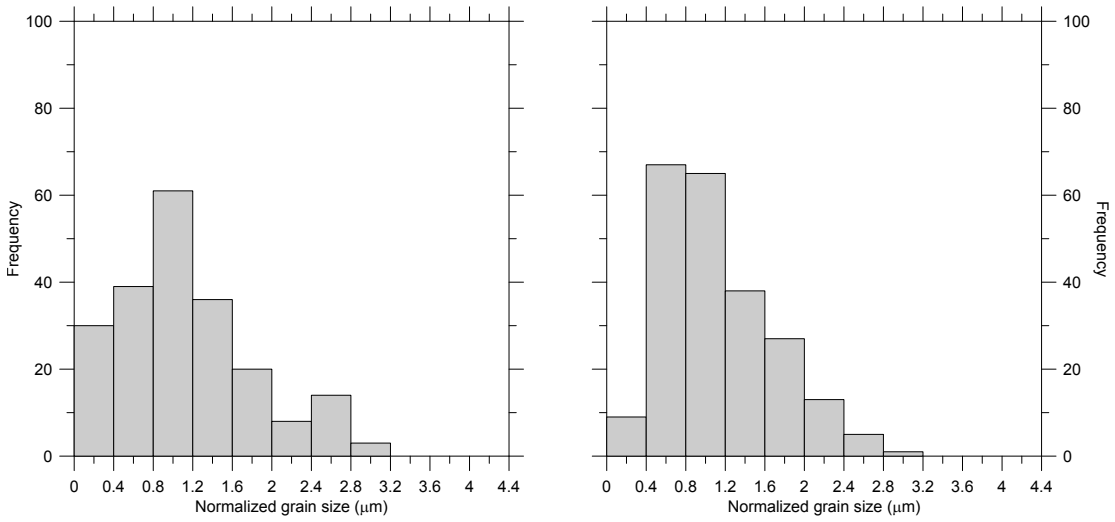

(a) Sample 2PR-PC5 (1250 °C, 0.5 GPa, 72 h)

(b) Sample 12PR-PC8 (1200 °C, 0.5 GPa, 12 h)

Typical grain size distributions. Normalized grain size correspond to the measured grain size divided by the median size (continued).

Leïla HASHIM

Observations expérimentales et modélisation de la croissance de grains d'olivine dans le manteau supérieur

Résumé :

La taille de grains dans le manteau terrestre a des implications cruciales sur les processus à grande échelle, telles que la propagation des ondes sismiques, la perméabilité et la rhéologie des roches. Cependant, la taille de grains évolue constamment avec le temps, car la croissance de grains statique induit une augmentation de la taille moyenne tandis que la recristallisation dynamique contribue à sa décroissance. La croissance d'olivine au sein d'agrégats mantelliques dans un milieu intergranulaire sec, en présence de liquide magmatique ou dans des conditions sursaturées en eau a été modélisée dans le cadre de cette thèse. En s'appuyant sur la théorie de croissance cristalline ainsi que sur des expériences à 1-atmosphère et hautes températures précédemment publiées, la loi de croissance d'olivine sèche a été déterminée. Le facteur limitant est, dans ce cas, la diffusion du silicium aux joints de grains à travers une épaisseur effective de 30 nm. La croissance d'agrégats en présence de liquide magmatique et fluide aqueux a été contrainte par de nouvelles expériences haute pression/haute température. Ces données indiquent que les taux de croissance sont significativement plus importants que dans des conditions sèches et sont limités par des réactions aux interfaces cristal/liquide. Nous proposons une loi de croissance générale régulée par une combinaison de joints de grains secs et mouillés, grâce aux paramètres de contiguité et de mouillabilité. Cette loi de croissance unifiée est fondamentale pour extrapoler les tailles de grains expérimentales à des échelles de temps, des profondeurs et des quantités de liquides relatives au manteau supérieur.

Mots clés : olivine, taille de grains, croissance, joint de grain, liquide magmatique, expériences HP-HT, diffusion, réaction à l'interface, mouillabilité, manteau.

Unraveling the grain size evolution in the Earth's mantle: Experimental observations and theoretical modeling

Abstract:

Grain size in the Earth's mantle is a fundamental parameter that has crucial implications on large-scale processes, such as seismic wave propagation, the permeability and the rheology of rocks. However, grain size is constantly evolving with time, where static grain growth implies an increase of the average grain size whereas dynamic recrystallization contributes to its decrease. Static grain growth of olivine-rich mantle aggregates in an intergranular medium being dry, melt-bearing and water-oversaturated has been here modeled. By using the appropriate theoretical background, the dry olivine grain growth law has been established from previously published experimental grain growth data at 1-atmosphere and high-temperature conditions. Grain growth rates for these samples are limited by silicon diffusion at grain boundaries through an effective width of 30 nm. Grain growth for melt- and water-bearing aggregates was, however, constrained by new high-pressure and high-temperature experiments. This data indicates that grain growth rates for liquid-bearing samples are significantly faster than for dry samples and are limited by precipitation reactions at the crystal/liquid interface rather by diffusion through the liquid phase. We propose a general grain growth law, which takes into account dry grain boundaries as well as wetted grain-grain interfaces, through the contiguity and wetness parameters. This unified law is fundamental to extrapolate experimental grain sizes to time scales, depths and liquid contents that are relevant of the upper mantle.

Keywords: olivine, grain size, grain growth, grain boundary, melt, HP-HT experiments, diffusion, interface reactions, wetness, mantle.

Institut des Sciences de la Terre d'Orléans
1A, rue de la Férollerie
45071 Orléans CEDEX 2